

2



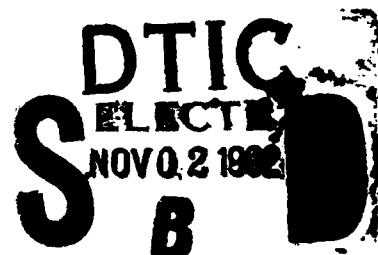
ACTIVE MICROPARTICLE MEDIA

T. P. Shen

**Rockwell International
1049 Camino Dos Rios
Thousand Oaks, CA 91360**

September 1992

Final Report



APPROVED FOR PUBLIC RELEASE; DISTRIBUTION UNLIMITED.

92-28556



**PHILLIPS LABORATORY
Lasers and Imaging Directorate
AIR FORCE MATERIEL COMMAND
KIRTLAND AIR FORCE BASE, NM 87117-6008**

92-28556

This final report was prepared by Rockwell International, Thousand Oaks, California, under Contract F29601-87-C-0050, Job Order 33261B14 with the Phillips Laboratory, Kirtland Air Force Base, New Mexico. The Laboratory Project Officer-in-Charge was Capt Victor C. Esch (LITN).

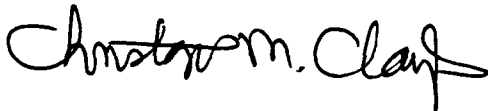
When Government drawings, specifications, or other data are used for any purpose other than in connection with a definitely Government-related procurement, the United States Government incurs no responsibility or any obligation whatsoever. The fact that the Government may have formulated or in any way supplied the said drawings, specifications, or other data, is not to be regarded by implication, or otherwise in any manner construed, as licensing the holder, or any other person or corporation; or as conveying any rights or permission to manufacture, use, or sell any patented invention that may in any way be related thereto.

This report has been authored by a contractor of the United States Government. Accordingly, the United States Government retains a nonexclusive royalty-free license to publish or reproduce the material contained herein, or allow others to do so, for the United States Government purposes.

This report has been reviewed by the Public Affairs Office and is releasable to the National Technical Information Service (NTIS). At NTIS, it will be available to the general public, including foreign nationals.

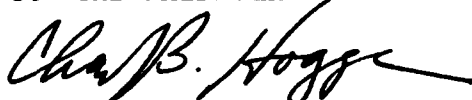
If your address has changed, if you wish to be removed from the mailing list, or if your organization no longer employs the addressee, please notify PL/LITN, Kirtland AFB, NM 87117-6008 to help maintain a current mailing list.

This report has been reviewed and is approved for publication.



CHRISTOPHER M. CLAYTON
Acting Chief, NLO Branch

FOR THE COMMANDER



CHARLES B. HOGGE, DV6
Acting Director, Lasers and Imaging
Directorate

DO NOT RETURN COPIES OF THIS REPORT UNLESS CONTRACTUAL OBLIGATIONS OR NOTICE ON A SPECIFIC DOCUMENT REQUIRES THAT IT BE RETURNED.

REPORT DOCUMENTATION PAGE

Form Approved
OMB No. 0704-0188

Public reporting burden for this collection of information is estimated to average 1 hour per response, including the time for reviewing instructions, searching existing data sources, gathering and maintaining the data needed, and completing and reviewing the collection of information. Send comments regarding this burden estimate or any other aspect of this collection of information, including suggestions for reducing this burden, to Washington Headquarters Services, Directorate for Information Operations and Reports, 1215 Jefferson Davis Highway, Suite 1204, Arlington, VA 22202-4302, and to the Office of Management and Budget, Paperwork Reduction Project (0704-0188), Washington, DC 20503.

| | | |
|----------------------------------|----------------------------------|--|
| 1. AGENCY USE ONLY (Leave blank) | 2. REPORT DATE September 1992 | 3. REPORT TYPE AND DATES COVERED Final 25 Sep 87 - 130 Jan 91 |
|----------------------------------|----------------------------------|--|

4. TITLE AND SUBTITLE

ACTIVE MICROPARTICLE MEDIA

5. FUNDING NUMBERS

C: F29601-87-C-0050
PE: 62601F
PR: 3326
TA: 1B
WU: 14

6. AUTHOR(S)

T. P. Shen

7. PERFORMING ORGANIZATION NAME(S) AND ADDRESS(ES)

Rockwell International
1049 Camino Dos Rios
Thousand Oaks, CA 91360

8. PERFORMING ORGANIZATION REPORT NUMBER

9. SPONSORING / MONITORING AGENCY NAME(S) AND ADDRESS(ES)

Phillips Laboratory
Kirtland AFB, NM 87117-6008

10. SPONSORING / MONITORING AGENCY REPORT NUMBER

PL-TR--91-1020

11. SUPPLEMENTARY NOTES

12a. DISTRIBUTION / AVAILABILITY STATEMENT

Approved for public release; distribution unlimited.

12b. DISTRIBUTION CODE

13. ABSTRACT (Maximum 200 words)

The theoretical and experimental research on the active nonlinear optical processes in the microparticle composites and conjugated polymers were investigated. The experimental studies focused on the transient effects in the phase conjugation and coherent beam combination using picosecond pulses. The theoretical studies emphasized the physical mechanisms of the nonlinear properties of the metallic microparticle composites and the conjugated polymers.

Solid-state nonlocal continuum for the nonlinear electrodynamics of the microparticle composites was developed. A semiclassical lattice-dynamic theory was derived to predict the large nonresonant optical nonlinearity below the bandgap for one-dimensional conjugated polymers. This effort concentrated on the electronic nonlinearity of the microparticle composites and the conjugated polymers. The electronic nonlinearity is the most significant contribution for the picosecond pulse applications, which are useful in the high bit-rate transmission and communication.

14. SUBJECT TERMS

Microparticles, Conjugate Polymers, Wave Mixing, Phase Conjugation

15. NUMBER OF PAGES

152

16. PRICE CODE

17. SECURITY CLASSIFICATION OF REPORT

Unclassified

18. SECURITY CLASSIFICATION OF THIS PAGE

Unclassified

19. SECURITY CLASSIFICATION OF ABSTRACT

Unclassified

20. LIMITATION OF ABSTRACT

SAR

TABLE OF CONTENTS

| | <u>Page</u> |
|---|-------------|
| 1.0 INTRODUCTION | 1 |
| 2.0 THEORY | 4 |
| 2.1 LINEAR RESPONSE | 8 |
| 2.2 SECOND-ORDER RESPONSE | 9 |
| 2.3 THIRD-ORDER RESPONSE | 11 |
| 3.0 ELECTRODYNAMICS OF MICROPARTICLE COMPOSITES | 14 |
| 3.1 LINEAR ELECTRODYNAMICS | 14 |
| 3.1.1 Scattering Amplitude in the Far Zone | 14 |
| 3.1.2 Macroscopic Electromagnetic Fields and Intensities | 16 |
| 3.1.3 Numerical Results and Discussion | 19 |
| 3.2 SUM AND DIFFERENCE FREQUENCY GENERATIONS | 20 |
| 3.2.1 Scattering Amplitude and the Radiation in the Far Zone | 20 |
| 3.2.2 Macroscopic Electromagnetic Fields and Intensities | 33 |
| 3.2.3 Numerical Results and Discussion | 37 |
| 3.3 THIRD-ORDER SUSCEPTIBILITY IN THE FREQUENCY DOMAIN | 43 |
| 3.3.1 Third-Order Susceptibility in the Frequency Domain | 45 |
| 3.3.2 Time-Dependence of Third-Order Susceptibility and Polarization | 53 |
| 3.4 SPECTRAL RANGE AND RESPONSE TIME | 56 |
| 3.5 SATURATION CHARACTERISTICS | 57 |
| 4.0 EXPERIMENTAL RESULTS | 59 |
| 4.1 PHASE CONJUGATION EXPERIMENTS | 59 |
| 4.1.1 Phase Conjugation in CS ₂ | 59 |
| 4.1.2 Phase-Conjugation in Gold Colloids | 68 |
| 4.2 COHERENT TWO-WAVE MIXING EXPERIMENTS | 76 |
| 4.2.1 Experimental Setup | 76 |
| 4.2.2 Experimental Results | 78 |

TABLE OF CONTENTS (Concluded)

| | <u>Page</u> |
|--|-------------|
| 5.0 COMPARISON | 88 |
| 5.1 LINEAR ABSORPTION SPECTRUM | 88 |
| 5.2 PHASE CONJUGATION | 89 |
| 5.3 COHERENT TWO-WAVE MIXING | 90 |
| 5.3.1 Transient Coherent Two-Wave Mixing in Kerr Medium | 90 |
| 5.3.2 Transient Coherent Two-Wave Mixing in Metallic Colloids (Gold and Silver) | 96 |
| 6.0 A ONE-DIMENSIONAL CONJUGATED POLYMER | 104 |
| 6.1 ONE-DIMENSIONAL VIBRON-LATTICE MODEL | 104 |
| 6.2 THIRD-ORDER NONLINEAR SUSCEPTIBILITY | 107 |
| 7.0 CONCLUSIONS | 111 |
| REFERENCES | 114 |
| APPENDIX A | 119 |
| APPENDIX B | 123 |
| APPENDIX C | 137 |

| | |
|---------------------------|-------------------------------------|
| Accession For | |
| NTIS GRA&I | <input checked="" type="checkbox"/> |
| DTIC TAB | <input type="checkbox"/> |
| Unannounced | <input type="checkbox"/> |
| Justification _____ | |
| By _____ | |
| Distribution/ _____ | |
| Availability Codes | |
| Dist. | Avail and/or Special |
| A-1 | |

DTIC QUALITY INSPECTED 1

LIST OF FIGURES

| <u>Figure</u> | <u>Page</u> |
|---|-------------|
| 1. The system to be considered | 5 |
| 2. Linear responses of a single silver sphere versus r/a , $a = 100 \text{ \AA}$ | 21 |
| 3. Surface plasma resonant frequency versus sphere radius | 22 |
| 4. The local field enhancement factor | 23 |
| 5. The particle size dependence of the real and imaginary parts of the dielectric function of the microspheres in water or glass with the damping parameter $\nu = 0.02 \omega_p$ or $0.1 \omega_p$ | 24 |
| 6. The host dielectric constant dependence of the real and imaginary parts of the dielectric function of the microspheres for radius 50 \AA or 100 \AA | 25 |
| 7. The frequency dependence of the real and imaginary parts as well as absolute value of dielectric function of micro- spheres in water | 26 |
| 8. The frequency dependence of the real and imaginary parts as well as absolute value of the dielectric function of microspheres in glass | 27 |
| 9. The frequency dependence of the refractive index and the extinction coefficient in water | 29 |
| 10. The frequency dependence of the refractive index and the extinction coefficient in glass | 30 |
| 11. Second-order dimensionless electron density profile $n_{2,lm}(r, \omega_{\pm})$ versus r/a , $a = 100 \text{ \AA}$ | 38 |
| 12. Second-order dimensionless radial electric field $\bar{\epsilon}_{r,lm}^{\pm}(r)$ versus r/a | 40 |
| 13. Second-order dimensionless radial velocity $\bar{\epsilon}_{r,lm}^{\pm}(r)$ versus r/a | 43 |
| 14. The incident θ_2 and coherent θ_{\pm} angles versus $\epsilon_h(\omega_{\pm})$ | 45 |
| 15. The reduced coherent and incoherent intensities versus $\epsilon_h(\omega_{\pm})$ | 46 |

LIST OF FIGURES (Continued)

| <u>Figure</u> | | <u>Page</u> |
|---------------|--|-------------|
| 16. | The dimensionless function U_{20}^{\pm} versus particle sizes | 47 |
| 17. | Experimental setup for the production of phase conjugation by degenerate four-wave mixing of picosecond pulses | 60 |
| 18. | Phase-conjugate reflectivity of CS ₂ in a 2-mm cell versus the pump energy in the forward pump beam, using a sample cell with retro-reflection mirror within the sample | 62 |
| 19. | Phase conjugate reflectivity of CS ₂ in a 2-mm sample cell versus the reduced pump energy E_r , for three different values of the ratio of backward to forward pump pulse energy E_b/E_f | 63 |
| 20. | Maximum value of the phase conjugate reflectivity, as obtained from different experiments, plotted versus the ratio of probe pulse fluence to forward pump beam fluence, F_{pr}/F_f | 66 |
| 21. | Phase conjugate reflectivity of CS ₂ in a 2-mm cell, at a pump to probe energy ratio of 500:1, plotted versus forward pump pulse energy | 67 |
| 22. | Laser system for high intensity, picosecond DFWM experiments | 69 |
| 23. | Phase conjugate reflectivity of Schott RG-6 gold colloid glass for high pump intensity, probe/pump ratio = 0.1, low repetition rate, 25 ps pulses for all beams incident (■); pump 1 blocked (O); pump 2 blocked (Δ) and all beams incident on an undoped glass sample (+) | 71 |
| 24. | Phase conjugation signal for water-based gold colloid and plain water in a 2-mm flow-through cell | 72 |
| 25. | Change in optical absorption at $\lambda = 543$ nm of Schott RG-6 as a function of total energy flux from pulsed Nd:YAG laser ($\lambda = 532$ nm) for average pulse energies of 0.1 mJ/pulse (+) and 1.0 mJ/pulse (□) | 73 |
| 26. | Continuous absorption of water-based gold colloid in a 2-mm cell before and after sample damage | 74 |
| 27. | A comparison of the interference of conjugate signals (●) and reference signals (□) from Schott RG-6 gold colloid glass and Schott OG-530 semiconductor colloid glass as a function of delay in the arm of the nonlinear interferometer | 75 |
| 28. | Experimental apparatus and beam geometry for degenerate two-wave mixing | 77 |

LIST OF FIGURES (Continued)

| <u>Figure</u> | | <u>Page</u> |
|---------------|--|-------------|
| 29. | Change in probe transmission in a semiconductor doped glass sample as a function of relative probe delay | 80 |
| 30. | Change in probe transmission in a liquid gold colloid sample as a function of relative probe delay | 81 |
| 31. | Change in probe transmission in a CS ₂ sample as a function of relative probe delay | 82 |
| 32. | Change in probe transmission in a nitrobenzene sample as a function of relative probe delay | 83 |
| 33. | Change in probe transmission in the polarization orthogonal to that of the initial probe polarization as a function of pump energy in the region of ~ 1 mJ per pulse | 83 |
| 34. | Change in probe transmission in a CS ₂ sample as a function of relative probe delay | 85 |
| 35. | Change in probe transmission intensity in a CS ₂ sample as a function of relative probe delay | 86 |
| 36. | Change in probe transmission in a CS ₂ sample as a function of relative probe delay | 87 |
| 37. | The linear absorption spectra of gold colloids within the quasi-hydrodynamic theory | 88 |
| 38. | Percentage of energy transfer versus pulse delay in CS ₂ for a pump/probe intensity ratio of 10, an optical path length of 5 mm and parallel polarization | 94 |
| 39. | Percentage of energy transfer versus pulse delay in CS ₂ for a pump/probe intensity ratio of 10, an optical path length of 5 mm and cross polarization | 95 |
| 40. | The time-dependence prefactors versus probe delay time for silver colloids in water ($\epsilon_h = 1.7689$) and glass ($\epsilon_h = 2.25$) with radius of 50 Å or 100 Å, pulse widths 10 ps and $t = x/v$ | 97 |
| 41. | The time-dependence prefactors versus probe delay time for silver colloids in water ($\epsilon_h = 1.7689$) and glass ($\epsilon_h = 2.25$) with radius of 50 Å or 100 Å, pulse widths 1 ps and $t = x/v$ | 99 |

LIST OF FIGURES (Concluded)

| <u>Figure</u> | | <u>Page</u> |
|---------------|---|-------------|
| 42. | The time-dependence prefactors versus probe delay time for silver colloids in water ($\epsilon_h = 1.7689$) and glass ($\epsilon_h = 2.25$) with radius of 50 Å or 100 Å, pulse widths 0.4 ps and $t = x/v$ | 101 |

LIST OF TABLES

| <u>Table</u> | | <u>Page</u> |
|--------------|---|-------------|
| 1. | Adjustable parameters of degenerate two-wave mixing | 87 |

I.0 INTRODUCTION

There has been considerable interest in the nonlinear electrodynamical characteristics of microparticle composites (Refs. 1,2). Of particular interest are situations in which one or more of the microparticle's Frohlich modes have been resonantly excited by incident laser light. For such situations excitation of this surface mode amplifies the incident laser intensity which gives rise to enhanced nonlinear optical coefficients (Ref. 3).

Theory for surface-enhanced phase conjugation and coherent beam combination (or coherent two-wave mixing) is relatively primitive, and this final report focuses on calculating the third-order susceptibility, its magnitude, spectral range, response time, and possible saturation characteristics.

The amplitude of the laser electric field in the vicinity of a metallic microparticle is dramatically amplified at the surface plasma frequency. This feature of microparticle electrodynamics arises from a resonant coupling of the laser radiation with the electron plasma mode and has been used as a means to greatly enhance a variety of nonlinear processes.

In the theoretical studies, the electrodynamic problem of metallic microparticle composites has been treated globally, calculating the multipole moment induced upon the microparticles by the applied field. The surface-plasma resonance as well as the local field enhancement of the microparticles within the quasi-hydrodynamic formalism was obtained directly. In the theory the local field enhancement factors come in naturally. However, in other quantum mechanical calculations the enhancement factors have to be added at the end for the local field.

The linear response, which includes the linear fields, linear susceptibility, refractive index, and extinction coefficient with enhancement at the surface plasma dipole mode frequency will be calculated. The linear response always co-exists with the third-order response at fundamental frequencies. In particular, the linear absorption is an important limiting factor in the third-order nonlinear processes. The second-order response, which includes the second-order fields and intensity for the sum and difference frequency generation with enhancement at the surface plasma dipole and quadrupole mode frequencies will also be calculated. The sum and difference frequency generations

are intermediate processes to nondegenerate phase conjugation and coherent two-wave mixing in microparticle composites. The dc rectified and second harmonic generations are intermediate processes to degenerate and nondegenerate phase conjugation and coherent two-wave mixing in microparticle composites.

Then, the third-order response, which includes the third-order fields and susceptibility with enhancement at the surface plasma dipole frequency, will be calculated. The contribution of third-order susceptibility arises in microparticle composites through the product of linear fields and second-order fields as well as in the triple product of the linear fields. The contribution from the triple product of the linear fields, which is the commonly known direct effect, is not the major source of the third-order nonlinearity. The contribution from the second-order fields, referred to as cascading effect, is the dominant one. The time-dependent third-order susceptibility will be calculated to explain the transient behaviors in the wave-mixing for the microparticle composites.

To be more specific, the nonlinear electrodynamics of a microparticle composite are examined using a solid-state nonlocal continuum theory (Refs. 3,4,5). The problem is formulated in terms of the perturbative response of a particle, which consists of a degenerate electron gas moving in a positive uniform jellium (a uniform positively charged medium against which the electrons move) background, to laser beams within the quasi-hydrodynamic approximation (Refs. 4,5). The first-order, second-order and third-order dynamic responses of the particle to laser light are extracted. Specifically, the perturbed electron density and drift velocity are determined as well as the laser-induced dipole and quadrupole moments. The electrodynamic properties of the local fields in the vicinity of the microparticles are also resolved. The macroscopic electrodynamic response of the medium as a whole and results for the intensity, polarization, and angular dependence are presented.

In experimental studies, the phase conjugation and coherent two-wave mixing both in CS₂ and gold colloids were performed using picosecond pulses. The experiments done in CS₂, which is a well-studied simple Kerr liquid, were used to calibrate the more complex gold colloid system. From the degenerate phase conjugation experiments done in CS₂ and gold colloids, the degenerate third-order susceptibility for gold colloids was obtained. The transient time-resolved degenerate two-wave mixing experiments were

performed to investigate the coherent coupling coefficients in the time domain for nonlinear media. The polarization resolved experiments were also performed to study the anisotropy of the third-order susceptibility.

The experimental values of the third-order susceptibility for the gold colloids are larger than the calculated values from the free carrier contribution within the quasi-hydrodynamic formalism. It indicates that the gold colloids have other nonlinear mechanisms involved. However, for the silver colloids the third-order susceptibility between the experimental and theoretical values, which are 10^{-9} esu per sphere, are comparable. This can be explained by the fact that the plasma frequency of silver falls just below the threshold for d-electron transitions and so free electron behavior is approximately satisfied for silver. For gold, the threshold of core electron transition lies at a frequency below the plasma frequency. The overlapping of valence electron and d-electron transitions prevents the existence of a frequency range in which the free electron behavior is dominant. Therefore, the third-order susceptibility of gold colloids will result from the d-electron contribution as well.

The experiment and the theory for transient time-resolved and polarization-resolved coherent two-wave mixing in CS_2 are in excellent agreement. Qualitative explanation for the transient time-resolved and polarization-resolved coherent two-wave mixing in gold colloids will be given.

In search of alternative nonlinear optical materials, there was a theoretical investigation of the one-dimensional conjugated polymers. A one-dimensional lattice model Hamiltonian was used to calculate their third-order polarization and susceptibility. The nonresonant nonlinearity of the conjugated polymers below their band gap is on the order of 10^{-10} esu.

The final part of the report gives conclusions and recommendations for microparticle composites as well as conjugated polymers as a phase-conjugation or image amplification mediums.

2.0 THEORY

Consider a metallic microparticle composite whose particle size is $< 100 \text{ \AA}$. This is small compared to any of the radiation wavelengths so that the Rayleigh limit is valid. Also, the quasi-static approximation is used where the Maxwell equations are reduced to the electrostatic equation. If the incident and nonlinear-generated frequencies are all sufficiently high, the ionic (or phonon) contribution inside the microparticles will be negligible. It is assumed that each of the microparticles in the composite consists of a rigid, positive jellium background with charge density en_0 accompanied by a degenerate electron gas. The dynamics of the electron gas is described by the quasi-hydrodynamic theory with damping. Charge neutrality demands that the unperturbed electron density be n_0 and in the presence of laser radiation the perturbed electron density is denoted by $n(r,t)$. Note that Fuchs and Kliewer have shown that the hydrodynamic and self-consistent field approximations yield the same results at all experimentally accessible frequencies (Ref. 6). Thus, Landau damping can be accounted for with a simple dissipation model characterized by a frequency-independent damping constant, ν . It is also assumed that microparticle size exceeds 20 \AA so that the quantum-size effect is not important (Ref. 7).

The hydrodynamic equations, which are the Euler equation and the equation of continuity, govern the response of the electron gas to incident laser radiation. Here, the nonlinear response of a single-sphere, which consists of a degenerate electron gas, confined to a microsphere of radius a , embedded in a passive linear dielectric and irradiated by laser beams is examined. The unperturbed electron profile is taken to be a step function. Although a step function does poorly for a flat metal surface (Ref. 8), it is used here for several reasons. (1) It is the standard model used for modeling the nonlinear optics due to the resonant plasmon responses of metallic microspheres (Ref. 9*) and using more complex spatial profiles is computationally prohibitive. (2) The nonlinear plasmon response appears to involve the electron fluid deep within the microsphere, not just at the surface. Thus, on physical grounds, the frequency-mixing properties of these resonances should not be overly sensitive to the details of the

*In their calculation, a circularly polarized light is used and no second-order monopole response.

electron profile near the surface. Mathematically, this is reflected in the fact that the dipole and quadrupole moments require an integration of various moments of the density over the entire volume of the microsphere. (3) Although other profiles will give different results, these differences are masked by the fact that numerous suspension parameters (geometric shape, particle size distribution and metallic purity) will vary significantly from the model and from sample-to-sample.

The physical situation is depicted in Figure 1. The ω_1 beam is incident normal to the surface of microparticle composite, is elliptically polarized, has a polarization vector $\hat{e}_1 = \hat{y} + \eta\hat{z}$ and a propagation vector $\mathbf{k}_1 = k_1\hat{x}$ within the medium. For a circularly polarized light, $\eta = i$. The second laser beam is oriented at an angle θ_0 with respect to the first beam, has a unit polarization vector $\hat{e}_2 = (\hat{x}\cos\theta_2 + \hat{z}\sin\theta_2)$ and a propagation vector $\mathbf{k}_2 = k_2(\hat{x}\sin\theta_2 - \hat{z}\cos\theta_2)$ within the medium, where $\theta_2 = \pi/2 - \theta_0$. Here, $k_j = [\epsilon_h(\omega_j)]^{1/2}\omega_j/c$, with $\epsilon_h(\omega_j)$ the dielectric constant of the host at the frequency ω_j .

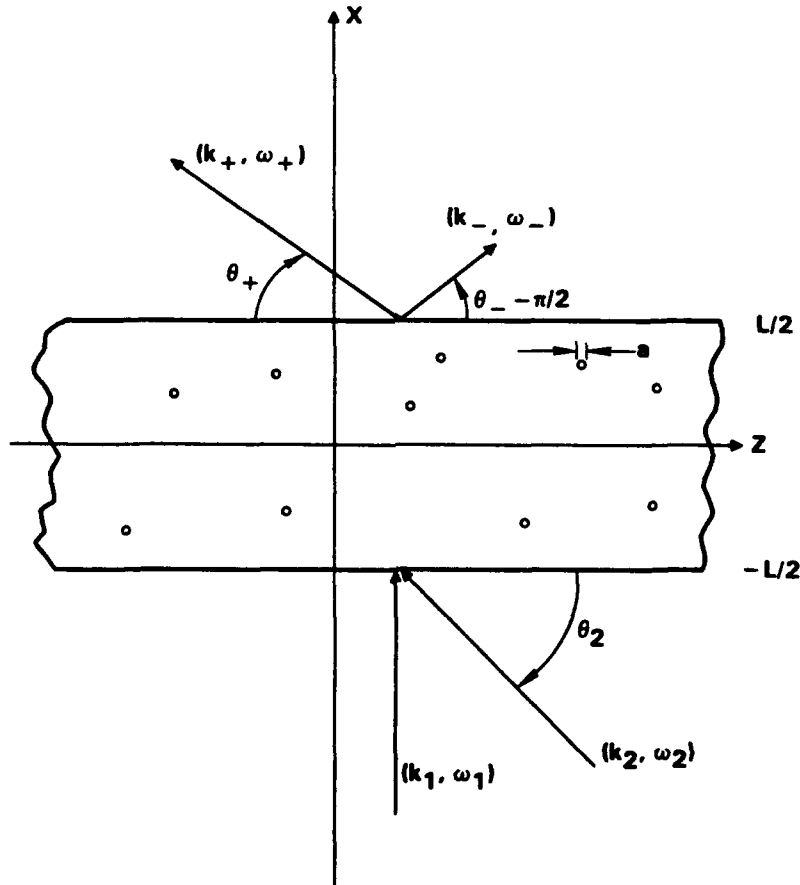


Figure 1. The system to be considered.

Within each microparticle, laser radiation induces an electron drift velocity, $\mathbf{v}(\mathbf{r},t)$ whose dynamics are governed by the Euler equation

$$n(\mathbf{r},t) \{ \partial/\partial t + \nu + \mathbf{v}(\mathbf{r},t) \cdot \nabla \} \mathbf{v}(\mathbf{r},t) = -en(\mathbf{r},t)\mathbf{E}(\mathbf{r},t)/m - \nabla p(\mathbf{r},t) \quad (1)$$

Here, ν is the electron collision frequency and $p(\mathbf{r},t)$ is the quantum pressure of the degenerate electron gas, which within the Thomas-Fermi approximation (Ref. 9) is given by

$$p(\mathbf{r},t) = \left[\frac{3}{8\pi} \right]^{2/3} (h^2/5m) n(\mathbf{r},t)^{5/3} \quad (2)$$

The third term on the lefthand side of the Euler equation is the convective current, which arises from the fact that the conduction electrons are a continuous medium in this model. The first term on the righthand side of Equation 1 is the Lorentz force, the magnetic term having been dropped within the electrostatic approximation. The last term is due to quantum pressure, which gives rise to a spatial variation (i.e., a screening) in the electron density near the microparticle surface in the presence of radiation. Thus, the response of the electron gas is nonlocal. The perturbed electron charge density, $n(\mathbf{r},t)$ obeys the equation of continuity,

$$\partial n(\mathbf{r},t)/\partial t + \nabla \cdot [n(\mathbf{r},t)\mathbf{v}(\mathbf{r},t)] = 0 \quad (3)$$

The incident electric component of the laser radiation field $\mathbf{E}_0(\mathbf{r},t)$ is given by

$$\mathbf{E}_0(\mathbf{r},t) = \mathbf{e}_1 A_1 \exp[i(\mathbf{k}_1 \cdot \mathbf{r} - \omega_1 t)] + \mathbf{e}_2 A_2 \exp[i(\mathbf{k}_2 \cdot \mathbf{r} - \omega_2 t)] + cc \quad (4)$$

where \mathbf{e}_j , A_j , \mathbf{k}_j and ω_j ($j = 1,2$) are the incident unit polarization vector, electric field amplitude, wave vector and frequency of the j^{th} laser beam. The total electric field amplitude, $\mathbf{E}(\mathbf{r},t)$, in Equation 1 is driven by the perturbed charge density inside the microparticle. Within the quasi-static approximation $\mathbf{E}(\mathbf{r},t) = -\nabla \phi(\mathbf{r},t)$ where $\phi(\mathbf{r},t)$ is the electrostatic potential. Outside the microparticle, the Laplace equation holds

$$\nabla^2 \phi(\mathbf{r},t) = 0 \quad (5a)$$

Inside the microsphere, the electrostatic potential obeys Poisson's equation

$$\nabla^2 \phi(r,t) = 4\pi en(r,t)/\epsilon_b \quad (5b)$$

where the electrostatic potential is coupled to Equations 1 and 3 via $n(r,t)$, and ϵ_b is the dielectric constant of the rigid jellium background. Equation 5a and b must be supplemented with the usual electrostatic boundary conditions, namely that $\phi(r,t)$ and $\epsilon \partial \phi(r,t)/\partial r$ are continuous at the surface. Since the Euler equation and the equation of continuity are coupled together, only one additional boundary condition (ABC) is required, which is usually chosen to be the acoustic condition to ensure that no electrons flow across the boundary; viz., the radial component of the electron drift velocity will vanish at the surface. These boundary conditions can be followed without any difficulties in determining the linear response of the microparticle to laser light. However, in the next order of perturbation theory, difficulties can arise in the presence of the monopole response (Ref. 9). Specifically, if one demands that the second-order radial velocity vanish at the microparticle's surface, then the integral of the second-order perturbed electron density over the volume of the microparticle will deviate from zero. In turn, this implies that the calculation does not conserve charge and reflects the fact that there are basic inconsistencies in describing the microparticle response by means of a relaxation model (Refs. 10,11,12). Here, a different additional boundary condition is used for monopole responses, namely, that charge is conserved in every order of perturbation theory. If this is done, then the second-order radial velocity will deviate from zero at the microparticle's surface. Calculations in Section 3.2.3 show that within a screening length of the surface, the ratio of the radial velocity at the surface to the maximum velocity is on the order of v/ω_{\pm} , where ω_{\pm} is the frequency of the radiation generated by the microparticle via nonlinear mixing processes. Thus, so long as $v/\omega_{\pm} \ll 1$, this inconsistency is not significant.

An examination of Equations 1 and 2 reveals four nonlinear terms in the Euler equation for the electron drift velocity: (1) the electron current, (2) the convective current (3) the Lorentz force, and (4) the quantum pressure.

The electron density, drift velocity, quantum pressure, and the electrostatic potential can be decomposed into the different possible frequency components. Thus, if $\alpha(r,t)$ is any of these quantities, then

$$\begin{aligned}
\alpha(r,t) = & \alpha_0 + \alpha_1(r,\omega_1) \exp(-i\omega_1 t) + \alpha_1(r,\omega_2) \exp(-i\omega_2 t) \\
& + \alpha_2(r,\omega_-) \exp(-i\omega_- t) + \alpha_2(r,\omega_+) \exp(-i\omega_+ t) + \alpha_2(r,0) \\
& + \alpha_2(r,2\omega_1) \exp(-2i\omega_1 t) + \alpha_2(r,2\omega_2) \exp(-2i\omega_2 t) \\
& + \alpha_3(r,\omega_1) \exp(-i\omega_1 t) + \alpha_3(r,\omega_2) \exp(-i\omega_2 t) + \text{c.c.}
\end{aligned}
\tag{6}$$

where α_0 is the equilibrium value, α_1 are the linear response at fundamental frequencies and the α_2 s are the sum ($\omega_+ = \omega_1 + \omega_2$), difference ($\omega_- = \omega_1 - \omega_2$) frequency, a rectified dc(0) and the second-harmonic ($2\omega_i$) contributions for the second-order response, and α_3 s are the fundamental frequency contributions for the third-order response.

2.1 LINEAR RESPONSE

Inserting the perturbative expansion, i.e., Equation 6 into Equations 1 through 5, shows that the induced linear density satisfies the following equation

$$[\nu^2 - q^2(\omega)] n_1(r,\omega) = 0 \tag{7a}$$

In Equation 7a, $q(\omega)$ is the self-consistent, frequency-dependent screening wave vector, which is given by

$$q(\omega) = [\omega_p^2 - \omega(\omega + i\nu)]^{1/2}/\beta \tag{7b}$$

where $\omega_p = (4\pi n_0 e^2 / m \epsilon_b)^{1/2}$ is the plasma frequency and $\beta^2 = 0.6 v_F^2$ with v_F the Fermi velocity. In the low-frequency limit, the screening wave vector becomes real and reduces to the Thomas-Fermi value, $q_{TF} = \omega_p / \beta$. In this limit, the field barely penetrates into the particle and the electron density is uniform everywhere, except in the immediate vicinity of the particle's surface. In the high-frequency limit, i.e., $\omega \geq \omega_p$, $q(\omega)$ has an imaginary part, the electron density is oscillatory.

Explicit expressions for the first-order electron density, electric field as well as the drift velocity are given in Appendix A.

2.2 SECOND-ORDER RESPONSE

To determine the quadratic response of the electron gas to two nondegenerate laser beams oscillating at ω_1 and ω_2 , insert the expressions for the linear electron density, drift velocity and electric field into Equations 1 and 3 and extract those terms that are oscillating at ω_{\pm} for sum (ω_+) and difference (ω_-) frequency generation. This leads to the following equation for the second-order electron density response oscillating at ω_{\pm} :

$$[\nabla^2 - q^2(\omega_{\pm})]n_2(r, \omega_{\pm}) = -\beta^{-2}\nabla \cdot S(r; \omega_1, \pm\omega_2) \quad (8)$$

where the drive terms $S(r; \omega_1, \pm\omega_2)$ are defined by

$$\begin{aligned} S(r; \omega_1, \pm\omega_2) = & i\omega_1 n_1(r, \omega_1) v_1(r, \pm\omega_2) \pm i\omega_2 n_1(r, \omega_1) v_1(r, \pm\omega_2) \\ & + n_0 [v_1(r, \omega_1) \cdot \nabla] v_1(r, \pm\omega_2) + n_0 [v_1(r, \pm\omega_2) \cdot \nabla] v_1(r, \omega_1) \\ & + e/m [n_1(r, \omega_1) E_1(r, \pm\omega_2) + n_1(r, \pm\omega_2) E_1(r, \omega_1)] \\ & + (2\beta^2/3n_0) \nabla [n_1(r, \omega_1) n_1(r, \pm\omega_2)] \end{aligned} \quad (9)$$

The linear response $n_1(r, \omega)$, $v_1(r, \omega)$ and $E_1(r, \omega)$ are all enhanced at the surface mode frequencies ω_s . The drive term $S(r; \omega_1, \pm\omega_2)$ may be doubly enhanced for ω_1 and ω_2 near ω_s , since $S(r; \omega_1, \pm\omega_2)$ is a bilinear product of linear responses at ω_1 and ω_2 . For compact notation, denote $S(r; \omega_1, \pm\omega_2)$ as $S_{\pm}(r)$. The first two terms in $S_{\pm}(r)$ arise from the second-order electron current, the next two are from the second-order convective current, the fifth and sixth terms arise from the second-order Lorentz force, while the last term arises from the second-order quantum pressure. The explicit expression for the drive terms are given by

$$S_{\pm}(r) = \frac{r_{\pm} \beta^2}{q_{\pm} a^2} [\hat{r} S_r^{\pm}(r) + \hat{\theta} S_{\theta}^{\pm}(r) + \hat{\phi} S_{\phi}^{\pm}(r)] \quad (10)$$

with

$$\begin{aligned}
S_r^\pm(r) = & (4\pi/9)^{1/2} S_{r00}^\pm(r) n \sin \theta_2 Y_{00}(\theta) \\
& + (16\pi/45)^{1/2} S_{r20}^\pm(r) n \sin \theta_2 Y_{20}(\theta) \\
& - (2\pi/15)^{1/2} S_{r21-}^\pm(r) n \cos \theta_2 [Y_{21}(\theta, \phi) - Y_{2-1}(\theta, \phi)] \\
& + i(2\pi/15)^{1/2} S_{r21+}^\pm(r) \sin \theta_2 [Y_{21}(\theta, \phi) + Y_{2-1}(\theta, \phi)] \\
& - i(2\pi/15)^{1/2} S_{r,22}^\pm(r) \cos \theta_2 [Y_{22}(\theta, \phi) + Y_{2-2}(\theta, \phi)]
\end{aligned} \tag{11a}$$

$$\begin{aligned}
S_\theta^\pm(r) = & (4\pi/45)^{1/2} S_{\theta 20}^\pm(r) n \sin \theta_2 \frac{\partial}{\partial \theta} Y_{20}(\theta) \\
& - (2\pi/15)^{1/2} S_{\theta 21-}^\pm(r) n \cos \theta_2 \frac{\partial}{\partial \theta} [Y_{21}(\theta, \phi) - Y_{2-1}(\theta, \phi)] \\
& + i(2\pi/15)^{1/2} S_{\theta 21+}^\pm(r) \sin \theta_2 \frac{\partial}{\partial \theta} [Y_{21}(\theta, \phi) + Y_{2-1}(\theta, \phi)] \\
& - i(\pi/30)^{1/2} S_{\theta 22}^\pm(r) \cos \theta_2 \frac{\partial}{\partial \theta} [Y_{22}(\theta, \phi) - Y_{2-2}(\theta, \phi)]
\end{aligned} \tag{11b}$$

$$\begin{aligned}
S_\phi^\pm(r) = & - (2\pi/15)^{1/2} S_\phi^\pm(r, \pm \omega_2, \omega_1) n \cos \theta_2 \frac{1}{\sin \theta} \frac{\partial}{\partial \phi} [Y_{21}(\theta, \phi) \\
& - Y_{2-1}(\theta, \phi)] + i(2\pi/15)^{1/2} S_\phi^\pm(r, \omega_1, \pm \omega_2) \sin \theta_2 \frac{1}{\sin \theta} \frac{\partial}{\partial \phi} \\
& [Y_{21}(\theta, \phi) + Y_{2-1}(\theta, \phi)] - i(\pi/30)^{1/2} S_{\phi 22}^\pm(r) \cos \theta_2 \frac{1}{\sin \theta} \frac{\partial}{\partial \phi} \\
& [Y_{22}(\theta, \phi) - Y_{2-2}(\theta, \phi)]
\end{aligned} \tag{11c}$$

where the different components $S_{\mu m}^\pm(r)$ are given in Appendix B (Equations B.1). Also explicit expressions for the second-order electric field as well as the electron density and velocity are contained in Appendix B.

Similar expressions can be obtained for the dc rectified and second-harmonic contributions.

2.3 THIRD-ORDER RESPONSE

To determine the third-order response of the electron gas to two nondegenerate laser beams oscillating at ω_1 and ω_2 , insert the expressions for the linear and quadratic electron density, drift velocity, and electric field into Equations 1 and 3 and extract those terms that are oscillating at ω_1 and ω_2 fundamental frequency generation. This leads to the following equation for the third-order electron density response oscillating at ω_i :

$$[\nabla^2 - q^2(\omega_i)]n_3(r, \omega_i) = -\beta^{-2}\nabla \cdot T(r; \omega_i) \quad (12)$$

where $i = 1$ or 2 and the drive terms $T(r; \omega_i)$ are defined by

$$\begin{aligned} T(r; \omega_1) = & T^{(2)}(r, \omega_2 + \omega_-) + T^{(2)}(r, \omega_1 + 0) + T^{(2)}(r, -\omega_2 + \omega_+) \\ & + T^{(2)}(r, -\omega_1 + 2\omega_1) + T^{(1)}(r, \omega_1, \omega_2, -\omega_2) \\ & + T^{(1)}(r, \omega_1, \omega_1, -\omega_1) \end{aligned} \quad (13a)$$

$$\begin{aligned} T(r; \omega_2) = & T^{(2)}(r, \omega_1 - \omega_-) + T^{(2)}(r, \omega_2 + 0) + T^{(2)}(r, -\omega_1 + \omega_+) \\ & + T^{(2)}(r, -\omega_2 + 2\omega_2) + T^{(1)}(r, \omega_2, \omega_1, -\omega_1) \\ & + T^{(1)}(r, \omega_1, \omega_2, -\omega_2) \end{aligned} \quad (13b)$$

where

$$T^{(2)}(r, \omega_i + 0) = T^{(2)}(r, \omega_i + (\omega_1 - \omega_1)) + T^{(2)}(r, \omega_i + (\omega_2 - \omega_2)) \quad (13c)$$

In Equation 13a, the first cascade term is given by

$$\begin{aligned}
T^{(2)}(r, \omega_2 + \omega_-) = & i\omega_2 n_1(r, \omega_2) v_2(r, \omega_-) + i\omega_- n_2(r, \omega_-) v_1(r, \omega_2) \\
& + n_0 [v_1(r, \omega_2) \cdot \nabla] v_2(r, \omega_-) + n_0 [v_2(r, \omega_-) \cdot \nabla] v_1(r, \omega_2) \\
& + e/m [n_1(r, \omega_2) E_2(r, \omega_-) + n_2(r, \omega_-) E_1(r, \omega_2)] \\
& + (2\beta^2/3n_0) \nabla [n_1(r, \omega_2) n_2(r, \omega_-)]
\end{aligned} \tag{14a}$$

and the first direct term is given by

$$\begin{aligned}
T^{(1)}(r, \omega_1, \omega_2, -\omega_2) = & n_1(r, \omega_1) [v_1(r, \omega_2) \cdot \nabla] v_1(r, -\omega_2) + c.c.] \\
& + n_1(r, \omega_2) [v_1(r, -\omega_2) \cdot \nabla] v_1(r, \omega_1) \\
& + (v_1(r, \omega_1) \cdot \nabla) v_1(r, -\omega_2)] \\
& + n(r, -\omega_1) [(v_2(r, \omega_1) \cdot \nabla) v(r, \omega_1) \\
& + v_1(r, \omega_2) \cdot \nabla] v_1(r, \omega_1)]
\end{aligned} \tag{14b}$$

and similar expressions can be obtained for the other terms in Equations 13.

The linear responses $n_1(r, \omega_1)$, $v_1(r, \omega_1)$ and $E_1(r, \omega_1)$ are all enhanced at the surface mode frequencies ω_s . The second-order responses $n_2(r, \omega_-)$, $v_2(r, \omega_-)$, and $E_2(r, \omega_-)$ may be doubly enhanced for ω_1 and ω_2 near ω_s . The first two terms in Equation 14a arise from the electron current, the next two are from the convective current, the fifth and sixth terms arise from the Lorentz force, while the last term arises from the second-order quantum pressure. All the terms appearing in Equation 14b arise from the convective current. The explicit expression for the drive terms can be worked out.

In Equations 13, the driving terms $T^{(2)}$ and $T^{(1)}$ come from the products of the second-order fields and the linear fields as well as the triple products of the linear fields. The driving terms $T^{(2)}$ and $T^{(1)}$ can be further broken down into self-action terms and cross-action terms. The self-action term and cross-action term in $T^{(1)}$ at ω_1 are $T^{(1)}(r, \omega_1, \omega_1, -\omega_1)$ and $T^{(1)}(r, \omega_1, \omega_2, -\omega_2)$, respectively. The self-action terms in $T^{(2)}$ are $T^{(2)}(r, \omega_1 + (\omega_1 - \omega_1))$ and $T^{(2)}(r, -\omega_1 + 2\omega_1)$, which come from the product of the self-rectified and self-second-harmonic fields and linear fields. The cross-action terms in $T^{(2)}$ at ω_1 are $T^{(2)}(r, \omega_2 + \omega_-)$, $T^{(2)}(r, \omega_1 + (\omega_2 - \omega_2))$, and $T^{(2)}(r, -\omega_2 + \omega_+)$, which are, respectively, from the product of the difference frequency, cross-rectified, and sum frequency fields and linear fields. The same classification is applied for $T^{(2)}$ and $T^{(1)}$ at ω_2 . The terms in $T^{(2)}$ resulting from the products of the difference and sum frequency fields and linear fields are also known as "coherent coupling" terms, since they are important for the coherent waves.

Accordingly, all the third-order responses, which include the third-order susceptibility, polarization, density, electric field, and velocity, can be classified from their corresponding driving terms. That is, there will be self-action and cross-action effects in third-order responses resulting from all possible combinations of second-order fields and first-order fields as well as the triple products of the linear fields.

3.0 ELECTRODYNAMICS OF MICROPARTICLE COMPOSITES

In this section, the macroscopic linear and nonlinear electrodynamic responses of a very dilute microparticle composite are investigated. The electrodynamic response of the microparticle composite is determined by the total field generated in the entire composite. For very dilute microparticle composites, each microparticle is in the far field of all the others and the single scattering approximation is valid. Hence, the total field of the composite is simply the sum of the far field generated by each particle.

The linear and nonlinear electrodynamic responses of the microparticle composite are determined by the induced linear and nonlinear polarization of the microparticles. The coherent part of the electrodynamic response is determined by the phase-matched amplitude of the microparticles, viz. the "optical theorem" (or the "Ewald-Oseen extinction theorem").

3.1 LINEAR ELECTRODYNAMICS

3.1.1 Scattering Amplitude in the Far Zone

In this section, the first-order electromagnetic fields in the radiation zone, which are generated by a single microsphere are determined. A microsphere at point $\mathbf{r}' = (x, y, z')$ scatters the two incident beams to generate a first-order field $E_s^{(1)}(\mathbf{r}, \omega_i)$ at the incident (ω_i) frequency at point $\mathbf{r} = (x, y, z)$, where $r \gg a$ in the radiation zone. The electromagnetic field associated with an oscillating dipole of the microsphere located at \mathbf{r}' , is given by

$$E_s^{(1)}(\mathbf{r}, \mathbf{r}', \omega_i) = \exp[i\phi(\mathbf{r}, \mathbf{r}')] f_i^{(1)}(\theta', \phi') / |\mathbf{r} - \mathbf{r}'| \quad (15)$$

where the phase $\phi(\mathbf{r}, \mathbf{r}')$ is given by

$$\phi(\mathbf{r}, \mathbf{r}') = k_i |\mathbf{r} - \mathbf{r}'| + \mathbf{k}_i \cdot \mathbf{r}' \quad (16)$$

and $k_i = [\epsilon_h(\omega_i)]^{1/2} \omega_i / c$ with $i = 1$ or 2 , the integration is over the volume $V' = 4\pi/3 a^3$ of the sphere at \mathbf{r}' . In the quasi-static limit where the radiation wavelength $\lambda \gg a$, the

phase factors in Equation 16 remain nearly constant within a given sphere. Hence, the scattering amplitude in Equation 15 is given by

$$f_i^{(1)}(\theta', \phi') = k_i^2 (n \times p^{(1)}) \cdot n \quad (17)$$

where n is the unit vector in the direction $(r-r')$, and the vector $p^{(1)}$ is the first-order dipole moment tensor induced by the laser light in a microparticle located at the origin, $\cos\theta' = (z-z')/r$ and $\tan\phi' = (y-y')/(x-x')$. Note that the dipole moment tensor $p^{(1)}$ can be extracted from the electrostatic field in the near zone for a small scatter. For a microsphere irradiated by laser beam at ω_i , the radiation-induced dipole moment is given in Appendix A (Equation A.7). Finally, the scattering amplitude, $f_i^{(1)}(\theta', \phi')$, for the electric field in the radiation zone, arising from a single microparticle is

$$f_1^{(1)}(\theta', \phi') = k_1^2 a^3 P^{(1)}(\omega_1) \{ \hat{\theta} [\cos\theta \sin\phi - n \sin\theta] - \hat{\phi} \cos\phi \} \quad (18a)$$

$$f_2^{(1)}(\theta', \phi') = k_2^2 a^3 P^{(1)}(\omega_2) \{ \hat{\theta} [\cos\theta_2 \cos\phi \cos\phi - \sin\theta_2 \sin\theta] - \hat{\phi} \cos\theta_2 \sin\phi \} \quad (18b)$$

where the incident frequency is at ω_i , and the polarization $P^{(1)}(\omega_i)$ is defined in Appendix A (Equation A.8).

The magnetic field components $B_s^{(1)}(r, r', \omega_i)$ are then given by

$$B_s^{(1)}(r, r', \omega_i) = n \times E_s^{(1)}(r, r', \omega_i) \quad (19)$$

so that the total intensity $I_s(r, r', \omega_i)$, for a single microparticle at r' is,

$$I_S^{(1)}(r, r', \omega_i) = (c/8\pi) |f_i^{(1)}(\theta', \phi')|^2 / |r - r'|^2 \quad (20)$$

3.1.2 Macroscopic Electromagnetic Fields and Intensities

In this section, the total linear electromagnetic fields and intensities arising from a tenuous collection of microparticles randomly distributed in a passive linear dielectric host are examined. In general, a collection of microparticles will scatter radiation with random phase with respect to one another. The resultant total linear electromagnetic field from a microparticle composite will be the sum of the coherent (or average) field and the incoherent (fluctuating) field (Ref. 13). The phase of the field will fluctuate randomly for arbitrary directions, so that the volume-averaged (or ensemble-averaged) incoherent field is zero. However, along a particular phase-matched (or coherent) direction, the different particles all scatter in phase with one another and the resultant average field is coherent. This coherent field will be discussed in Section 3.1.2.1. The average intensity for a microparticle composite is the sum of the coherent and incoherent intensities and will be examined in Section 3.1.2.2. A tenuous microsphere composite with the particles sufficiently far apart so that they do not affect each other will be considered. Then, the far-field and single scattering approximations are valid and the total field at a point r is the sum of the far field from each microsphere located at point r' , as depicted in Figure 1.

3.1.2.1 Coherent Field: Linear Dielectric Function. The linear coherent field at ω_i is given by the integral (or summation) of the far field of each sphere, which is given in Equation 15, over the entire composite, i.e.,

$$E_C^{(1)}(r, \omega_i) = \int_V dr' E_S^{(1)}(r, r', \omega_i) \quad (21a)$$

$$= N \int_{-\frac{1}{2}L}^{\frac{1}{2}L} dx' \int_{-\frac{1}{2}L}^{\frac{1}{2}L} dy' \int_{-\frac{1}{2}L}^{\frac{1}{2}L} dz' \exp[i\phi(r, r')] f_i^{(1)}(\theta', \phi') / |r - r'| \quad (21b)$$

where the composite is assumed to reside within a slab of dimensions $L \times L_y \times L_z$, where $L \ll L_y, L_z$ and $L_y L_z \rightarrow \infty$, but L remains finite and N is the microsphere number density. The prefactors, which include the scattering amplitude f_i and the propagator $1/|r-r'|$ vary slowly with r' in comparison to the rapidly-varying exponential factor, $\exp[i\phi(r, r')]$. The concern is with the limiting case in which $r \gg L$. To evaluate the integral for the y' -, and z' -coordinate first for the slab, the method of steepest descents (Refs. 15,16) will be used. The stationary phase point for the microsphere is located at $r_s = (r_s, \theta_s, \phi_s)$. The coordinates

$$\theta_s = \theta_i \quad (22a)$$

$$\phi_s = 0 \quad (22b)$$

and θ_i are the incident angles at ω_i .

Equations 22a and b indicate that the phase-matched direction for the linear response is in the forward direction.

Then, the coherent field at ω_2 in Equation 21 is given by

$$E_c^{(1)}(r, \omega_1) = - \hat{\theta} f L \frac{1}{\sin \theta_i} f_i^{(1)}(\theta_i | \theta_s, 0) \quad (23)$$

where $\hat{\theta}$ is unit polarization vector of the coherent electric field at point r far outside the slab and $f = N 4\pi a^3/3$ is the volume fraction of microspheres. In Equation 23, the forward scattering amplitude per unit volume f_i results from evaluation of the integral in Equation 21 at the stationary phase point and is given by

$$f_i^{(1)}(\theta_i | \theta_s, 0) = 2\pi i k_i p^{(1)}(\omega_i) \quad (24)$$

This general relation of the linear coherent field given in Equation 23, which is embodied in the forward scattering amplitude, is also called the "Optical Theorem" or the "Ewald-Oseen extinction theorem."

If the microparticle composite of thickness L is replaced by a homogeneous dielectric slab of same thickness with effective linear susceptibility χ_1 , then the electric field at point r outside the slab is given by

$$E(r, \omega_i) = 2\pi i k_i L \chi_1(\omega_i) A_i / \epsilon_h(\omega_i) \sin \theta_i \quad (25)$$

where the ω_i , A_i and θ_i are the incident frequency, field amplitude and angle, respectively.

Equating Equations 25 and 23, the effective linear dielectric function or susceptibility of the microparticle composite with volume fraction f is given by

$$\epsilon(\omega_i) = \epsilon_h(\omega_i) + 4\pi \chi_1(\omega_i) \quad (26a)$$

$$4\pi \chi_1(\omega_i) = 4\pi \epsilon_h(\omega_i) f P^{(1)}(\omega_i) \quad (26b)$$

where the microparticles are embedded in a passive linear dielectric material with the dielectric constant being $\epsilon_h(\omega_i)$.

3.1.2.2 Total Intensity: Linear Scattering. The total intensity from a slab of microparticle composite of thickness L is given by

$$I^{(1)}(r, \omega_i) = N \int_{-\frac{1}{2}L}^{\frac{1}{2}L} dx' \int_{-\infty}^{\infty} dy' \int_{-\infty}^{\infty} dx'' I_S^{(1)}(r, r', \omega_i) \quad (27)$$

where N is the microparticle number density and I_S is given in Equation 20. The total intensity can be decomposed into two parts, viz, the coherent and incoherent intensities. The coherent part is given by

$$I_C^{(1)}(r, \omega_i) = \frac{c}{8\pi} E_C^{(1)}(r, \omega_i) \times B_C^{(1)*}(r, \omega_i) \cdot \hat{r} \quad (28a)$$

$$= f^2 L^2 \frac{1}{\sin^2 \theta_i} \frac{\pi c}{2} k_i^2 |P^{(1)}(\omega_i)|^2 \quad (28b)$$

where

$B_C^{(1)} = \hat{r} \times E_C^{(1)}$ and $E_C^{(1)}$ is given in Equation 23. The incoherent part is given by

$$I_i^{(1)}(r, \omega_i) = \frac{c}{8\pi} N \int_{-\frac{1}{2}L}^{\frac{1}{2}L} dx' \int_{-\infty}^{\infty} dy' \int_{-\infty}^{\infty} dz' \frac{|f_i^{(1)}(\theta', \phi')|^2}{|r - r'|^2} \quad (29a)$$

where the x' , y' , and z' integrations can be easily evaluated, and the incoherent intensity is given by

$$I_i^{(1)}(r, \omega_i) = fL \frac{\pi^2 c}{6} k_i^4 a^3 |P^{(1)}(\omega_i)|^2 \quad (29b)$$

which is less than 1 percent of the incident intensity for volume fraction $f < 10^{-4}$.

3.1.3 Numerical Results and Discussion

The microparticles to be considered in the numerical calculation are silver spheres with radius $a > 20 \text{ \AA}$, where the quantum size effect is not important (Ref. 14). The background dielectric constant ϵ_b and the plasma frequency ω_p of the silver spheres are, respectively, 5.578 and 3.8 eV. The damping constant ν inside the silver sphere is modified by the free path effect (Ref. 14) and is given by

$$\nu = \nu_B + \frac{v_F}{a} \quad (30)$$

where $\nu_B = 0.01 \omega_p$ is the bulk damping constant and V_F is the Fermi velocity of the electrons.

For comparison, the linear responses are plotted in Figure 2 for a single silver sphere with $a = 100 \text{ \AA}$ in vacuum, which is irradiated by 0.3787 \mu m laser light of 1 MW intensity. The 0.3787 \mu m laser light can excite the surface dipole mode of the aforementioned silver sphere. Indeed, as shown in Figure 2(b), the electric field inside the sphere is enhanced by the surface dipole resonant denominator $D(\omega_s)$, whose magnitude is about 10, and is nearly $\pi/2$ out of the phase with respect to the incident electric field. Figure 2(c) depicts the radial velocity throughout the microsphere.

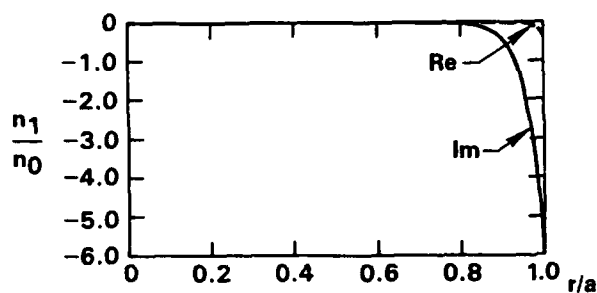
In Figures 3 through 10, the linear dielectric properties of the microsphere composites are shown. In particular, the calculations are done for the parameters appropriated for silver in water or glass substrate. The enhancement near the surface plasma mode of the spheres is clearly shown in all the linear dielectric properties, e.g., Figures 7 through 10. The higher enhancement factors will appear in the second-order and third-order nonlinear dielectric properties from the same local enhancement field.

All the nonlocal nature of the physical quantities will approach the local limit for the large $q_j a$. In Figure 5 the particle size dependence of the linear dielectric function of the microsphere composite is shown. The dielectric function has an enhancement from the nonlocality of the small sphere limit and approaches the local limits, which are indicated by the arrows in Figure 5, for large sphere limit. However, for extremely small spheres the dielectric function decreases and approaches the pure host limit. Note in Figure 5, the nonlocal nature is more pronounced for the smaller damping parameter, i.e., $\nu = 0.02 \omega_p$.

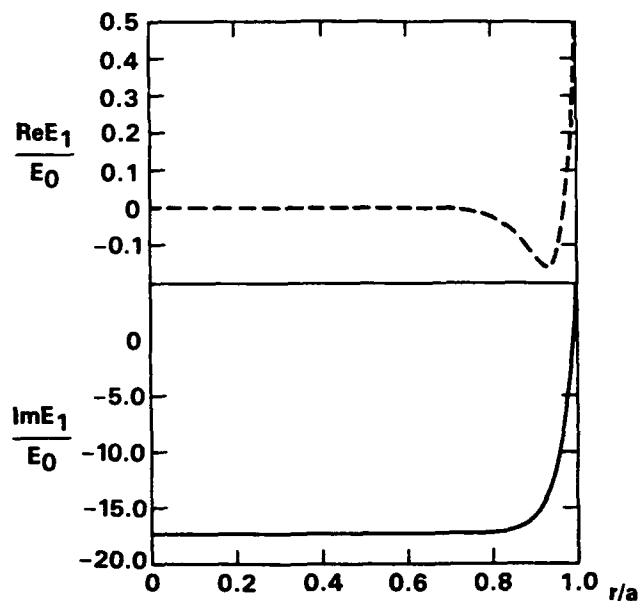
3.2 SUM AND DIFFERENCE FREQUENCY GENERATIONS

3.2.1 Scattering Amplitude and the Radiation in the Far Zone

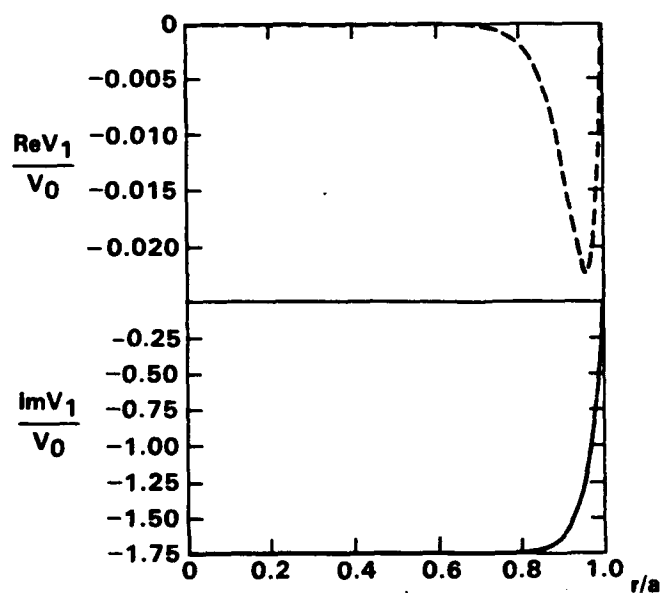
In this section, the second-order electromagnetic fields in the radiation zone, which are generated by a single microsphere are determined. A microsphere at point $\mathbf{r}' = (x, y, z')$ scatters the two incident beams, to generate a second-order field $E_s^{(2)}(\mathbf{r}, \omega_{\pm})$ at the sum (ω_+) or difference (ω_-) frequency at point $\mathbf{r} = (x, y, z)$, where $r \gg a$



(a) Electron density profile
 $n_0 = 3.08 \times 10^{18} \text{ cm}^{-3}$.



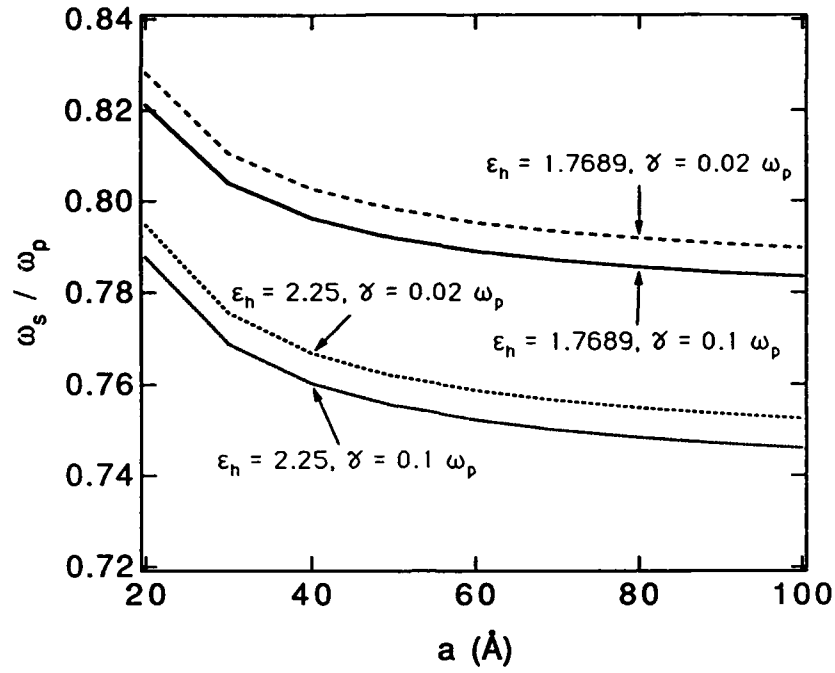
(b) Radial electric field.



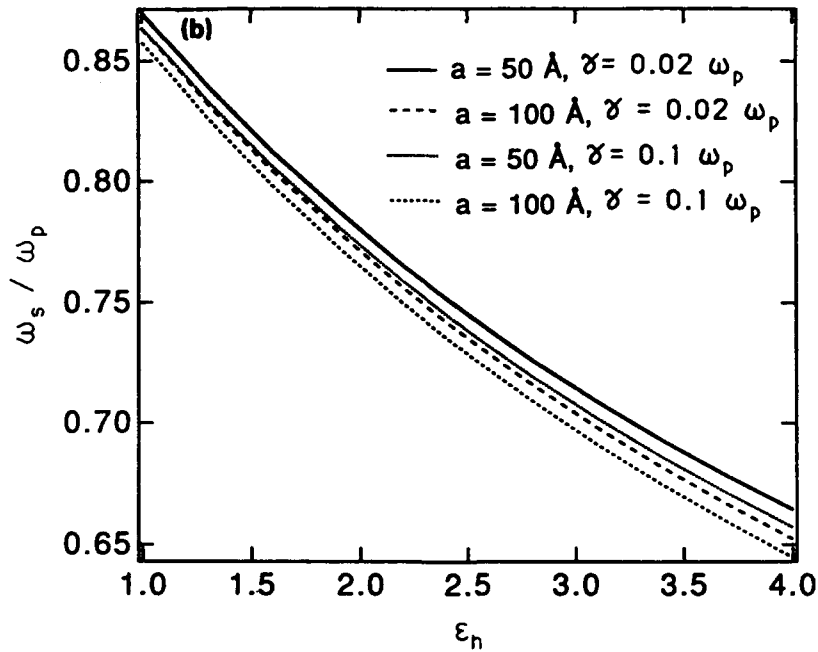
(c) Radial velocity ($V_0 = 0.84 \times 10^5 \text{ cm/s}$).

Figure 2.

Linear responses of a single silver sphere versus r/a , $a = 100 \text{ \AA}$. The incident laser light is 1 MW at 0.3787 \mu m . The magnitude of the incident electric field is $E_0 = 0.92 \times 10^2 \text{ stat V/cm}$.

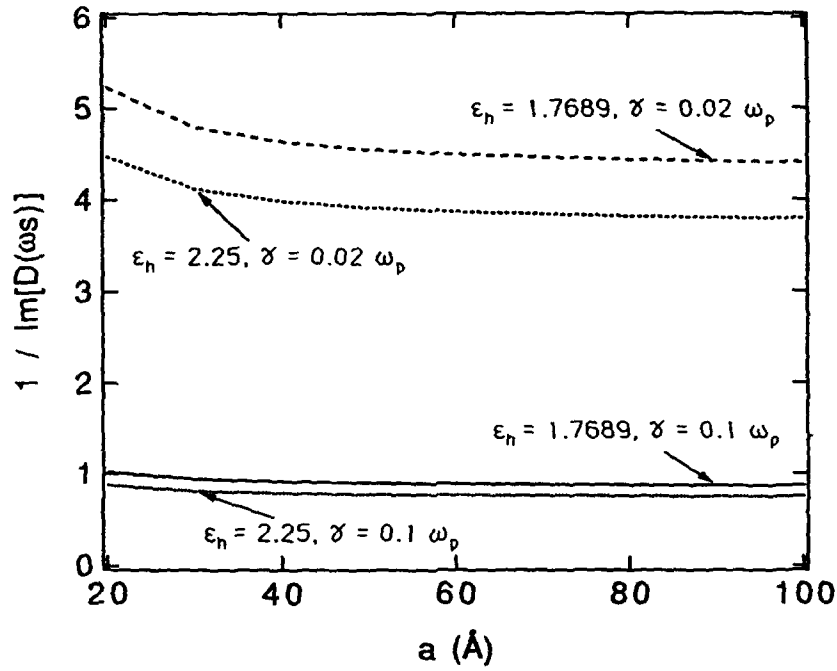


(a) Surface plasma resonant frequency versus sphere radius. The host material is either water ($\epsilon_h = 1.7689$) or glass ($\epsilon_h = 2.25$).

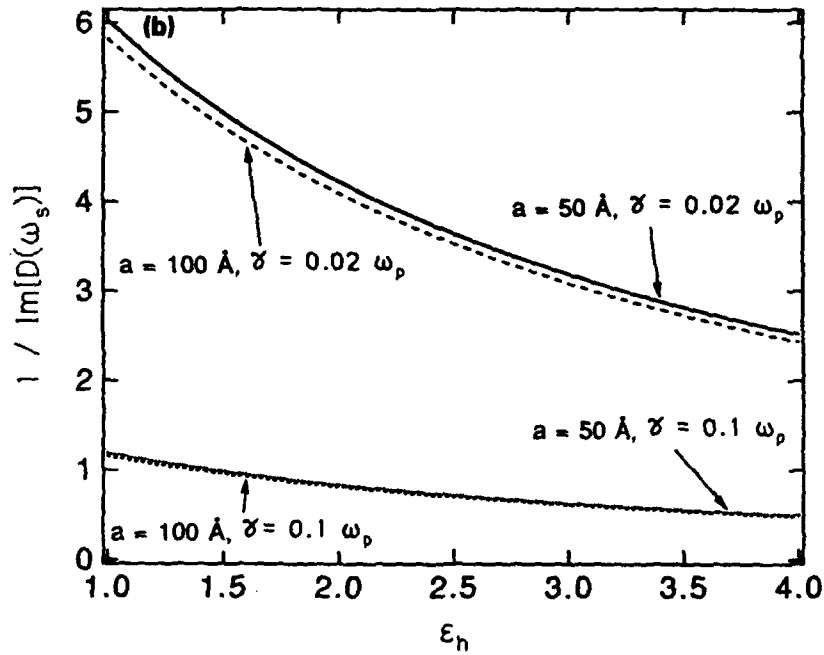


(b) Surface plasma resonant frequency versus host dielectric constant for radius being 50 Å or 100 Å. The damping parameter (γ) is either $0.02 \omega_p$ or $0.1 \omega_p$. The plasma frequency is 3.8 eV. The background dielectric constant (ϵ_b) of the sphere is 5.578.

Figure 3. Surface plasma resonant frequency versus sphere radius.

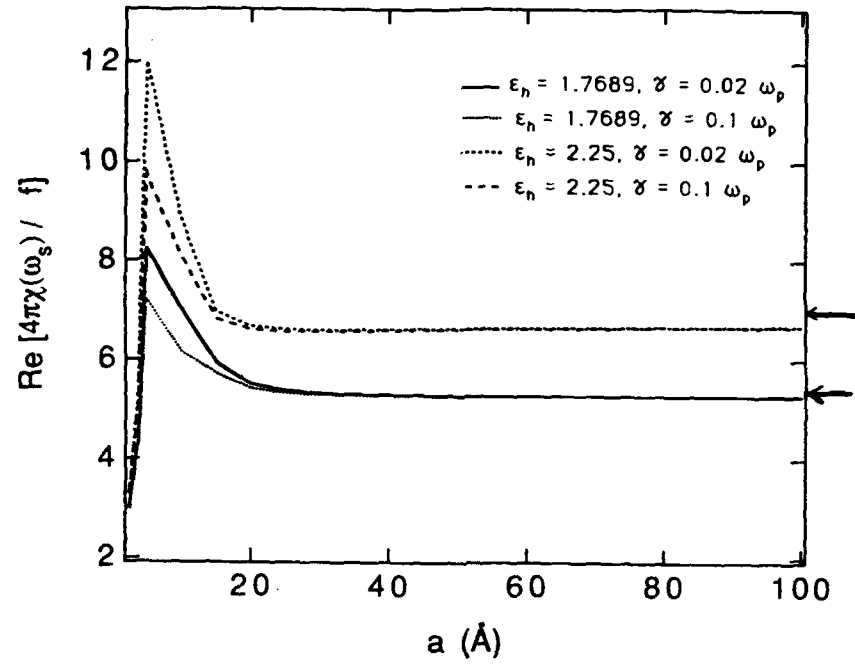


(a) The local field enhancement factor at the surface plasma resonant frequency versus sphere radius.

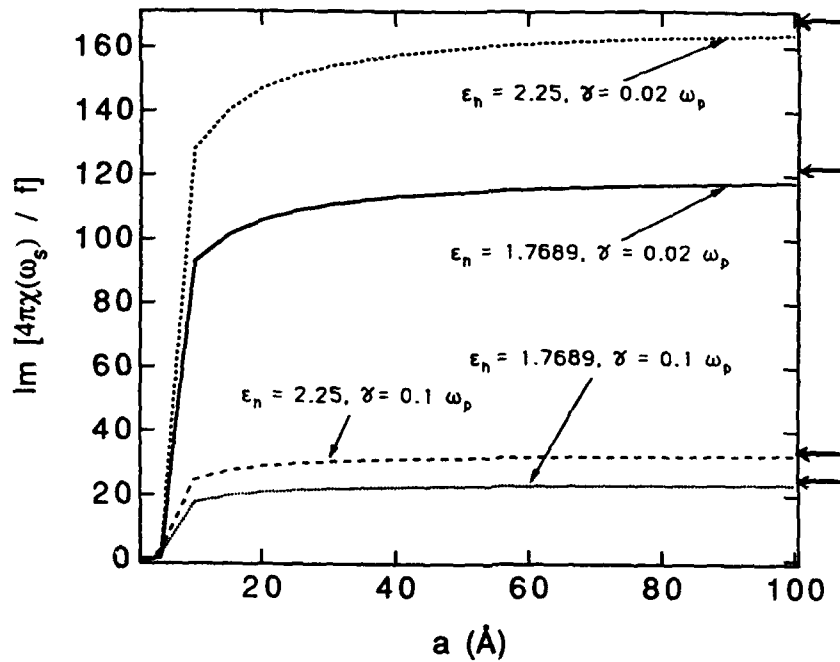


(b) The local field enhancement factor at the surface plasma resonant frequency versus the host dielectric constant. The parameters for the spherical particle are the same as used in Figure 3.

Figure 4. The local field enhancement factor.

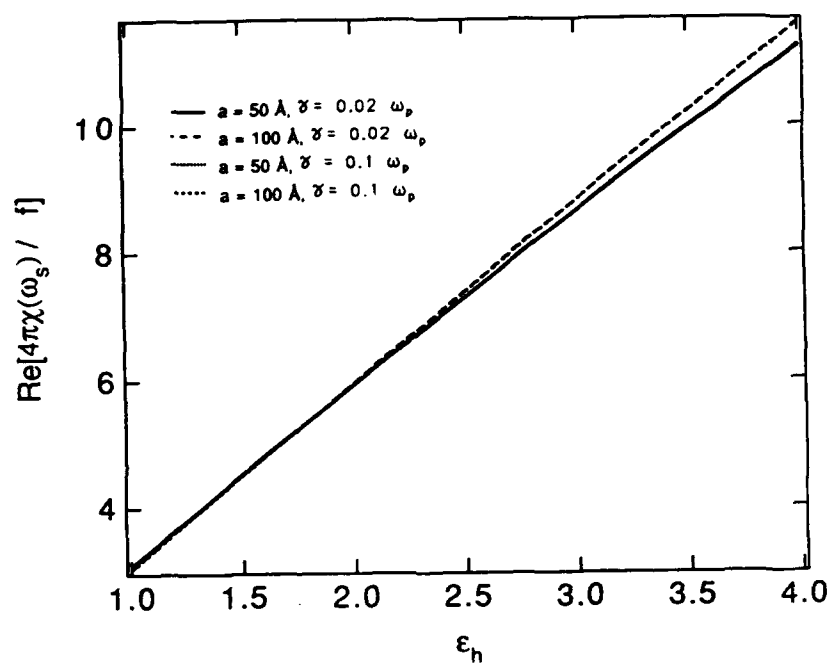


(a) Real part

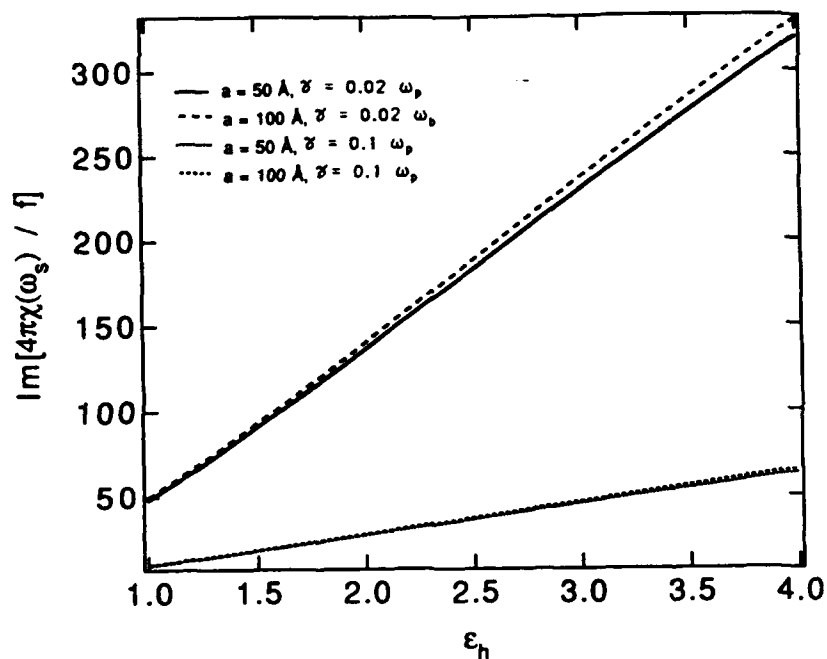


(b) Imaginary part

Figure 5. The particle size dependence of the real and imaginary parts of the dielectric function of the microspheres in water or glass with the damping parameter $\gamma = 0.02 \omega_p$ or $0.1 \omega_p$. The parameters for the spherical particles the same as used in Figure 3.

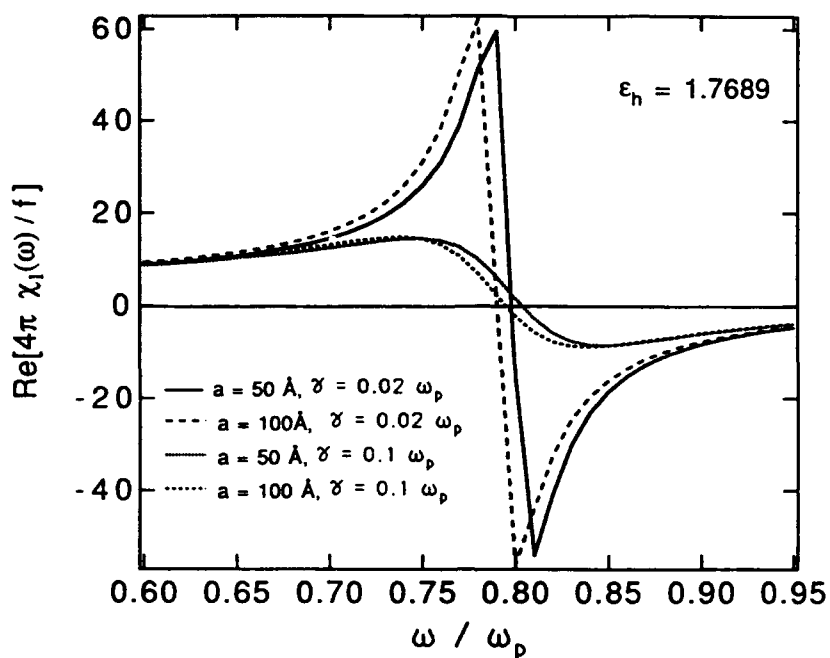


(a) Real part

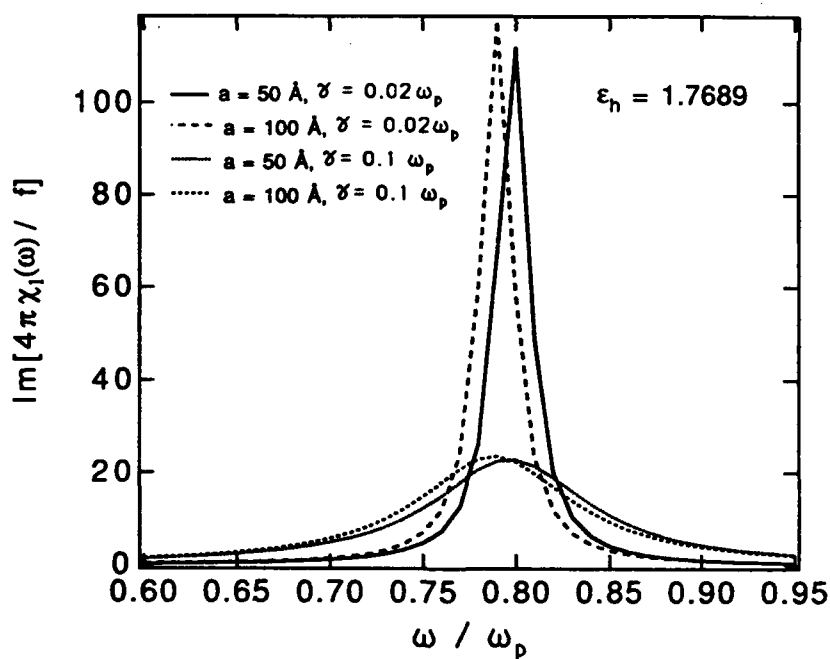


(b) Imaginary part

Figure 6. The host dielectric constant dependence of the real and imaginary parts of the dielectric function of the microspheres for radius 50 Å or 100 Å. The parameters for the spherical particle are the same as used in Figure 3.



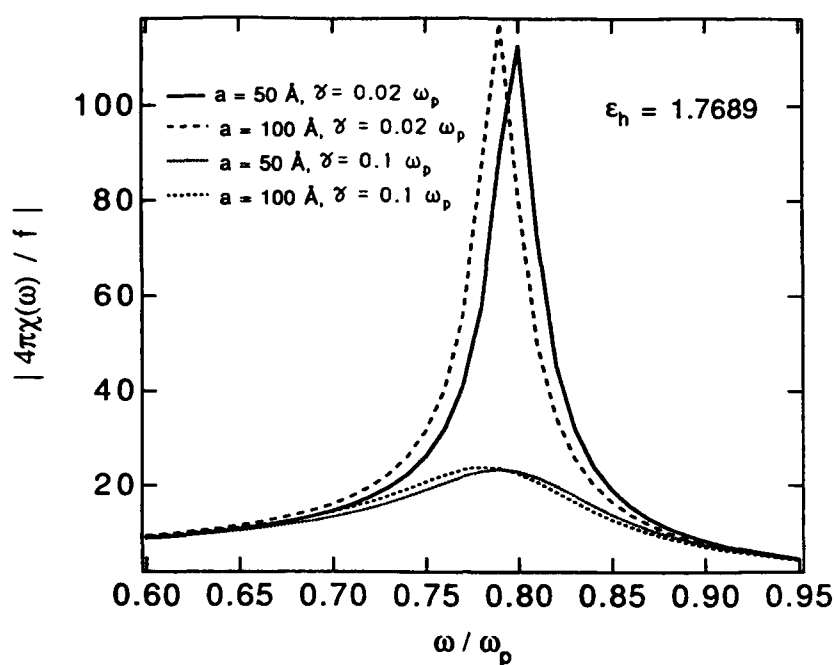
(a) Real part



(b) Imaginary part

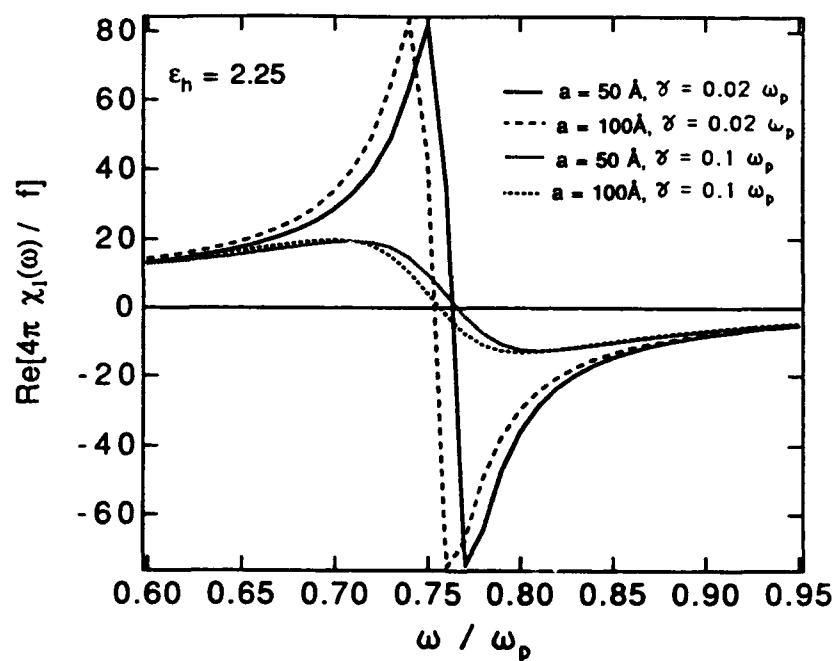
Figure 7.

The frequency dependence of the real and imaginary parts as well as absolute value of dielectric function of microspheres in water. The values of the dielectric function are normalized by the volume fraction f .



(c) Absolute value

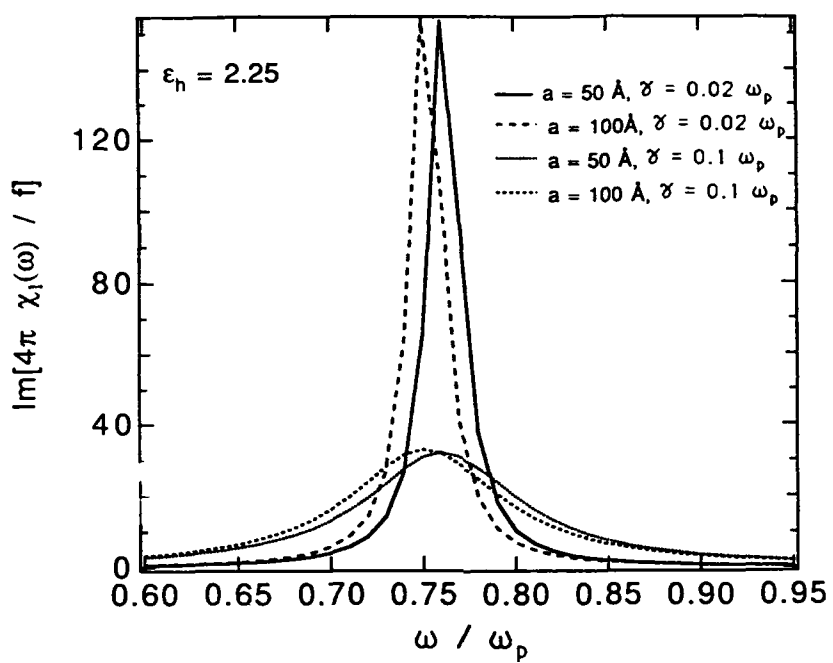
Figure 7. (Concluded)



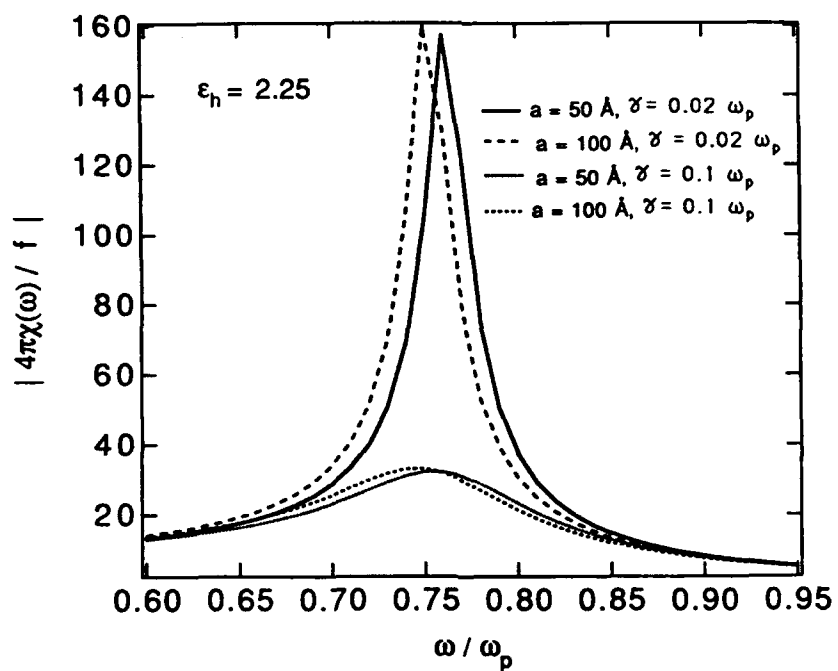
(a) Real part

Figure 8.

The frequency dependence of the real and imaginary parts as well as absolute value of the dielectric function of microspheres in glass.

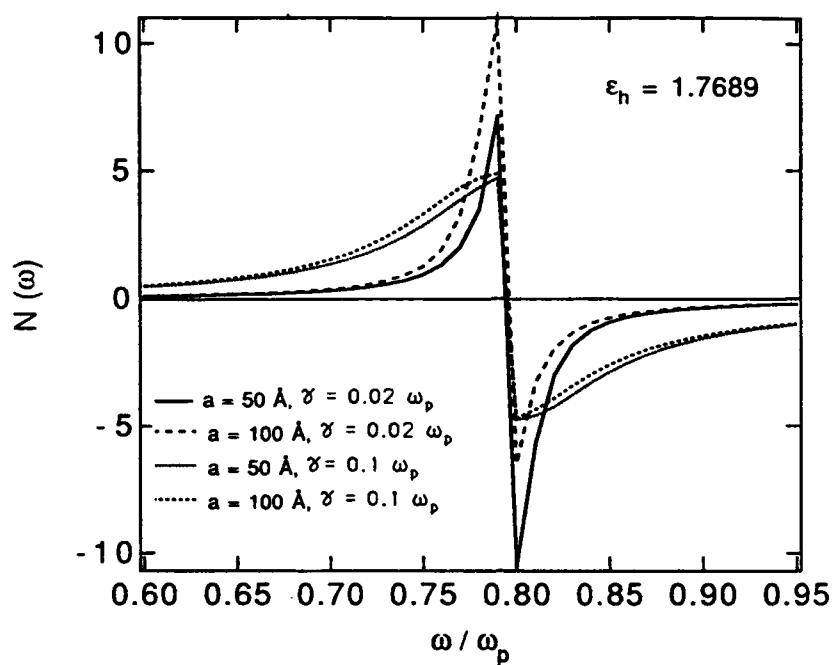


(b) Imaginary part

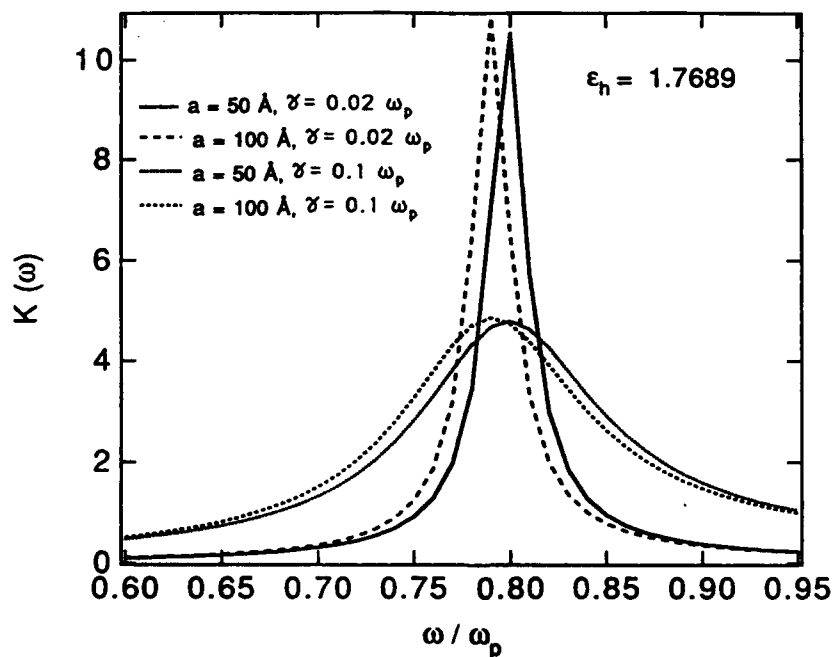


(c) Absolute value

Figure 8. (Concluded)

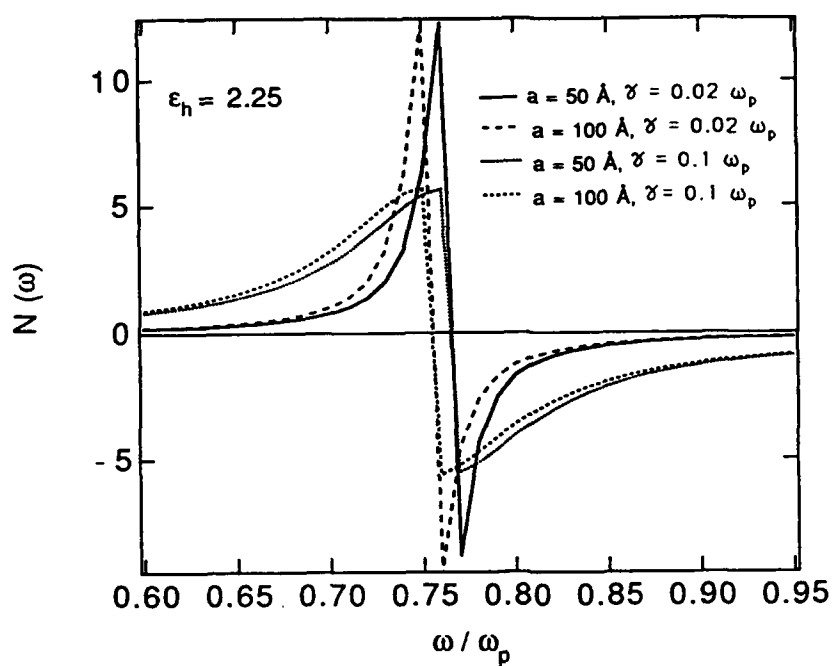


(a) Refractive index

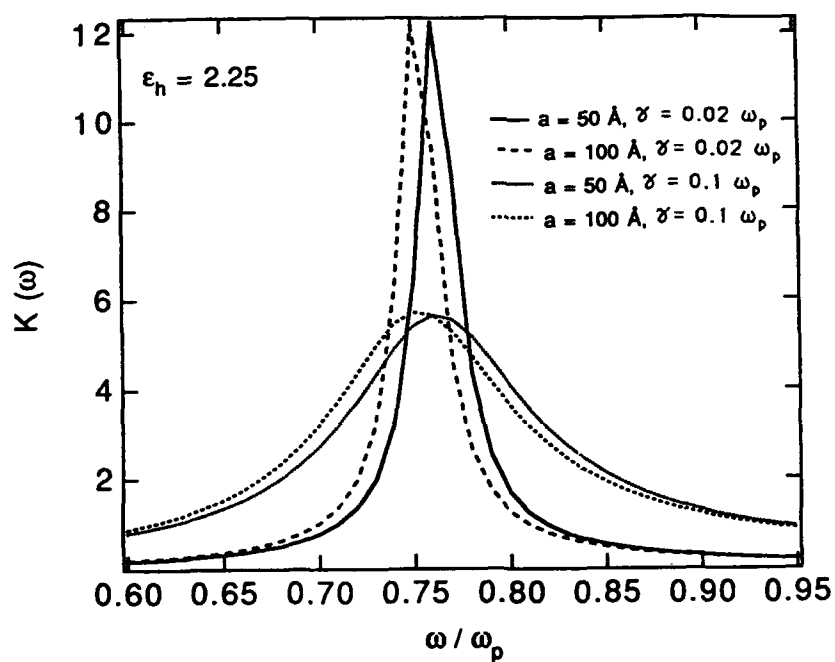


(b) Extinction coefficient

Figure 9. The frequency dependence of the refractive index and the extinction coefficient in water. The values are normalized by the volume fraction f .



(a) Refractive index



(b) Extinction coefficient

Figure 10. The frequency dependence of the refractive index and the extinction coefficient in glass.

in the radiation zone. The electromagnetic field associated with an oscillating quadrupole of the microsphere located at \mathbf{r}' , is given by

$$E_s^{(2)}(\mathbf{r}, \mathbf{r}', \omega_{\pm}) = \exp[i\phi(\mathbf{r}, \mathbf{r}')] f_{\pm}^{(2)}(\theta', \phi') / |\mathbf{r} - \mathbf{r}'| \quad (31)$$

where the phase $\phi(\mathbf{r}, \mathbf{r}')$ is given by

$$\phi(\mathbf{r}, \mathbf{r}') = k_{\pm} |\mathbf{r} - \mathbf{r}'| + (\mathbf{k}_1 \pm \mathbf{k}_2) \cdot \mathbf{r}' \quad (32)$$

and $k_{\pm} = [\epsilon_h(\omega_{\pm})]^{1/2} \omega_{\pm} / c$ the integration is over the volume $V' = 4\pi/3 a^3$ of the sphere at \mathbf{r}' . In the quasi-static limit where the radiation wavelength $\lambda \gg a$, the phase factors in Equation 32 remain nearly constant within a given sphere. Hence, the scattering amplitude in Equation 31 is given by

$$f_{\pm}^{(2)}(\theta, \phi) = -i(k_{\pm}^3/2) (n_x Q(n)/3) x n \quad (33)$$

where the vector $\mathbf{Q}(n)$ is defined by

$$Q_{\mu} (n_{\nu}) = \sum Q_{\mu\nu} n_{\nu} \quad (34)$$

$Q_{\mu\nu}$ is the second-order quadrupole moment tensor induced by the laser light in a microparticle located at the origin, $\cos\theta' = (z-z')/r$ and $\tan\phi' = (y-y')/(x-x')$. Note that the quadrupole moment tensor \mathbf{Q} can be extracted from the electrostatic field in the near zone for a small scatter. For a microsphere irradiated by two laser beams oriented at an

angle of θ_2 with respect to each other, the radiation-induced quadrupole moment tensor is given by

$$Q = \begin{vmatrix} 0 & 0 & Q_{xz} \\ 0 & 0 & 0 \\ Q_{zx} & 0 & Q_{zz} \end{vmatrix} \quad (35)$$

where $Q_{\mu\nu} = Q_{\nu\mu}$. Explicit formulas for $Q_{\mu\nu}$ are given in Appendix B (Equation B.17). Finally, the scattering amplitude, $f_{\pm}^{(2)}(\theta', \phi')$, for the electric field in the radiation zone, arising from a single microparticle is

$$\begin{aligned} f_{\pm}^{(2)}(\theta', \phi') = & ik_{\pm}^3 a^5 [2\pi e r_{\pm} / (3\epsilon_h(\omega_{\pm}) + 2\epsilon_b)] \{ \hat{\theta} [-\sin\theta_2 \sin 2\theta' U_{20}^{\pm} / 2 \\ & + \cos\theta_2 \cos 2\theta' \cos\phi' U_{21}^{\pm}] - \hat{\phi} \cos\theta_2 \cos\theta' \sin\phi' U_{21}^{\pm} \} \end{aligned} \quad (36)$$

Note that in the collinear and copolarized limit ($\theta_2 = \pi/2$), the scattering amplitude has a component only in the θ -direction. The functions U_{lm}^{\pm} are dimensionless, are related to weighed averages of the various components of the charge density over the sphere and are defined in Appendix B. Numerical results for U_{20}^{\pm} as a function of particle sizes will be discussed in Section 3.2.3.

The magnetic field components $B_s^{(2)}(r, r', \omega_{\pm})$ are then given by

$$B_s^{(2)}(r, r', \omega_{\pm}) = n \times E_s^{(2)}(r, r', \omega_{\pm}) \quad (37)$$

so that the total intensity $I_s^{(2)}(r, r', \omega_{\pm})$, for a single microparticle at r' is,

$$I_s^{(2)}(r, r', \omega_{\pm}) = (c/8\pi) |f_{\pm}^{(2)}(\theta', \phi')|^2 / |r - r'|^2 \quad (38)$$

where $Q(n)$ is defined in Equation 33.

3.2.2 Macroscopic Electromagnetic Fields and Intensities

In this section, the total second-order electromagnetic fields and intensities arising from a tenuous collection of microparticles randomly distributed in a passive linear dielectric host are examined. In general, a collection of microparticles will scatter radiation with random phase with respect to one another. The resultant total second-order electromagnetic field from a microparticle composite will be the sum of the coherent (or average) field and the incoherent (fluctuating) field (Ref. 13). The phase of the field will fluctuate randomly for arbitrary directions, so that the volume-averaged (or ensemble-averaged) incoherent field is zero. However, along a particular phase-matched (or coherent) direction, the different particles all scatter in phase with one another and the resultant average field is coherent. This coherent field will be discussed in Section 3.2.2.1. The average intensity for a microparticle composite is the sum of the coherent and incoherent intensities and will be examined in Section 3.2.2.2. A tenuous microsphere composite with the particles sufficiently far apart so that they do not affect each other will be considered. Then, the far-field and single scattering approximations are valid and the total field at a point r is the sum of the far field from each microsphere located at point r' , as depicted in Figure 1.

3.2.2.1 Coherent Field: Coherent Generation. The second-order coherent field at ω_{\pm} is given by the integral (or summation) of the far field of each sphere, which is given in Equation 31, over the entire composite, i.e.,

$$E_C^{(2)}(r, \omega_{\pm}) = \int_V dr' E_s^{(2)}(r, r', \omega_{\pm}) \quad (39a)$$

$$= N \int_{-\frac{1}{2}L}^{\frac{1}{2}L} dx' \int_{-\frac{1}{2}L}^{\frac{1}{2}L} dy' \int_{-\frac{1}{2}L}^{\frac{1}{2}L} dz' \exp[i\phi(r, r')] f_{\pm}^{(2)}(\theta', \phi') / |r - r'| \quad (39b)$$

where the composite is assumed to reside within a slab of dimensions $L \times L_y \times L_z$, where $L \ll L_y, L_z$ and $L_y L_z \rightarrow \infty$, but L remains finite and N is the microsphere number density. The prefactors, which include the scattering amplitude $f_{\pm}^{(2)}$ and the propagator $1/|r-r'|$ vary slowly with r' in comparison to the rapidly-varying exponential factor, $\exp[i\phi(r, r')]$. The concern is with the limiting case in which $r \gg L$. To evaluate the integral for the y' -, and z' -coordinate first for the slab, the method of steepest descents will be used (Ref. 16). The stationary phase point for the microsphere is located at $r_{\pm} = (r_{\pm}, \theta_{\pm}, \phi_{\pm})$. The coordinates

$$r_{\pm} = |x-x'|/\sin\theta_{\pm} \quad (40a)$$

$$\phi_{\pm} = 0 \quad (40b)$$

$$\cos\theta_{\pm} = \pm k_2 \cos\theta_2 / k_{\pm} \quad (40c)$$

and θ_{\pm} are the coherent angles at ω_{\pm} . An examination of Equation 39 reveals that there is always a stationary phase point for the sum-frequency (ω_+) wave or the difference-frequency (ω_-) wave, if $k_{\pm} > k_2 \cos\theta_2$. Thereby it restricts the range of angles in which the second laser can be aligned for coherent sum or difference frequency wave generation.

The last integral over the x' -coordinate in Equation 39b is over a finite region and will give rise to the phase-matching term. Then, the coherent field in Equation 38 is given by

$$E_c^{(2)}(r, \omega_{\pm}) = \hat{r}_{\pm} f L j_0(\Delta_{\pm} L/2) f_{\pm}^{(2)}(\theta_2 | \theta_{\pm}, 0) \left[\frac{2\pi i}{k_{\pm} \sin\theta_{\pm}} \right] \exp[i\Delta_{\pm} L/2 + i\phi_{\pm}(r)] \quad (41)$$

where the unit polarization vector of the coherent electric field at point r far outside the slab is $\hat{r}_{\pm} = \hat{x} \cos\theta_{\pm} - \hat{z} \sin\theta_{\pm}$, $j_0(z) = \sin z/z$ is the usual phase-matching term and $f = N 4\pi a^3/3$ is the volume fraction of microspheres. In Equation 41, the scattering amplitude per unit volume is evaluated at the stationary phase point and is given by

$$f_{\pm}^{(2)}(\theta_2|\theta_{\pm},0) = i\frac{3}{2}er_{\pm}k_{\pm}^3a^2[\cos\theta_2\cos2\theta_{\pm}U_{21}^{\pm} + 2/3\sin\theta_2\sin2\theta_{\pm}U_{20}^{\pm}]/(3\epsilon_h(\omega_{\pm})+2\epsilon_b) \quad (42)$$

while the phase of the wave $\phi_{\pm}(\mathbf{r})$ is

$$\phi_{\pm}(\mathbf{r}) = k_{\pm}[\sin\theta_{\pm}x + \cos\theta_{\pm}z] \quad (43)$$

The phase factor $\Delta_{\pm}L/2$ arises from phase mismatch between the polarization driven by incident waves and nonlinear wave, which is given by

$$\Delta_{\pm} = k_1 \pm k_2\sin\theta_2 - k_{\pm}\sin\theta_{\pm} \quad (44)$$

An examination of the scattering amplitude evaluated at the stationary phase point reveals that there is no coherent response if the lasers are collinear and copolarized, that is, $\theta_2 = \pi/2 = \theta_{\pm}$.

3.2.2.2 Total Intensity: Second-Order Scattering. The total intensity for the sum and difference frequency generation from a slab of microparticle composite of thickness L is given by

$$I^{(2)}(\mathbf{r},\omega_{\pm}) = N \int_{-\frac{1}{2}L}^{\frac{1}{2}L} dx' \int_{-\infty}^{\infty} dy' \int_{-\infty}^{\infty} dx'' I_S^{(2)}(\mathbf{r},\mathbf{r}',\omega_{\pm}) \quad (45)$$

where N is the microparticle number density and I_S is given in Equation 38. The total intensity can be decomposed into two parts, viz, the coherent and incoherent intensities. The coherent part is given by

$$I_C^{(2)}(r, \omega_{\pm}) = \frac{c}{8\pi} E_C^{(2)}(r, \omega_{\pm}) \times B_C^{(2)}(r, \omega_{\pm}) \cdot \hat{r} \quad (46a)$$

$$= f^2 L^2 \frac{9\pi c}{8} \frac{|k_{\pm}|^4 a^4 e^2 |r_{\pm}|^2}{|3\epsilon_h(\omega_{\pm}) + 2\epsilon_b|^2} i_{\pm}^{(2)}(\theta_2) |j_0(\Delta_{\pm} L/2)|^2 \quad (46b)$$

where

$$i_{\pm}^{(2)}(\theta_2) = |\cos\theta_2 \cos 2\theta_{\pm} U_{21}^{\pm} + 2/3 \sin\theta_2 \sin 2\theta_{\pm} U_{20}^{\pm}|^2 \quad (46c)$$

$B_C^{(2)} = \hat{r} \times E_C^{(2)}$ and $E_C^{(2)}$ is given in Equation 41. The incoherent part is given by

$$I_i^{(2)}(r, \omega_{\pm}) = \frac{c}{8\pi} N \int_{-\frac{1}{2}L}^{\frac{1}{2}L} dx' \int_{-\infty}^{\infty} dy' \int_{-\infty}^{\infty} dz' \frac{|f_{\pm}^{(2)}(\theta', \phi')|^2}{|r - r'|^2} \quad (47a)$$

where the x', y' , and z' integrations can be easily evaluated, and the incoherent intensity is given by

$$I_i^{(2)}(r, \omega_{\pm}) = fL \frac{3\pi^2 c}{16} \frac{|k_{\pm}|^6 a^7 e^2 |r_{\pm}|^2}{|3\epsilon_h(\omega_{\pm}) + 2\epsilon_b|^2} i_{\pm}^{(2)}(\theta_2) \quad (47b)$$

where

$$i_{\pm}(\theta_2) = \cos^2 \theta_2 U_{21}^{\pm 2} + 8/9 \sin^2 \theta_2 U_{20}^{\pm 2} \quad (47c)$$

3.2.3 Numerical Results and Discussion

The microparticles to be considered in the numerical calculation are silver spheres with radius $a > 20 \text{ \AA}$, where the quantum size effect is not important (Ref. 14). All the parameters for silver spheres are given in Section 3.1.3.

Figures 11 through 13 depict the second-order responses of the silver sphere for difference and sum frequency generation. To illustrate the surface enhanced nature, the frequency of the first incident laser light is always tuned to the surface dipole resonant frequency, viz., $\omega_1 = \omega_S$, in order to maximize the enhancement of the drive terms for the second-order fields. The frequency of the second laser light is tuned to the vicinity of ω_S , to optimize the second enhancement factor in the drive terms. Also, the second laser light may be tuned to the frequency $\omega_2 = \omega_S - \omega_Q$. The intensity of both incident light beams are 1 MW/cm^2 .

All the responses in Figures 11 through 13 for the small difference frequency and the sum frequency at the surface quadrupole resonance are well screened, since the frequencies are below the plasma frequency. And the responses in Figures 11 through 13 for the sum frequency generation near $2\omega_S$ are highly oscillatory.

For quadrupole ($\ell = 2$) responses, the total charge is zero and the acoustic condition can be imposed as an additional boundary condition (ABC). However, for monopole ($\ell = 0$) responses, one must ensure the charge conservation and the ABC is the charge neutrality instead of the acoustic condition. Thus, the acoustic condition may be violated, which implies an electron flow across the boundary of the sphere.

In Figure 13, the acoustic condition is indeed violated for $\ell = 0$. For the difference frequency generation shown in Figure 13(a), the radial velocity at the surface is nearly equal to the maximum velocity inside the sphere, where $v/\omega_- \sim 1$. For the sum frequency generation near $2\omega_S$ shown in Figure 13(c), the radial velocity at the surface is nearly zero, where $v/\omega_+ \sim 0.01$. Therefore, the ratio of the radial velocity at the surface to the maximum velocity inside the sphere is on the order of v/ω_{\pm} for $\ell = 0$. Also, the $\ell = 2$ second-order responses in Figures 11(e), 12(e), and 13(e) are indeed enhanced with respect to the $\ell = 0$ counterparts in Figures 11(b), 12(b), and 13(b).

(a) $\omega_1 = \omega_s$, $l = 0$, $m = 0$;
difference frequency genera-
tion with $\omega_- = 0.01 \omega_p$.

(b) $\omega_1 = \omega_s$, $l = 0$, $m = 0$;
for sum frequency generation
with $\omega_+ = \omega_q = 0.3642 \mu\text{m}$.

(c) $\omega_1 = \omega_s$, $l = 0$, $m = 0$;
for sum frequency generation
 $\omega_+ = 2\omega_s - 0.01 \omega_p = 0.1904 \mu\text{m}$.
The units r_+ for $n_{2,l,m}(r, \omega_{\pm})$
are $1.89 \times 10^{16} \text{ cm}^{-3}$.

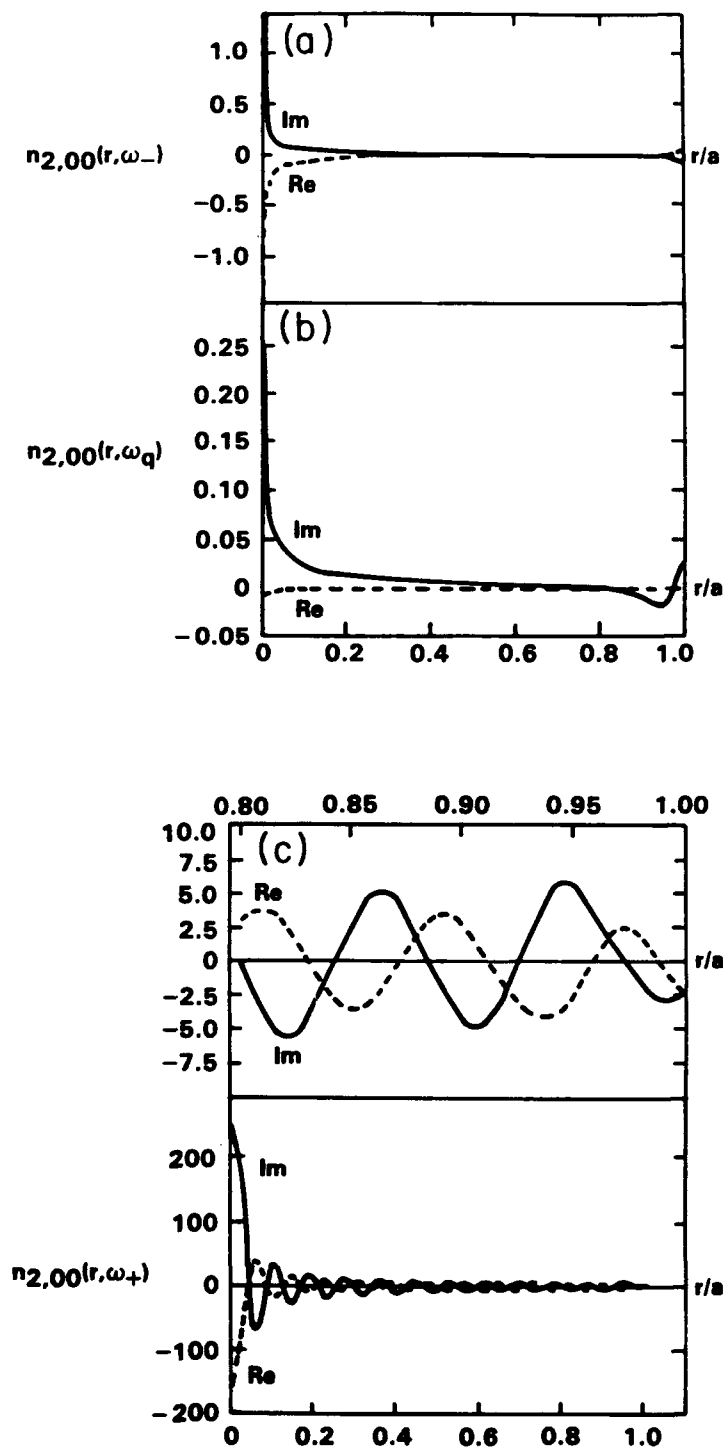
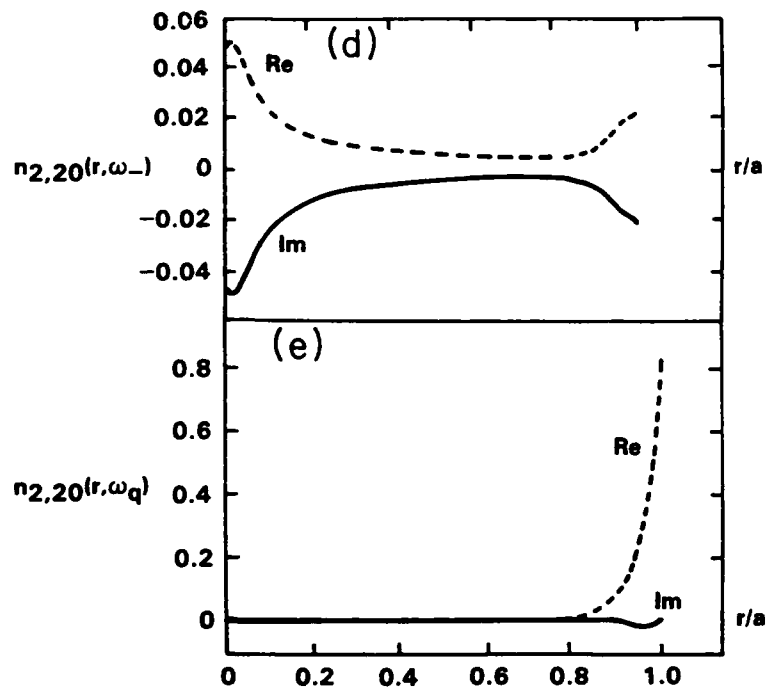


Figure 11. Second-order dimensionless electron density profile $n_{2,l,m}(r, \omega_{\pm})$ versus r/a , $a = 100 \text{ \AA}$.

(d) $l = 2, m = 0$; for
difference frequency
generation with
 $\omega_- = 0.01 \omega_p$.



(f) $l = 2, m = 0$; for sum
frequency generation
 $\omega_+ = 2\omega_s - 0.01 \omega_p =$
 $0.1904 \mu\text{m}$. The units r_{\pm}
for $n_{2,20}(r, \omega_{\pm})$ are
 $1.89 \times 10^{18} \text{ cm}^{-3}$.

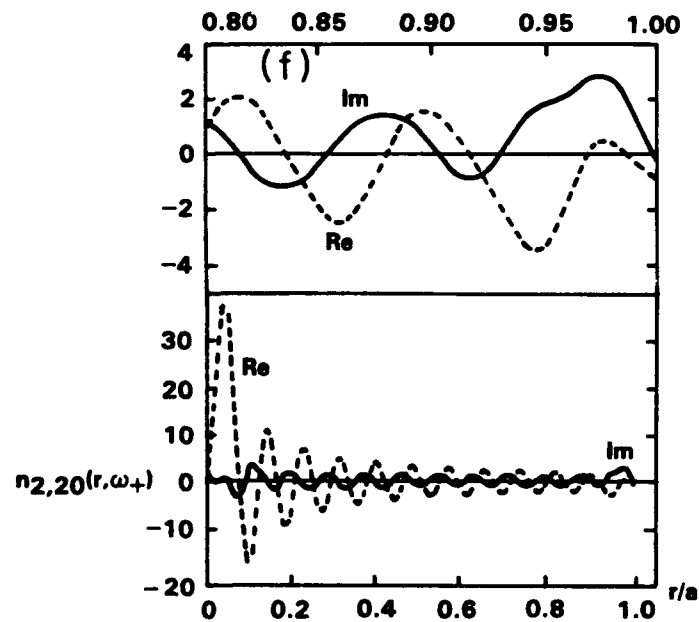


Figure 11. (Concluded)

Finally, the coherent and incoherent intensity for a slab of tenuous silver microsphere composite embedded in a dispersive host will be calculated. The configuration is shown in Figure 1. The dispersive host is chosen to be an artificial glass. The first incident frequency ω_1 is chosen to be the surface dipole frequency ω_s of a silver sphere in the glass host, viz., $\omega_1 = \omega_s = 0.4304 \mu\text{m}$ with $\epsilon_h(\omega_s) = 2.15$. The second incident frequency ω_2 is either tuned to the vicinity of ω_s , viz., $\omega_2 = \omega_s - 0.05\omega_p = 0.4608 \mu\text{m}$ with $\epsilon_h(\omega_2) = 2.14$. Or the frequency ω_2 may be the difference frequency between the surface dipole and quadrupole resonances, viz., $\omega_2 = \omega_q - \omega_s$, with $\omega_q \approx 0.4 \mu\text{m}$ and $\epsilon_h(\omega_2) = 1.9$.

(a) $\ell = 0, m = 0; \omega_- = 0.01 \omega_p$.

(b) $\ell = 0; \omega_+ = \omega_q$.

(c) $\ell = 0, m = 0; \omega_+ = 2\omega_s - 0.01 \omega_p$.

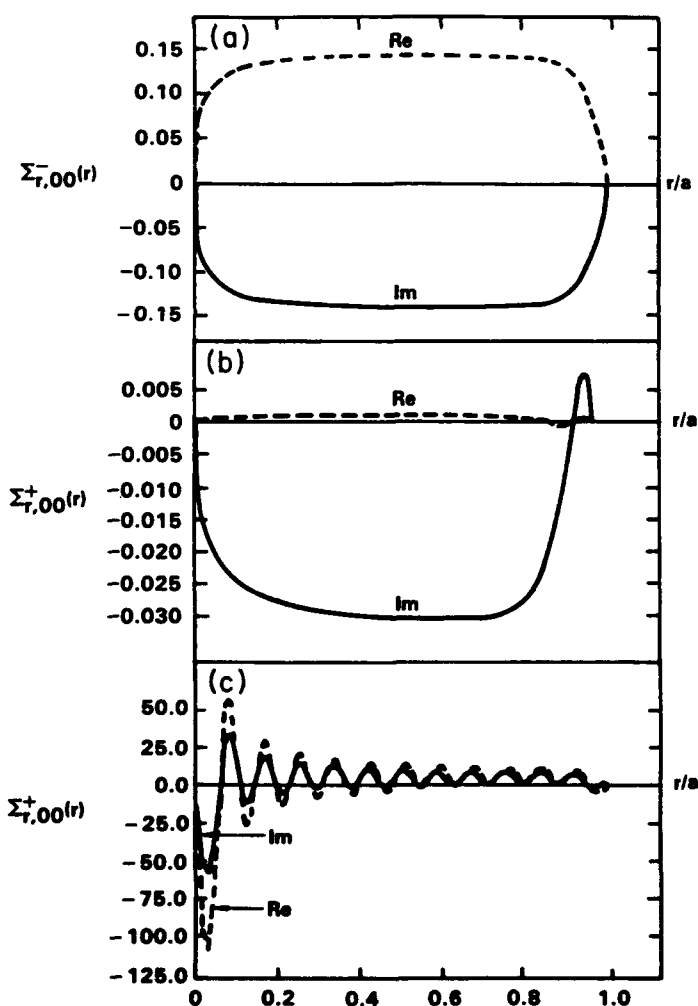


Figure 12. Second-order dimensionless radial electric field $\Sigma_{r,\ell m}^{\pm}(r)$ versus r/a , $a \approx 100 \text{ \AA}$. Same configuration treated in Figure 2. The units E_{20} for $\Sigma_{r,\ell m}^{\pm}(r)$ are 2.3 stat V/cm.

(d) $\ell = 2, m = 0; \omega_- = 0.01 \omega_p$.

(e) $\ell = 2, m = 0; \omega_+ = \omega_q$.

(f) $\ell = 2, m = 0; \omega_+ = 2\omega_S - 0.01 \omega_p$.

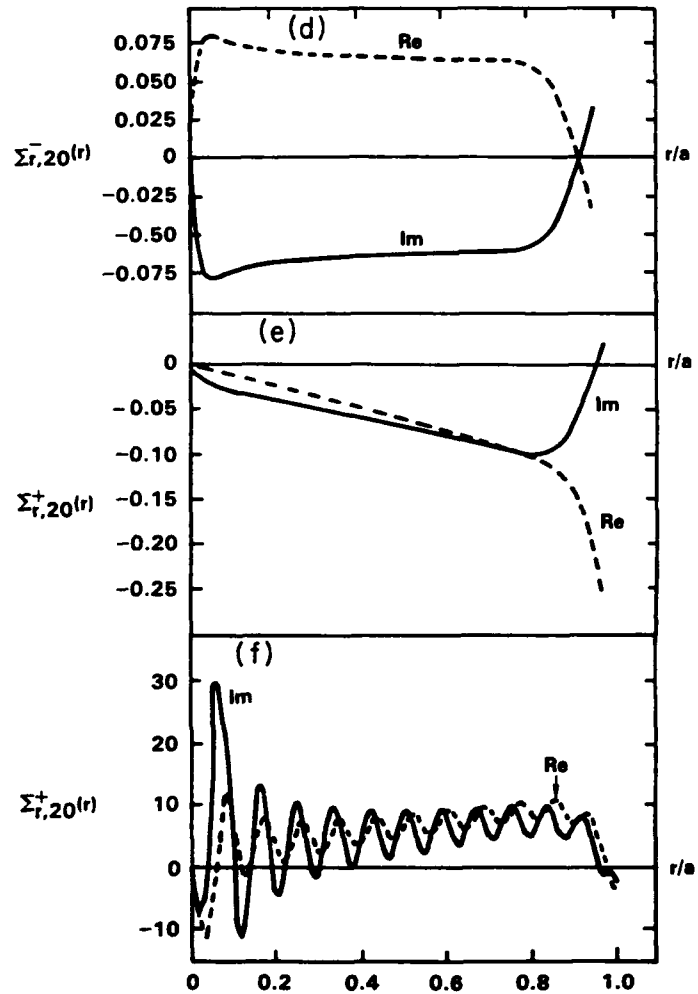


Figure 12. (Concluded)

The coherent intensity I_c of the sum (ω_+) or difference (ω_-) frequency generation peaks strongly near the perfect phase matching, viz., $\Delta_{\pm} L \leq 1$, where Δ_{\pm} is defined in Equation 44 and L is the slab thickness. The phase mismatch Δ_{\pm} defines a coherent length $L_{coh} = 1/\Delta_{\pm}$. Only for $L < L_{coh}$, the coherent intensity is significant and increases more or less quadratically with L . For a few millimeters thick silver microsphere composite, the sufficiently long coherent length L_{coh} is only achievable under the perfect phase matching, viz., $\Delta_{\pm} = 0$.

In order to have perfect phase matching, the host dielectric constant ϵ_h at the sum (difference) frequency must be less (greater) than $\epsilon_h(\omega_1)$ and $\epsilon_h(\omega_2)$. The incident angle θ_2 is determined by $\epsilon_h(\omega_{\pm})$ via the perfect phase matching condition. The angle θ_2

will then set the coherent angle θ_{\pm} through the stationary condition given in Equation 40c. It is no loss of generality to restrict the values of θ_2 to the range between 0° and 90° , since the range $90^\circ \leq \theta_2 \leq 180^\circ$ is just the mirror image of the former range with respect to the x-y plane. The physical values of θ_2 are going to limit the possible choices of the host materials, viz., $\epsilon_h(\omega_{\pm})$. A slab of silver microsphere composite to be considered consists of radius $a = 100 \text{ \AA}$, thickness $L = 1 \text{ mm}$ and volume fraction $f = 10^{-4}$. Figure 14 shows the dependence of the incident and coherent angles on $\epsilon_h(\omega_{\pm})$. For the sum frequency generation near $2\omega_s$ or at ω_q , the possible choices of $\epsilon_h(\omega_{\pm})$ are respectively in the range of (1.08, 2.14) or (1.8, 2.13). The difference frequency generation at $\omega_- = 0.05 \omega_p$ requires that $2.3 \leq \epsilon_h(\omega_-) < 900$.

Figure 15 shows the dependence of the coherent and incoherent intensities upon $\epsilon_h(\omega_{\pm})$. The reduced coherent and incoherent intensities are $i_c^{\pm}(\theta_2)/|U_{20}^{\pm}|^2$ and $i^{\pm}(\theta_2)/|U_{20}^{\pm}|^2$, respectively. The conversion factor to the corresponding absolute intensity is given in the figure caption for each case. The coherent intensity of the sum frequency generation near $2\omega_s$ is about 1 W/cm^2 , which is 10 dB above the corresponding incoherent intensity for $1.2 \leq \epsilon_h(\omega_{\pm}) \leq 2.1$. The coherent intensity of the sum frequency generation at ω_q is $0.05\text{--}0.2 \text{ W/cm}^2$, which is 27 to 30 dB above the incoherent intensity for $1.75 \leq \epsilon_h(\omega_q) \leq 2.1$. The coherent intensity at the difference frequency at $\omega_- = 0.05 \omega_p$ is only $1\text{--}10 \text{ \mu W/cm}^2$, which is 40 to 50 dB above the incoherent counterpart for $\epsilon_h(\omega_-) \geq 2.4$. For the sum frequency generation, the incoherent intensity may still be detectable. However, for the difference frequency generation, only the coherent intensity can be observed with ease.

In Figures 16(a) and 16(b), the size-dependence of the dimensionless function U_{20}^{\pm} in the quadrupole moments for dc rectified (U_{20}^-) and second-harmonic (U_{20}^+) generation for the case of a single intense laser irradiated on a silver microsphere composite are shown. Both figures show increasing quadrupole moments for decreasing particle sizes and vanishing quadrupole moments for extremely small spheres. These are the similar size-dependent characteristics shown in Figure 5 for the linear dielectric functions. However, the quasi-hydrodynamic theory adopted here breaks down for extremely small particles, where the quantum effect is important and should be included with care.

3.3 THIRD-ORDER SUSCEPTIBILITY IN THE FREQUENCY DOMAIN

For the third-order susceptibility, both the self-action effect of the laser fields and the cross-action effect between the laser fields at the degenerate and nondegenerate frequencies will be considered.

The self-action, which is described in terms of the intensity-dependent nonlinear dielectric function, is responsible for the self-phase modulation and self-focusing of a given laser field. They are important effects for a single laser field as well

(a) $l = 0, m = 0$;
 $\omega_- = 0.01 \omega_p$ (unit
 $V_{20} = 6.4 \times 10^3$ cm/sec).

(b) $l = 0, m = 0$;
 $\omega_+ = \omega_q$ (unit
 $V_{20} = 3.5 \times 10^3$ cm/sec).

(c) $l = 0, m = 0$;
 $\omega_+ = 2\omega_S - 0.01 \omega_p$
(unit $V_{20} = 1.7 \times 10^4$ cm/sec).

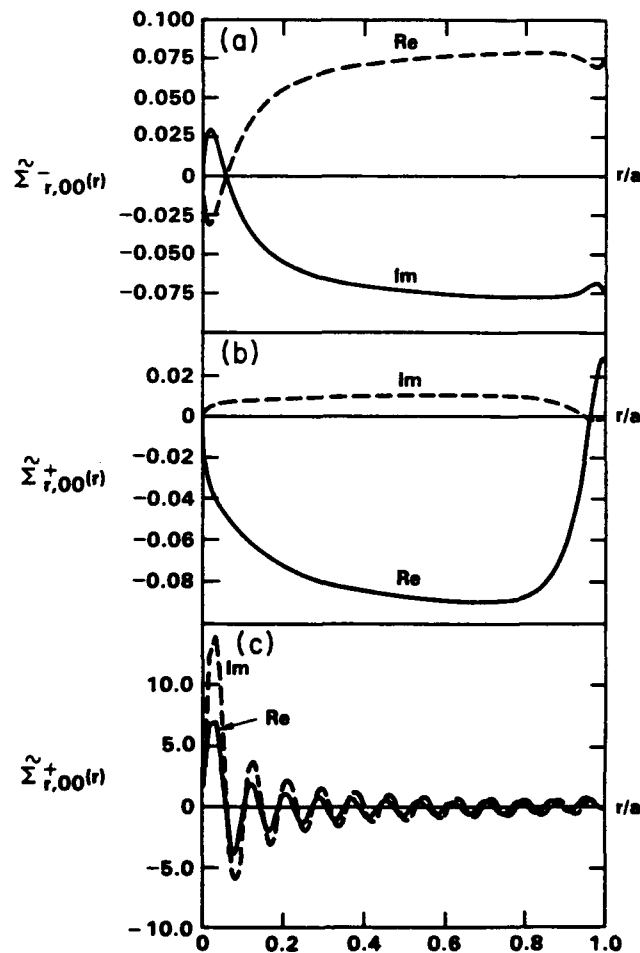


Figure 13. Second-order dimensionless radial velocity $\tilde{\Sigma}_{r,lm}^{\pm}(r)$ versus r/a , $a = 100 \text{ \AA}$. Same configuration treated in Figure 2.

(d) $l = 2, m = 0$;
 $\omega_- = 0.01 \omega_p$ (unit
 $V_{20} = 6.4 \times 10^3$ cm/sec).

(e) $l = 2, m = 0$;
 $\omega_+ = \omega_q$ (unit
 $V_{20} = 3.5 \times 10^3$ cm/sec).

(f) $l = 2, m = 0$;
 $\omega_+ = 2\omega_S - 0.01 \omega_p$
(unit $V_{20} = 1.7 \times 10^4$ cm/sec).

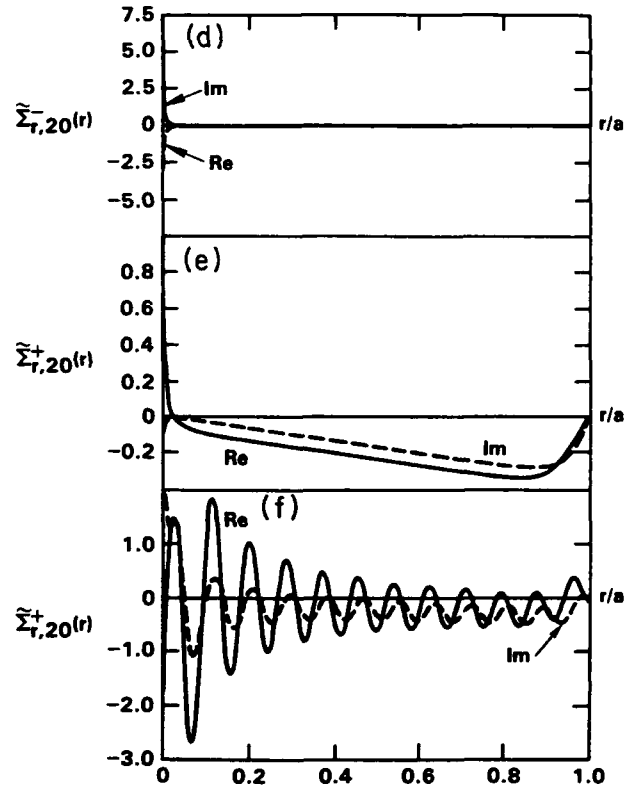
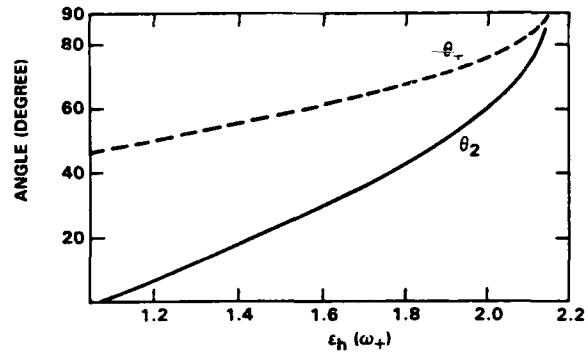


Figure 13. (Concluded)

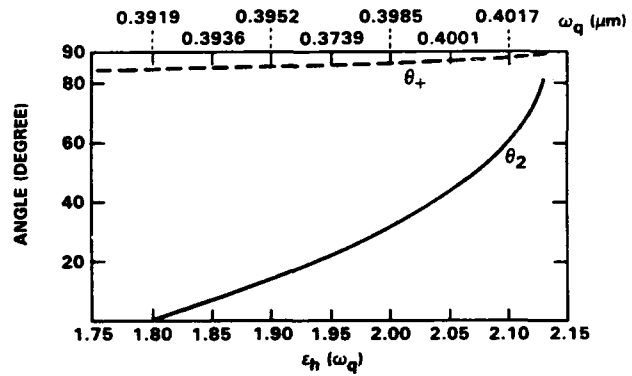
as for phase conjugation and coherent two-wave mixing. The cross-effect is described by the cross-intensity-dependent nonlinear dielectric function and coherent coupling coefficient which are responsible for the cross-phase modulation and coherent coupling between the laser fields. They are important effects in the phase conjugation and coherent two-wave mixing. In particular, the coherent coupling coefficient is the main mechanism in the coherent two-wave mixing.

The electrodynamic problem has been treated globally, calculating the dipole moment induced upon the sphere by the applied field, and thus obtaining directly the surface-plasma resonance within the quasi-hydrodynamic formalism. Therefore, if the incident frequency is near the surface plasma resonant frequency of the microparticles, there will be local field enhancement of the third-order susceptibility just as the theory states.

(a) $\omega_+ = 2\omega_s - 0.05 \omega_p = 0.2225 \mu\text{m}.$



(b) $\omega_q = 0.39 - 0.41 \mu\text{m}.$



(c) $\omega = 0.05 \omega_p = 6.54 \mu\text{m}.$
 $f = 10^{-4}$, $L = 1 \text{ mm}$, and $a = 100 \text{ \AA}.$

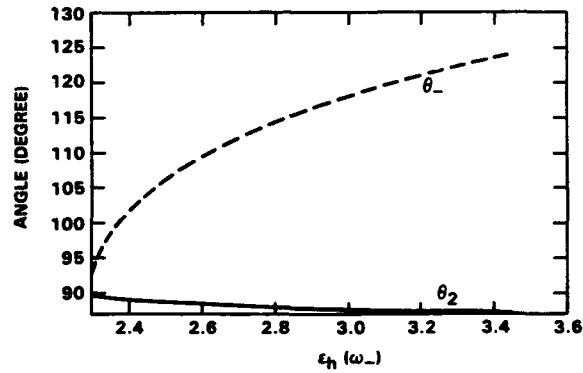
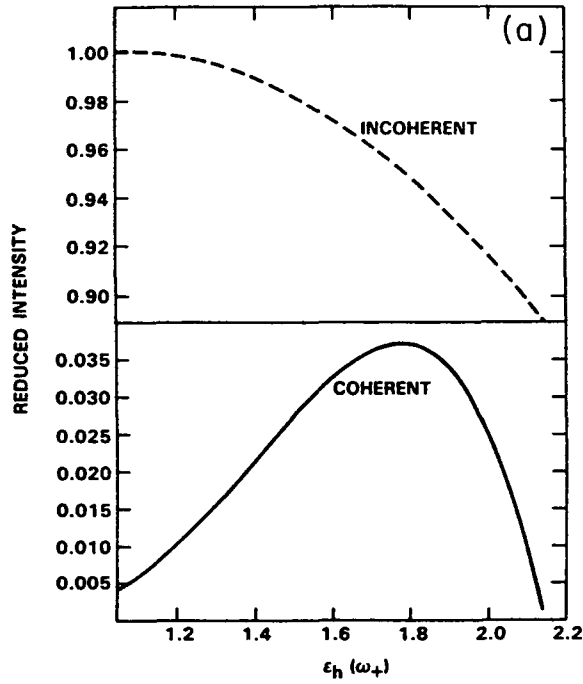


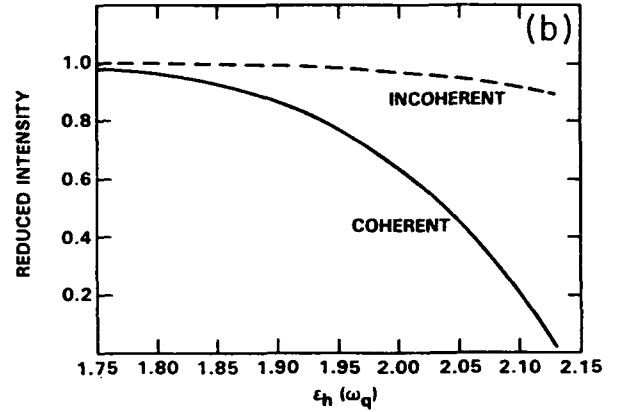
Figure 14. The incident θ_2 and coherent θ_{\pm} angles versus $\epsilon_h(\omega_{\pm})$.

3.3.1 Third-Order Susceptibility in the Frequency Domain

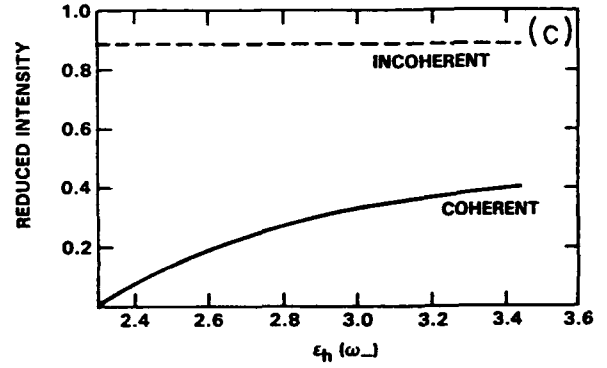
3.3.1.1 Self-Action and Cross Action Effects. For self-action, consider a metallic sphere composite, which is irradiated by an intense laser beam of frequency ω_i , amplitude A_i , propagating along the x-axis and polarized in the z-direction. The equation, which governs the induced third-order density fluctuation at $\omega_i(r, \omega_i)$ is Equation 12.



(a) $\omega_+ = 2\omega_s - 0.05\omega_p$. The conversion factors are 29.19 W/cm^2 and 0.12 W/cm^2 for coherent and incoherent intensities.



(b) $\omega_+ = \omega_q$, the conversion factors are 0.23 W/cm^2 and 0.30 mW/cm^2 for coherent and incoherent intensities.



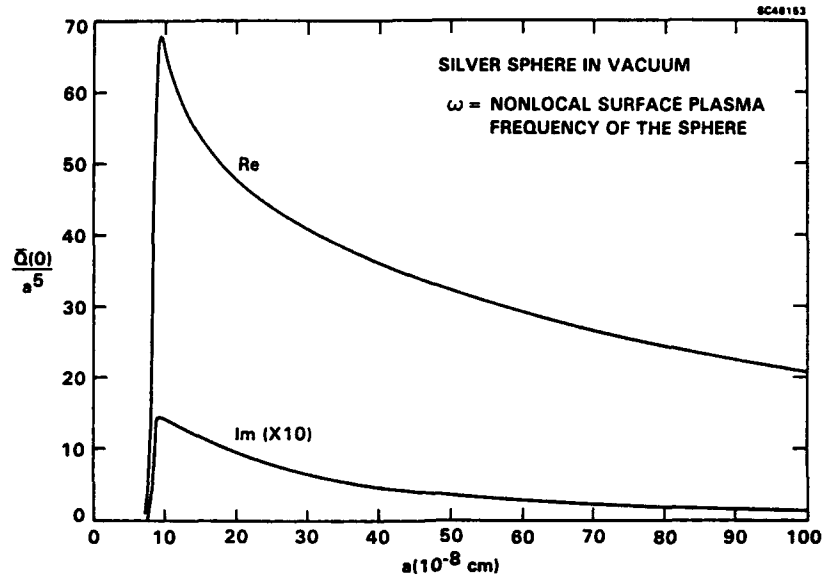
(c) $\omega_- = 0.05\omega_q$, the conversion factors are $13.76 \mu\text{W/cm}^2$ and 6.65 nW/cm^2 for the coherent and incoherent intensity. $f = 10^{-4}$, $L = 1 \text{ mm}$, and $a = 100 \text{ \AA}$.

Figure 15. The reduced coherent and incoherent intensities versus $\epsilon_h(\omega_{\pm})$.

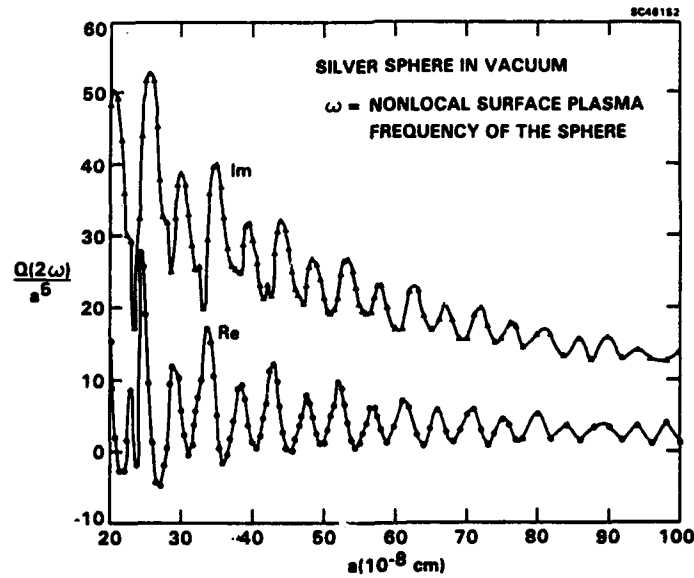
The induced third-order fields are given as follows. Inside the sphere, the density and electrostatic potential are given by

$$n_3(r, \omega_1) = n_{3,10}(r, \omega_1) Y_{10}(\theta) + n_{3,30}(r, \omega_1) Y_{30}(\theta) \quad (48)$$

$$\phi_3(r, \omega_1) = \phi_{3,10}(r, \omega_1) Y_{10}(\theta) + \phi_{3,30}(r, \omega_1) Y_{30}(\theta) \quad (49)$$

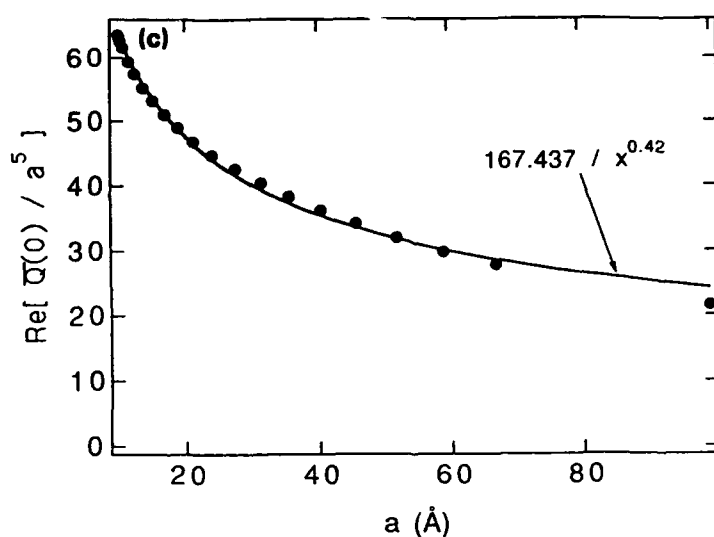


(a) For dc rectified part, $U_{20}^- = \bar{Q}(0)/a^5$.

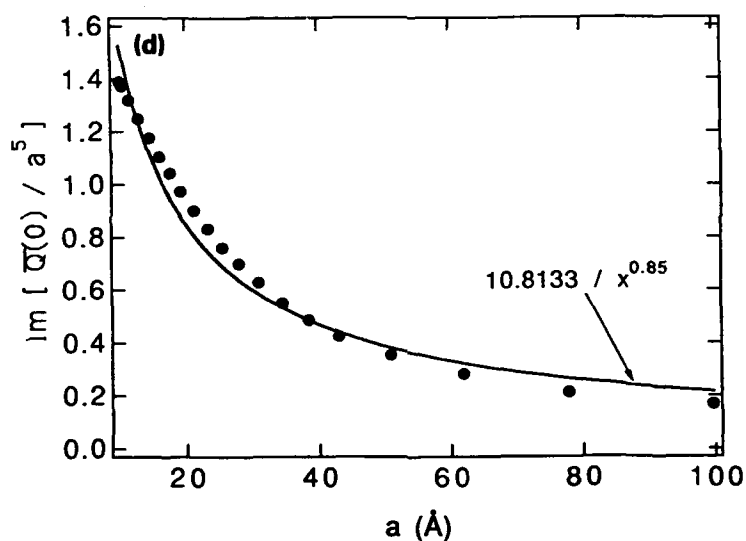


(b) For second-harmonic part, $U_{20}^+ = \bar{Q}(2\omega)/a^5$.

Figure 16. The dimensionless function U_{20}^\pm versus particle sizes.



(c) The best fitted power law curve for (a).



(d) The best fitted power law curve for (b)

Figure 16. (Concluded)

Outside the sphere, the electrostatic potential is given by

$$\phi_3(r, \omega_1) = \frac{u^{(3)}(\omega_1)}{r^2} \cos\theta + \frac{o(\omega_1)}{r^4} Y_{30}(\theta) \quad (50)$$

where $u^{(3)}(\omega_1)$ and $o(\omega_1)$ are the induced third-order dipole and octupole moments of the sphere. The induced third-order dipole moment is given in Appendix C (Equation C.10).

The third-order octupole moment ($l = 3$) is much smaller compared to the third-order dipole moment ($l = 1$) for spheres in the Rayleigh limit. Thus, the third-order octupole moment contribution to the third-order susceptibility is negligible.

For a very dilute metallic sphere composite slab, the third-order coherent field at point r outside the slab generated by microparticle third-order polarization at ω_i is given by

$$E_C^{(3)}(r, \omega_i) = fL2\pi i k_i \{-\hat{\theta} \sin \theta P_0^{(3)}(\omega_i)\} \quad (51)$$

where f is the volume, L is the thickness of the slab, and $P_m^{(3)}(\omega_i)$ is given in Appendix C (Equation C.11).

The corresponding third-order susceptibility of the composite is given by

$$\chi_{zzzz}^{(3)}(\omega_i; \omega_i, \omega_i, -\omega_i) = \chi_0^{(3)} \epsilon_h(\omega_i) f P_{i,1m}^{(3)}(\omega_i) \frac{1}{D_1(\omega_i) |D_1(\omega_i)|^2} \quad (52)$$

where the dimensionless function $P_{i,1m}(\omega_i)$ is given in Appendix C (Equation C.10), and the local field enhancement factors are clearly given.

For a silver sphere of 100 Å in radius embedded in a host with $\epsilon_h = 1$, one has

$$\chi_0^{(3)} = 3.59 \times 10^{-10} \quad (53)$$

After lengthy numerical integration, one obtains at the surface plasma frequency ω_s

$$\chi^{(3)}(\omega_s) = (-5.3 + 1.81i) \times 10^{-9} \text{ esu/sphere} \quad (54a)$$

for $v = 0.02 \omega_p$, and

$$\chi^{(3)}(\omega_s) = (-8.3 + i 4.1) \times 10^{-12} \text{ esu/sphere} \quad (54b)$$

for $v = 0.1 \omega_p$, respectively. The experimental value (Ref. 18) for single silver sphere is 2.4×10^{-9} esu, which was measured in the degenerate four-wave mixing configuration, and is fairly close to the value given in Equation 54a.

The degenerate third-order susceptibility for a very dilute silver sphere composite with volume fraction f is given by $f \chi^{(3)}(\omega_s)$, where the numerical values of $\chi^{(3)}(\omega_s)$ are given by Equations 54.

For cross-action effects, consider the metallic microsphere composite, which is irradiated by two intense laser beams of frequencies ω_1 and ω_2 , electric field amplitudes A_1 and A_2 , both propagating along the x -axis and linearly polarized in the z -direction. Then the third-order susceptibility under this configuration is given by

$$\chi_{zzzz}^{(3)}(\omega_i; \omega_i, \omega_j, -\omega_j) = \epsilon_h(\omega_i) f \chi_0^{(3)} \sum_{j=1}^2 P_{j,10}^{(3)}(\omega_i) \frac{1}{D_1(\omega_i) |D_1(\omega_j)|^2} \quad (55)$$

where the $i = j$ term is the self-action contribution as given by Equation 52 and the $i \neq j$ term is the cross-action contribution.

According to the classification discussed in Section 2.3, the third-order susceptibility in Equation 55 for $i = 1$ can be cast into the following groups,

$$\begin{aligned} \chi_{zzzz}^{(3)}(\omega_1) &= \chi_{zzzz}^{(3C)}(\omega_1; \omega_1, \omega_2, -\omega_2) + \chi_{zzzz}^{(3X)}(\omega_1; \omega_1, \omega_2, -\omega_2) \\ &\quad + \chi_{zzzz}^{(3S)}(\omega_1; \omega_1, \omega_1, -\omega_1) \end{aligned} \quad (56)$$

which are the coherent coupling, cross-phase-modulation and self-phase modulation parts of the susceptibility, respectively.

In Equation 56, the coherent coupling part is given by

$$\chi_{zzzz}^{(3C)}(\omega_1; \omega_1, \omega_2, -\omega_2) = \chi_{zzzz}^{(3)}(\omega_1; \omega_2 + \omega_-) + \chi_{zzzz}^{(3)}(\omega_1; -\omega_2 + \omega_+) \quad (57a)$$

which comes from the cascading sum and difference frequency effects.

In Equation 56, the cross-phase modulation part is given by

$$\chi_{zzzz}^{(3X)}(\omega_1; \omega_1, \omega_2, -\omega_2) = \chi_{zzzz}^{(3)}(\omega_1; \omega_1 + (\omega_2 - \omega_2)) + \chi_{zzzz}^{(3)}(\omega_1; \omega_1, \omega_2, -\omega_2) \quad (57b)$$

which comes from the cascading cross-rectified effect and direct third-order contribution.

In Equation 56, the self-phase modulation part is given by

$$\begin{aligned} \chi_{zzzz}^{(3S)}(\omega_1; \omega_1, \omega_1, -\omega_1) &= \chi_{zzzz}^{(3)}(\omega_1; \omega_1 + (\omega_1 - \omega_1)) + \chi_{zzzz}^{(3)}(\omega_1; -\omega_1 + 2\omega_1) \\ &+ \chi_{zzzz}^{(3)}(\omega_1; \omega_1, \omega_1, -\omega_1) \end{aligned} \quad (57c)$$

which comes from the cascading self-rectified and self-second-harmonic effect and the direct third-order contribution.

3.3.1.2 Polarization Effect. For polarization effect, consider the more general situation discussed in Section 2.0 (Fig. 1). There are an elliptically polarized ω_1 wave with polarization vector $\hat{e}_1 = \hat{y} + n\hat{z}$ and a linearly polarized ω_2 wave with polarization vector $\hat{e}_2 = \hat{z}$ incident normal to the microparticle composite, i.e., $\theta_2 = \pi/2$. The normal direction of the composite or the propagation direction of both waves is in the x-direction.

For a very dilute metallic sphere composite slab, the third-order coherent field at point r outside the slab generated by microparticle third-order polarization at ω_i is given by

$$E_C^{(3)}(r, \omega_1) = fL2\pi k_1 \{-\hat{\theta}\eta \sin\theta P_0^{(3)}(\omega_1) + (\hat{\theta}\cos\theta \sin\phi - \hat{\phi}\cos\phi)P_1^{(3)}(\omega_1)\} \quad (58a)$$

$$E_C^{(3)}(r, \omega_2) = fL2\pi k_2 \{-\hat{\theta}\sin\theta P_0^{(3)}(\omega_2)\} \quad (58b)$$

where f is the volume, L is the thickness of the slab, and $P_m^{(3)}(\omega_i)$ is given in Appendix C (by Equation C.11).

Then the nonvanishing components of the third-order susceptibility are given by

$$\chi_{zzzz}(\omega_i; \omega_i, \omega_i, -\omega_i) = \epsilon_h(\omega_i) f \chi_0^{(3)} P_{i,10}^{(3)}(\omega_i) \frac{1}{D_1(\omega_i) |D_1(\omega_i)|^2} \quad (59a)$$

for self-action contribution and

$$\begin{aligned} \chi_{zzzz}(\omega_i; \omega_i, \omega_j, -\omega_j) + \chi_{zyzy}(\omega_i; \omega_i, \omega_j, -\omega_j) &= \epsilon_h(\omega_i) f \chi_0^{(3)} P_{j,10}^{(3)}(\omega_i) \\ &\times \frac{1}{D_1(\omega_i) |D_1(\omega_j)|^2} \end{aligned} \quad (59b)$$

$$\chi_{yzzy}(\omega_i; \omega_i, \omega_j, -\omega_j) = \epsilon_h(\omega_i) f \chi_0^{(3)} P_{j,11}^{(3)}(\omega_i) \frac{1}{D_1(\omega_i) |D_1(\omega_j)|^2} \quad (59c)$$

with $j \neq i$ for cross-action contribution, and $i = 1$ or 2 .

The third-order susceptibility in Equation 58 can also be grouped into the coherent coupling, cross-phase-modulation and self-phase modulation parts as was done for Equation 55.

3.3.2 Time-Dependence of Third-Order Susceptibility and Polarization

In Section 3.3.1, the third-order susceptibility of metallic microsphere composites in the frequency domain, which is convenient to use in the case of monochromatic or quasi-monochromatic light beams was calculated. However, in the case of ultrashort light pulses, the third-order susceptibility in the time domain will be more useful.

The more general time-dependent third-order nonlinear polarization is given by

$$P^{(3)}(t) = \int_0^\infty dt_1 \int_0^\infty dt_2 \int_0^\infty dt_3 \tilde{\chi}^{(3)}(t_1, t_2, t_3) E(t-t_1) E(t-t_2) E(t-t_3) \quad (60)$$

According to Equation 60 the time-dependent third-order susceptibility for metallic microsphere composites can be obtained from the Fourier transform of the frequency-dependent third-order susceptibility in Section 3.3.1 and is given by

$$\tilde{\chi}^{(3)}(t_1, t_2, t_3) = \int \frac{d\omega_1'}{2\pi} \int \frac{d\omega_2'}{2\pi} \int \frac{d\omega_3'}{2\pi} \tilde{\chi}^{(3)}(\omega; \omega_1', \omega_2', \omega_3') e^{-i(\omega_1' t_1 + \omega_2' t_2 + \omega_3' t_3)} \quad (61)$$

where

$$\omega = \omega_1' + \omega_2' + \omega_3'.$$

In Section 2.3, the different classification of the third-order responses was discussed. Here only the time-dependent third-order polarization for coherent coupling terms is worked out explicitly. If the metallic microsphere composite is irradiated by the two Gaussian light pulses at carrier frequencies ω_1 and ω_2 with pulse full widths T_1 and T_2 , and probe delay time τ_D , the time-dependent third-order susceptibility for the metallic microsphere composite can be obtained from Fourier transformation of Equations 59.

For a linearly polarized probe wave at ω_2 , the coherent coupling parts of the time-dependent third-order susceptibility are given by

$$\begin{aligned}
x_{zzzz}^{(3C)}(t_1, t_2, t_1) + x_{zyzy}^{(3C)}(t_1, t_2, t_1) = \epsilon_h(\omega_2) f x_0^{(3)} \left\{ \frac{p_{1,10}^{(3)}(\omega_2) t_2}{d_1(\omega_s)} \right. \\
\left. + i p_{1,10}^{(3)}(\omega_2) \right\} \times \frac{\theta(t_2)}{2v_s d_1(\omega_s)^3} e^{v_s t_2}
\end{aligned} \tag{62a}$$

$$\begin{aligned}
x_{yzyz}^{(3C)}(t_1, t_2, t_1) = \epsilon_h(\omega_2) f x_0^{(3)} \left\{ \frac{p_{1,11}^{(3)}(\omega_2) t_2}{d_1(\omega_s)} + p_{1,11}^{(3)}(\omega_2) \right\} \\
\times \frac{\theta(t_2)}{2v_s d_1(\omega_s)^3} e^{v_s t_2}
\end{aligned} \tag{62b}$$

where $\theta(t_2)$ is a step function, the denominator is given by

$$d_1(\omega_s) = \text{Re} \{D_1'(\omega_s)\} \tag{63a}$$

the inverse of intrinsic decay time is given by

$$v_s = \frac{\text{Im} D_1(\omega_s)}{d_1(\omega_s)} \tag{63b}$$

and t_1 and t_2 are, respectively, the time coordinate for the pump and probe waves. In Equation 61, the P-functions are given by

$$p_{1,1m}^{(3)}(\omega_2) = \bar{L}_{1m}(a, \omega_2) i_2(q_2 a) / a_2 i_2'(q_2 a) \tag{64a}$$

$$p_{1,1m}^{(3)}(\omega_2) = L_{1ms}(a, \omega_2) \tag{64b}$$

which are the same homogeneous and inhomogeneous factors shown in Appendix C (Equations C.10).

For simplicity, it is assumed that both pump (ω_1) and probe (ω_2) waves are propagating along the x-axis, i.e., $\theta_2 = \pi/2$. The envelopes of two pulses are chosen to be

$$A_i(x, t_i) = 2 \left[\frac{\sqrt{2\pi} I_i}{cT_i} \right]^{1/2} \exp \left[- \left(t_i - \frac{x}{v_i} \right)^2 / 4T_i^2 \right] \quad (65)$$

where I_i and v_i are the light intensity and phase velocity in the host medium, and T_i is the pulse full width, $i = 1$ or 2 .

Then the total electric field for the two-wave mixing can be written as

$$E(r, t) = \hat{e}_1 A_1(x, t) e^{-i\omega_1 t} + \hat{e}_2 A_2(x, t - \tau_D) e^{-i\omega_2(t - \tau_D)} + \text{c.c.} \quad (66)$$

where τ_D is the probe delay time.

Substituting Equations 62, 65 and 66 into Equation 60, the coherent parts of the time-dependent third-order polarization for the probe wave at ω_2 are given by

$$P_m^{(3c)}(t) = \epsilon_h(\omega_2) f x_0^{(3)} e^{-i\omega_2 t} \frac{4\sqrt{2\pi} I_1}{cT_1} \left[\frac{\sqrt{2\pi} I_2}{cT_2} \right]^{1/2} \\ \times \frac{1}{v_s v_e d_1(\omega_s)^3} O(t, \tau_D) \left\{ \frac{H(v_e T_e)}{d_1(\omega_s)} P'_{1,1m}^{(3)}(\omega_2) + i P(v_e T_e) P''_{1,1m}^{(3)}(\omega_2) \right\} \quad (67)$$

where the inverse of effective decay time for short pulses with relative delay is given by

$$v_e = v_s - \frac{\tau_D}{T_2^2} \quad (68a)$$

the overlap function is given by

$$O(t, \tau_D) = \exp \left[- \left(t - \tau_D - \frac{x}{v_2} \right)^2 / 2T_2^2 - \left(t - x/v_1 \right)^2 / 4T_1^2 \right] \quad (68b)$$

and the dimensionless polarization prefactors for the homogeneous and inhomogeneous contributions are given by

$$H(\nu_e T_e) = 2T_e^2 [1 - \nu_e P(\nu_e T_e)] \quad (68c)$$

$$P(\nu_e T_e) = \sqrt{\pi} T_e \exp(-\nu_e^2 T_e^2) \operatorname{erfc}(\nu_e T_e) \quad (68d)$$

with the effective pulse width T_e , which is defined by

$$\frac{1}{T_e^2} = \frac{1}{T_2^2} + \frac{2}{T_1^2} \quad (68e)$$

In Equation 66, the subscript $m = 1$ or 0 corresponds to the y - or z -component of the time-dependent third-order polarization of the probe wave at ω_2 .

3.4 SPECTRAL RANGE AND RESPONSE TIME

The spectral range of the nonlinear third-order susceptibility of the micro-particle composites is determined by the influential range of the local field enhancement factor. This can be easily determined by the FWHM of the enhancement factor. For silver microsphere composites from Figures 7 and 8, the spectral range is between $0.40 \mu\text{m}$ and $0.44 \mu\text{m}$. For gold microsphere composites, there is a smaller enhancement factor and larger spectral range because of gold's larger material intrinsic damping fitting parameter as compared to silver's.

The response times of the microparticle composite can be read out from their time-dependent polarization given in Equation 67. The response time is the effective decay time $(1/\nu_e)$ in the equation, which is determined by the intrinsic decay time $(1/\nu_s)$ of the microparticles as well as the ratio of the probe delay time (τ_D) to its pulse width (T_2) . The intrinsic decay times for the parameters used in Figures 3 through 10, are 20 fs and 5 fs for $\nu = 0.02 \omega_p$ and $\nu = 0.1 \omega_p$, respectively. These intrinsic decay times are typical of the electronic nonlinearity.

3.5 SATURATION CHARACTERISTICS

In a real material the optical nonlinearity cannot grow without limit and many materials will permit nonlinear changes only in a refractive index that saturates quite rapidly with power. Saturation often limits refractive index changes to an upper limit of 0.1 but apparently 0.001 is fairly common with a lower limit being typically 0.0001.

In this theory the nonlinear electrodynamics of microparticles is developed in terms of perturbation expansion. The saturation will set in if the expansion parameter is approaching unity.

From the calculated perturbed density, electric field or other fields, the expansion parameter can be easily extracted. Then, by equating the expansion parameter to unity, the saturation field and intensity for the nonlinear electrodynamics of the microparticles can be obtained.

Comparison of the perturbed density given in Appendices A, B and C (by Equations A.2, B.7 and C.6) shows that the following order of magnitude relationship exists between the second-order nonlinear density and the first-order linear density and the nonlinear density of successive orders

$$\frac{n_{n+1}}{n_n} = \frac{n_3}{n_2} = \frac{n_2}{n_1} = A_1/E_{\text{sat}} \quad (69)$$

where

$$E_{\text{sat}} = \frac{m\beta^2}{ea} D_1(\omega_i) = \frac{3eq_{\text{TF}}}{(q_{\text{TF}}r_s)^3 \epsilon_b a} D_1(\omega_i) \quad (70)$$

with A_1 and $D_1(\omega_i)$ are the electric field amplitude and the resonant denominator of the incident light. In Equation 70, r_s is a widely used measure of the electron density, and defined as the radius of a sphere whose volume is equal to the volume per free (or conduction) electron. Note that the saturation electric field given in Equation 70 is reduced by the surface plasma resonant effect, viz. $D_1(\omega_i)$, as well as the background

dielectric constant ϵ_D and is enhanced by the Thomas-Fermi screening effect, viz. the inverse of the Thomas-Fermi screening length q_{TF} .

The saturation fields for the parameters used in Figures 3 through 10, are 5.1 and 49.6 k statvolts per centimeter, which correspond to the saturation intensities, being 3.0 and 200 GW/cm^2 for silver spheres with $\nu = 0.02 \omega_p$ and $0.1 \omega_p$, respectively.

4.0 EXPERIMENTAL RESULTS

4.1 PHASE CONJUGATION EXPERIMENTS

4.1.1 Phase Conjugation in CS₂

4.1.1.1 Experimental Apparatus. Phase conjugation in CS₂ was studied experimentally utilizing the four wave mixing experimental system shown in Figure 17. A passively mode locked Nd:YAG oscillator produced a train of 8 to 10 pulses, with a pulse duration of 25 ps in a TEM₀₀ transverse mode. A single pulse was selected out of the pulse train and amplified through two single pass amplification stages. Between the two amplifiers, the beam was expanded by a factor of 3 by means of an inverted telescope, to increase the amplification and to reduce the divergence of the beam. The amplified pulse was frequency doubled to 532 nm, resulting in a single picosecond pulse with a maximum energy of 15 mJ, which corresponds to a peak power of ~ 600 MW. Vertical polarization of the frequency doubled pulses was ensured by a polarizing beam splitter. Beam splitter BS₁ (R = 0.15) was used to create the probe beam while beam splitter BS₂ (R = 0.50) reflects a small portion of the probe pulse into a reference pulse, I_r. The reference pulse is reflected back to BS₂ by mirror M₈, whose reflectivity was chosen to meet experimental requirements. The probe beam traverses the sample at an angle of 6° with the pump beam I_f. The temporal overlap was adjusted by the variable delay line consisting of mirrors M₃ through M₅. The backward pump beam I_b was created by retroreflection of I_f by mirror M₁ in close contact with the sample cell to ensure a maximum temporal overlap of the pulses within the nonlinear medium. The 0.55-mm thickness of the cell wall added to the retroreflection setup an inherent delay of 3 ps between the two pump pulses. This delay is much smaller than the pulse width and the experimentally determined coherence length of the pulses, which was 14 ps. In some experiments a special cell was used, the rear end of which was a mirror. This cell was, however, more difficult to handle and did not improve the maximum attainable phase-conjugate reflectivity. The CS₂ was HPLC-grade (glass distilled and filtered) and was contained in quartz spectroscopic cells with 1-, 2- or 10-mm optical path lengths. The diameter of the pump beams in the sample cell was 3 mm. Some of the experiments were performed focusing the probe beam into the sample cell. The phase conjugated beam I_c retraced the path of the probe and was detected by a fast photodiode (ITT F4000). The intensity was attenuated by three glass slides (G) which could be replaced by

mirrors when necessary. The reference pulse is detected by the same photo diode and precedes the conjugate pulse by 7 ns. Both pulses were measured using a Tektronix 500 MHz storage oscilloscope. The detection system was calibrated by placing mirror M_R in the path of the probe beam. Pulse energies were measured by a pyroelectric energymeter (Laser Precision RJ7200).

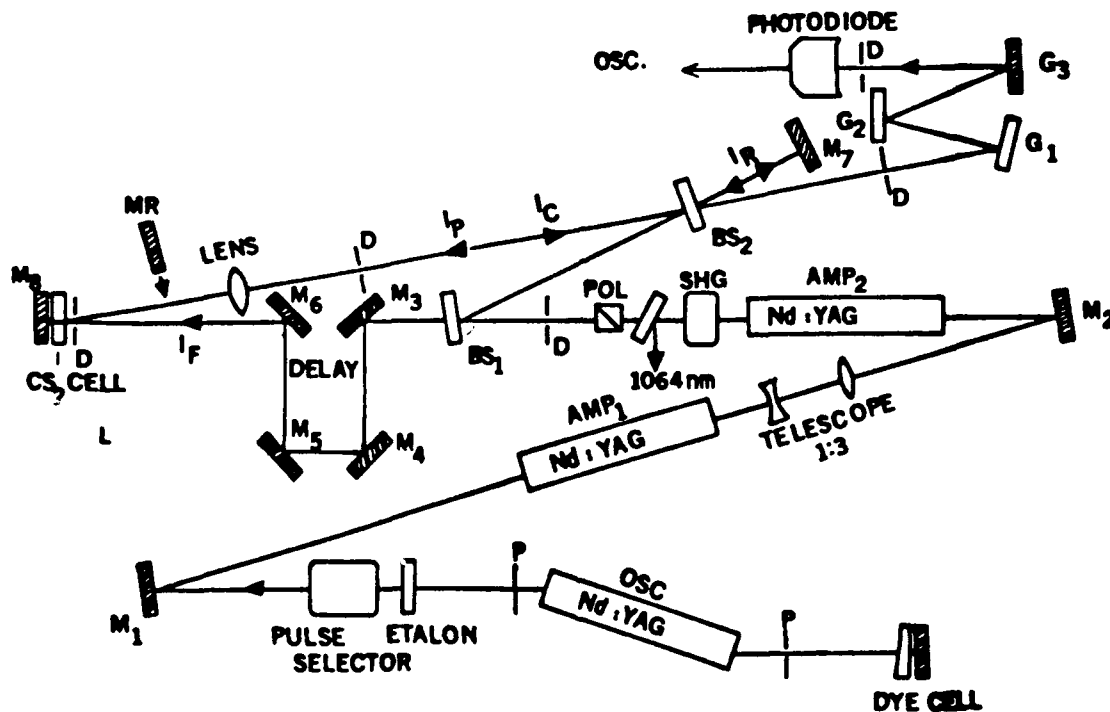


Figure 17. Experimental setup for the production of phase conjugation by degenerate four-wave mixing of picosecond pulses. The backward pump pulse is produced by retroreflection of the forward pump beam. M: mirror; D: diaphragm; SHG: second harmonic generator; I_F : forward pump beam; I_P : probe beam; I_C : phase conjugated beam; I_R : reference beam.

4.1.1.2 Experimental Results and Discussion. Using the experimental system described in the previous section, phase conjugate reflectivity was measured as a function of pulse energy for different values of probe to pump pulse fluence F_{pr}/F_f , for different ratios of the two pump pulse energies E_f/E_b and for different cell lengths L . Also, the presence of stimulated Brillouin scattering and whole beam self-focusing of the pump pulses were checked. Both of these nonlinear effects were found to be negligible. In an attempt to detect two-photon absorption in CS_2 , the transmission of picosecond

pulses was measured as a function of their energy. However no significant energy dependence of the transmission could be detected up to an energy of 5 mJ per pulse.

In the retroreflection setup, the maximum interaction length of the two pump beams is limited to one half of the pulse length, so it is advantageous to minimize wasted overlap.

In the first experiment a specially designed cell, 2-mm long, with the rear surface consisting of a dielectric mirror was used. Using this cell, the region of temporal overlapping of the two pump beams in the CS₂ was increased. Figure 18 shows a typical result for reflectivity versus pump pulse energy, using the special designed cell. The ratio of pump to probe pulse energy was 14. The decrease in the slope of the reflectivity versus energy was accompanied by a decrease in the quality of the phase conjugated beam, which was attributed to small-scale self-focusing; the pump pulse seems to break up in bright and dark regions, and this same distorted profile is transferred to the phase conjugate beam. The power density at which saturation takes place is about 1 GW/cm², although theory predicts a critical power threshold for macroscopic self-focusing in CS₂ at 10⁵ W. The short optical path length of the sample cell causes the self-focusing to occur outside the cell. In this case there is no change into the amplitude profile of the beam inside the cell, only a change in the phase profile, i.e., the shape of the wavefronts. According to Akhmanov a 1-mm cell containing a Kerr like medium acts as a thin lens with focal length z_f , given by Reference 16:

$$z_f = \frac{w_0^2}{4 I_0 n_2 L} \quad (71)$$

where w_0 is the 1/e beam radius at the cell entrance, I_0 is the intensity at the beam center, n_2 the nonlinear refractive index and L the cell length. At a power level $I_0 = 1 \text{ GW/cm}^2$, $w_0 = 3 \text{ mm}$ and $L = 1 \text{ mm}$, z_f equals 5 m in the case of CS₂. This shows that the short interaction region in picosecond FWHM, permitting the use of a short sample cell, reduces the effects of macroscopic or whole beam self-focusing.

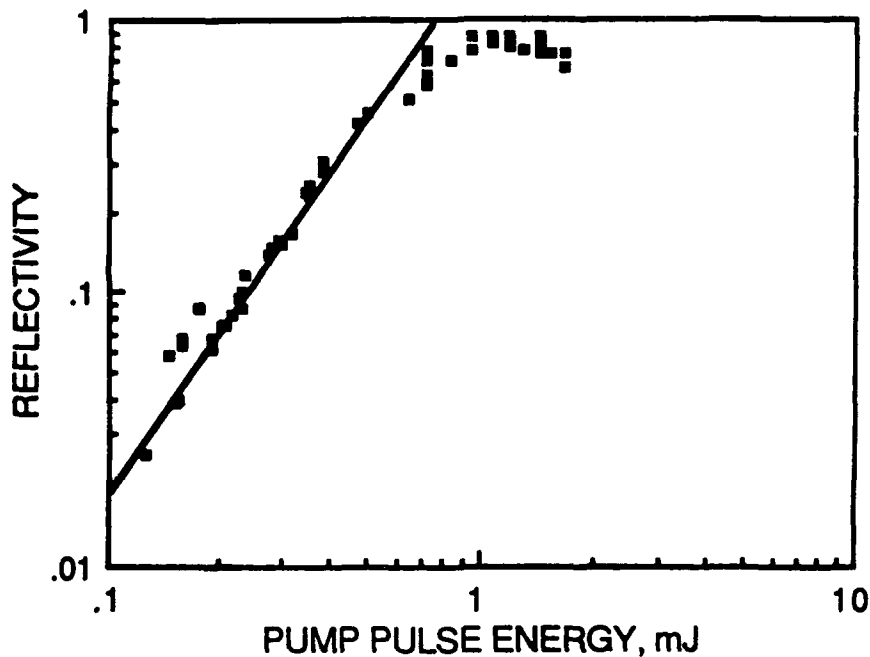


Figure 18. Phase-conjugate reflectivity of CS_2 in a 2-mm cell versus the pump energy in the forward pump beam, using a sample cell with retroreflection mirror within the sample. The pump/probe pulse energy ratio is 14:1. The curve clearly indicates the negative deviation from a square dependence of the reflectivity on the pump energy at high energies and is typical for most experiments we performed.

In order to determine the influence of a difference in energy of the forward and backward pump pulses, the conjugate reflectivity versus pump pulse energy was measured using a retroreflector with a reflectivity less than unity. Figure 19 shows reflectivity versus reduced energy curves for three different values of the backward to forward pump pulse energy ratio E_b/E_f . Taking into account the Fresnel losses at the sample cell window, the following values of E_b/E_f were measured: 0.91, 0.71 and 0.50. Reduced pump energy E_r is defined as the geometric mean of the forward and backward pump pulse energies E_f and E_b : $E_r = \sqrt{E_f E_b}$. Examination of the plot in Figure 19 makes evident the sharp decrease in efficiency with the increasing energy difference between forward and backward pump pulses. The solid lines represent the theoretical curves obtained using the model described in Reference 16. The wave vector k of an electromagnetic field depends on the intensity in a nonlinear medium since the refractive index is dependent on the electromagnetic field strength. Therefore, for two counterpropagating fields with identical vacuum wave vectors, k_f and k_b , within a nonlinear medium, $k_f + k_b$ will not be equal to zero, resulting in a phase mismatch of the

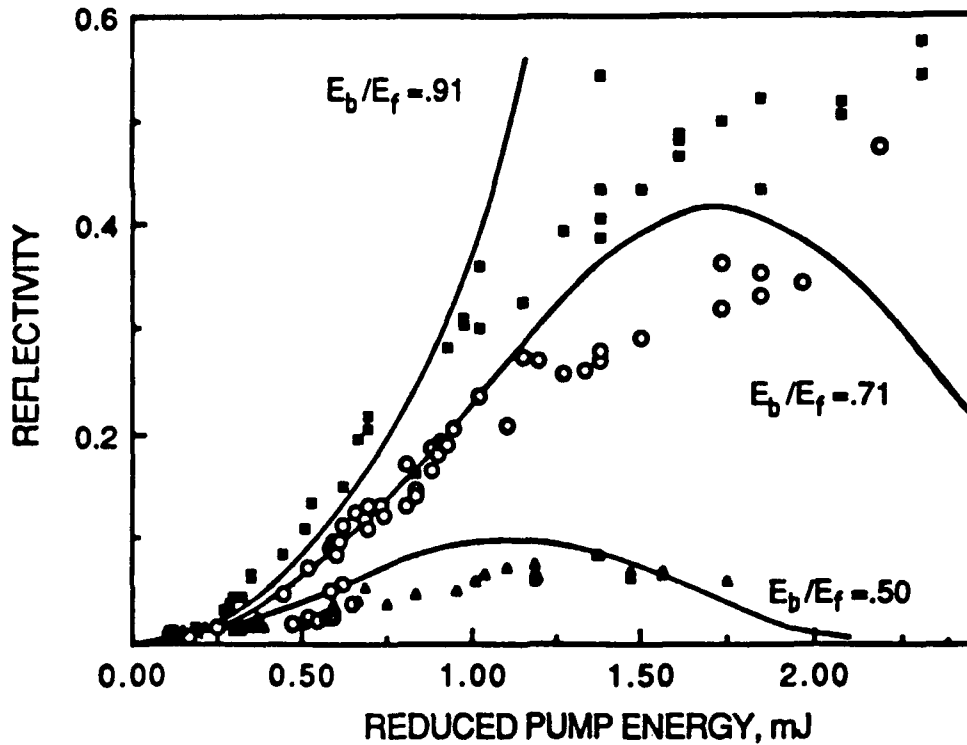


Figure 19. Phase conjugate reflectivity of CS_2 in a 2-mm sample cell versus the reduced pump energy E_r , for three different values of the ratio of backward to forward pump pulse energy E_b/E_f : (\blacksquare) 0.91, (\circ) 0.71, (\blacktriangle) 0.50. The solid lines are calculated curves, assuming a $1/e$ beam radius of 1.5 mm (see text). The ratio of forward pump pulse energy to probe pulse energy was 14:1.

four wave mixing process. If, however, the vacuum intensities are equal, then $k_f + k_b = 0$, and there should be no dephasing. The mismatch can be calculated as a function of the energy ratio r and the forward pump pulse intensity I_f , analogous to Reference 17:

$$|\Delta k| = |k_f + k_b| = \frac{9}{2} \omega \sqrt{\frac{\mu}{\epsilon}} x^{(3)} (1-r) I_f \quad (72)$$

Using the nonlinear coupling coefficient κ :

$$\kappa = \frac{9}{2} \epsilon \sqrt{\frac{\mu}{\epsilon}} x^{(3)} \sqrt{I_f I_b} \quad (73)$$

I_f and I_b being the intensities of forward and backward pump beam, the expression (Equation 72) can be written as following:

$$|\Delta k| = 9\kappa \left(\frac{1-r}{\sqrt{r}} \right) I_f \quad (74)$$

Using Equation 74, the phase conjugate reflectivity, R , with asymmetric pump beams can be calculated as follows:

$$R = \left[\frac{\sin^2(\kappa L \sqrt{1+p^2})}{\cos^2(\kappa L \sqrt{1+p^2}) + p^2} \right] \quad (75)$$

where $p = \frac{9}{2} (1-R/\sqrt{r})$ and L is the interaction length of the pump and probe pulses inside the nonlinear medium. The theoretical curves in Figure 19 were calculated using the value of $\chi^{(3)} = 2 \times 10^{-31}$ (SI units), leading to the following expression for the coupling constant in CS_2 :

$$\kappa = 0.21 I_f \text{ (MW/cm}^2\text{m)} \quad (76)$$

The curves were calculated assuming a beam diameter of 3 mm. For the ratio $E_b/E_f = 0.55$ the theory predicts the maximum reflectivity very well. The different maximum positions of the theoretical and experimental curves are attributed to the fact that the beam diameter was an estimate. These results show that for ratios E_b/E_f of 0.71 and 0.91 and at pump energies higher than 0.75 mJ, the experimental data for the phase-conjugate reflectivity fall below the theoretically expected values, even when the dephasing due to pump pulse energy asymmetry is taken into account. The experimental data shown in Figure 19 lead to the same conclusion, because in this experiment the pump pulse difference was minimized. The conclusion is that pump pulse asymmetry is not the limiting factor for the phase conjugate efficiency in these experiments.

A second important factor which limits the efficiency of phase conjugation is the depletion of the pump beams. It is obvious that the four-wave mixing process can never produce a conjugate pulse which has a higher energy density or fluence than that of the pump pulses. However, this effect has only seldom been taken into account when solving the coupled-wave equations for the optical phase conjugation (OPC) by degenerate four-wave mixing (DFWM) (Refs. 18,19). Numerical solutions to these equations, incorporating pump depletion, indicate no significant depletion effects when the pump to probe intensity ratio is higher than 10 (Ref. 19). In Figure 20 the results of six different experiments, each having a different ratio of probe to pump fluence F_{pr}/F_f are compiled. The maximum reflectivity obtained in each experiment is plotted as a function of the F_{pr}/F_f . In all experiments, except the one with $F_{pr}/F_f = 5$, this maximum was the saturation level of the reflectivity occurring at pump pulse energy levels above 2 mJ. Note that the power dependence in each of these experiments was measured by varying the intensity of the source beam so as to obtain reflectivity data at a constant pump to probe fluence ratio. In the normal setup, F_{pr}/F_f was equal to 0.05. In order to investigate the influence of variations in F_{pr}/F_f , this ratio was decreased by neutral density filters in the probe beam. At the lowest value of F_{pr}/F_f a reflectivity of more than 300 percent was obtained, which means phase conjugated amplification of the probe pulse. The reflectivity versus energy curve for this experiment is shown in Figure 21. Note that this curve shows very little saturation effect, as compared to Figure 18 for example. The cell length was 2 mm in this case. In the other extreme, where the ratio F_{pr}/F_f was increased to 5 by focusing the probe beam into the sample cell, a reflectivity of only 0.1 could be obtained. The probe beam was focused into the center of the collimated pump beams, reducing its radius by a factor of 10, causing the fluence of the probe beam to increase by a factor 100. However, focusing of the probe beam has been shown to increase the quality of the phase conjugation (Refs. 20,21): under certain conditions a lens transforms the probe beam to its spatial Fourier transform in the focal plane, located in the interaction region of the pump beams. In this case, the Gaussian reflectivity profile determined by the product of the pump pulse transverse intensity profiles, acts as a spatial filter, because the reflectivity is highest in the center of the Fourier plane, where the low spatial frequency components of the probe beam are concentrated. In this case the phase conjugated pump beam had the same diameter as the probe beam, whereas a phase conjugated reflection of a collimated probe

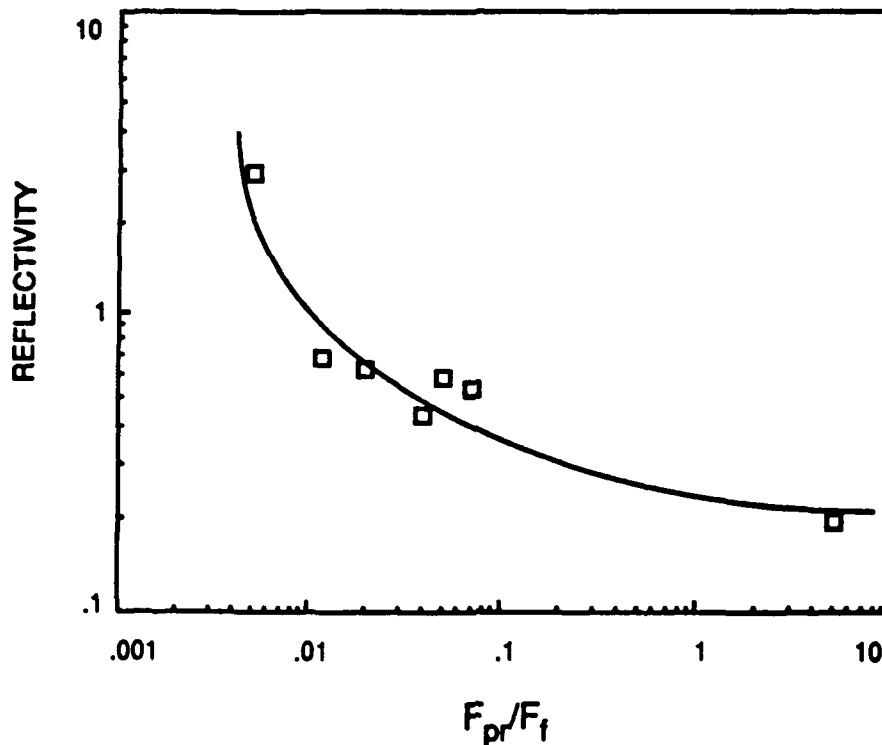


Figure 20. Maximum value of the phase conjugate reflectivity, as obtained from different experiments, plotted versus the ratio of probe pulse fluence to forward pump beam fluence, F_{pr}/F_f .

beam reduces its beam radius. The results, however, indicate that focusing of the probe beam leads to a stronger dependence of the PC-efficiency on the energy of the probe pulse, reducing the fidelity of the phase conjugation.

Self-focusing of the pump beams is very important as a limiting factor for the fidelity. Although whole beam self-focusing was never observed, the phase-conjugated beam at high pump pulse energy was degraded by small scale self-focusing, leading to beam breakup. Experiments using a 10-mm sample cell length, indicate a lower maximum reflectivity than 2-mm long cells. Normally one would expect a slight increase due to the increased overlap region. This effect is attributed to an increase of the wavefront distortions induced by small scale self-focusing in a longer sample cell.

In this discussion, generally, pump energy rather than pump intensity has been used as the independent parameter. It was not possible to measure accurately the beam diameters used in these experiments. Variation of the beam diameters is

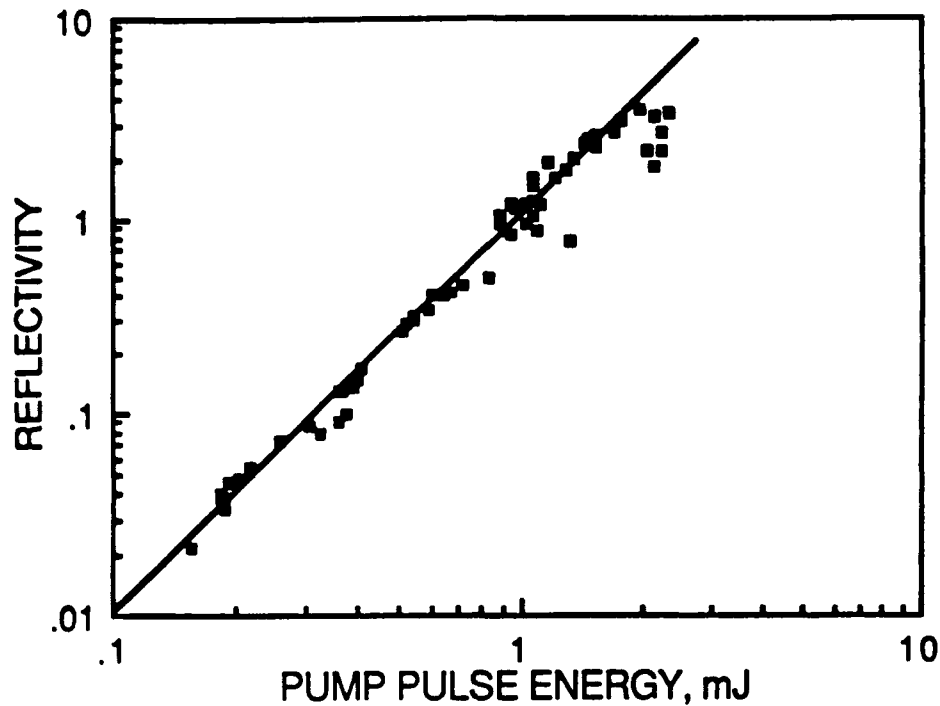


Figure 21. Phase conjugate reflectivity of CS_2 in a 2-mm cell, at a pump to probe energy ratio of 500:1, plotted versus forward pump pulse energy. A maximum reflectivity of 3 has been observed, i.e., an amplification of the phase conjugated reflection of the probe beam.

estimated to be 20 percent from experiment to experiment since realignment was involved. In addition to this, slight variations of the pulse width could occur due to changing concentration of the passive modelocker dye.

4.1.1.3 Conclusion. The efficiency of the phase conjugate reflection of picosecond pulses in CS_2 , a transparent optical Kerr medium has been measured. Very high reflection efficiencies were obtained although some saturation of the reflectivity at high fluences was observed. This was attributed to "small scale" self-focusing, which is a typical problem in high energy optical systems. The increased efficiency for the phase conjugation of short pulses in Kerr media is explained by the fact that the influence of the processes such as stimulated Brillouin scattering (SBS) and whole beam self-focusing, which limit the phase conjugate efficiency of nanosecond pulses, are reduced when picosecond pulses are used. In addition, a strong dependence of the phase conjugation efficiency on the ratio of the pump to probe fluences was observed.

4.1.2 Phase-Conjugation in Gold Colloids

4.1.2.1 Experimental Setup. Two types of gold colloid samples were used, a water-based colloid, prepared following the method of Turkevich (Ref. 22) and a solid glass-based sample obtained from Schott glass (sample type RG-6, 1mm thickness). A water-based colloid solution contains approximately 74 mg of gold per liter of water. Since the density of gold is 19.3 g/cm^3 , this corresponds to a total volume of $4 \times 10^{-3} \text{ cm}^3$ or a volume fraction ($\text{Vol}_{\text{gold}}/\text{Vol}_{\text{total}}$) of $\sim 4 \times 10^{-6}$. Typical values for the radius of the gold spheres in such solutions range from $\sim 40 \text{ \AA}$ to $\sim 120 \text{ \AA}$, corresponding to sphere volumes between 2.7×10^{-19} and $7.2 \times 10^{-18} \text{ cm}^3$. Electron micrographs indicated that particles in the solutions had an average radius of 120 \AA . This is equivalent to a number of spheres per liter ranging from $1.5 \times 10^{16}/\text{l}$ to $5.6 \times 10^{14}/\text{l}$. The water-based colloid had a local absorption maximum due to surface plasmons on the gold particles, measured by a Cary 219 spectrophotometer, of 2.76 cm^{-1} at 519 nm for a sample thickness of 2 mm . Similarly, the absorption of the Schott RG-6 sample had a local maximum of 9.21 cm^{-1} at 535 nm . This was superimposed on a background absorption, due to interband transitions, which becomes noticeable at $\sim 620 \text{ nm}$ and increases in magnitude as wavelength decreases. The width of the peak for the local maximum was approximately 100 nm for both samples before bleaching. After bleaching, the width could not be estimated accurately.

Optical phase conjugation measurements were made in two different pump intensity regions. The phase of the nonlinear susceptibility was measured by means of a nonlinear interferometer, described elsewhere (Ref. 23). A semiconductor colloid glass, whose $\chi^{(3)}$ (both magnitude and phase) was previously determined, was used in one arm as a reference and a gold colloid sample, whose phase was to be determined, was placed in the other arm. The interferometer operated at a wavelength of 532 nm via a CW mode-locked laser providing 1200 mW of average power at a repetition rate of 82 MHz . The peak intensities at the sample were ~ 1 to 2 kW/cm^2 .

Since the phase-conjugate reflectivities of most high speed (i.e. picosecond response) materials is very low at the low peak intensity levels of CW mode locked lasers (a few kilowatts per square centimeter), scattering is comparable to the P.C. reflectivities of $\sim 10^{-10}$ - 10^{-9} . For this reason, a lock-in amplifier was used in addition to a series of diaphragms to reject scattered light.

A pulsed Nd:YAG laser operating at 2 Hz and 532 nm was used for the high intensity phase conjugate (P.C.) reflectivity measurements (see Figure 22). A passively mode-locked oscillator was followed by a pulse selector, two amplifier stages, and a frequency doubling crystal. This provides a 25 ps, 532 nm pulse with a diameter of ~ 2 mm and energies ranging from a few tens of microjoules to a few millijoules. This pulse is split into four components. Two counterpropagating pump beams and one weaker probe beam are arranged in the counterpropagating DFWM geometry. The fourth component is used as a reference signal. The reference signal as well as the phase-conjugate signal are detected by high-voltage vacuum photodiodes. These are scanned by gated integrators at a 4 ns gate width (long enough to allow for trigger jitter and short enough to minimize detection of stray light). These integrators, in turn, are monitored with a computer interface (A/D conversion) and ultimately the data are manipulated by a DEC microvax computer.

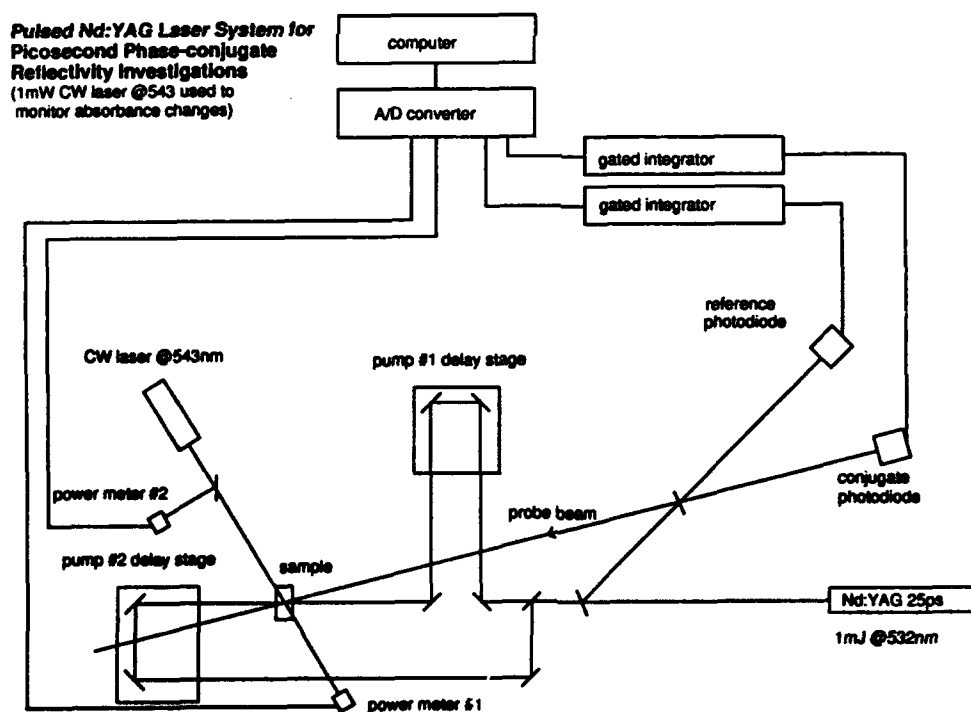


Figure 22. Laser system for high intensity, picosecond DFWM experiments.

The water-based colloid suspension was studied both in a static, closed cell and in a flowing cell in circuit with a 200-cc reservoir. The flowing cell arrangement was used to minimize the influence of sample deterioration during reflectivity measurements, while the static cell was used for absorption band measurements before and after damage.

During some experiments, the bleaching of the gold colloid glass was monitored by measuring the absorption in the sample. The intensity transmitted through the four wave mixing region in the sample was measured by a photodiode, as well as a reference signal. Thus, this system could monitor the influence of each successive laser pulse on the absorption of the gold colloid sample. The absorption monitor at 543 nm was assumed to be indicative of absorption changes at 532 nm, the wavelength at which the phase conjugation experiments were carried out.

4.1.2.2 Results. Data from the high-energy, pulsed YAG laser for gold colloid glass and water suspensions provided a power dependence reference for the phase conjugate reflectivity for intensities ranging up to a few gigawatts per square centimeter (Figures 23, 24a). In the initial studies, the probe beam power was ~ 10 percent of the pumps and in later experiments it was adjusted to be 50 percent of the pump power. No qualitative difference (due to the probe/pump ratio change) was detected in the structure of the measured reflectivity power dependence. At these low overall reflectivities, no influence from pump depletion was expected since a probe intensity comparable to a pump still would drain the pump by only 0.001 percent.

Data for the water-based suspension indicate that the reflectivity does not vary significantly with pump intensity in the region of ~ 500 MW/cm². This does not mean that the P.C. reflectivity is constant but rather that it does not vary strongly and certainly does not vary quadratically with the pump intensity as would be expected for a P.C. process.

For the water suspension, some experiments indicated a "flat" spot or local maximum in the intensity dependence at a pump energy flux of a few hundred micro-joules. At higher pump intensities, the reflectivity begins to rise again as a function of pump intensity. It is difficult to specify this power dependence analytically since, in the

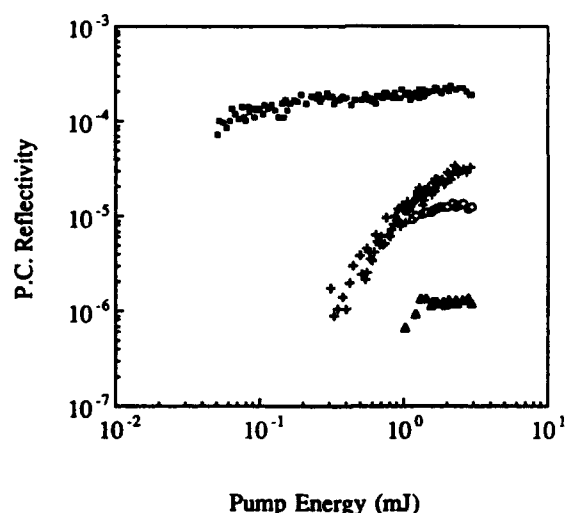
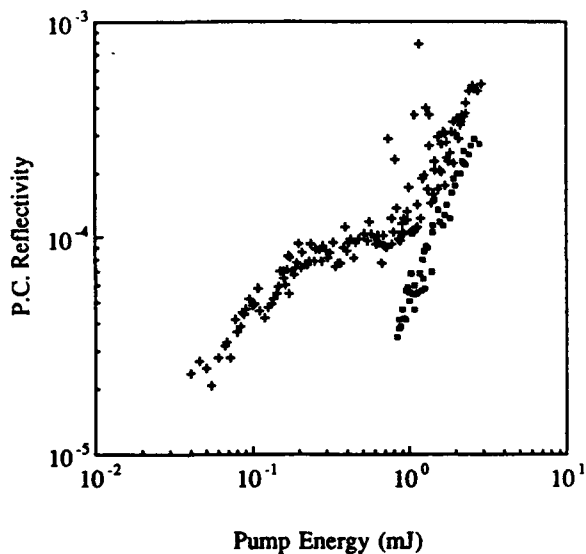


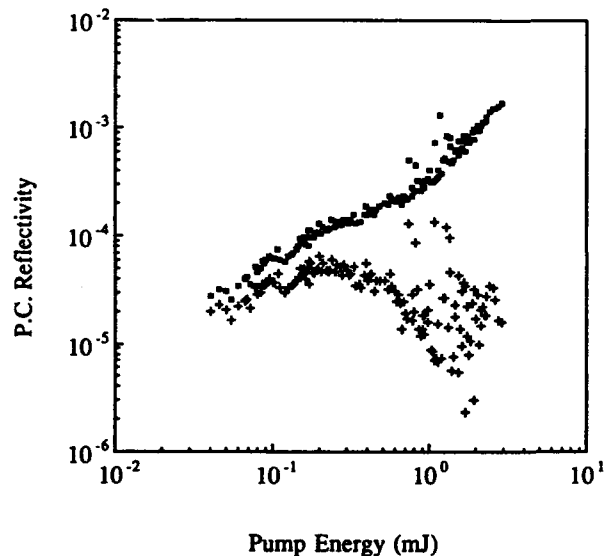
Figure 23. Phase conjugate reflectivity of Schott RG-6 gold colloid glass for high pump intensity, probe/pump ratio = 0.1, low repetition rate, 25 ps pulses for all beams incident (■); pump 1 blocked (○); pump 2 blocked (△) and all beams incident on an undoped glass sample (+). The flat response for gold glass is largely due to the formation of permanent gratings in the sample. All beams are linearly copolarized.

pump energy range, the slope of the curves varies continuously on a logarithmic scale but the range is not large enough to assign an exponential power dependence (Ref. 19). At first glance, these power dependence curves do not display characteristics that would be associated with the usual approximations (i.e. "tangent-squared" power dependence or saturation of reflectivity). These results will be discussed below.

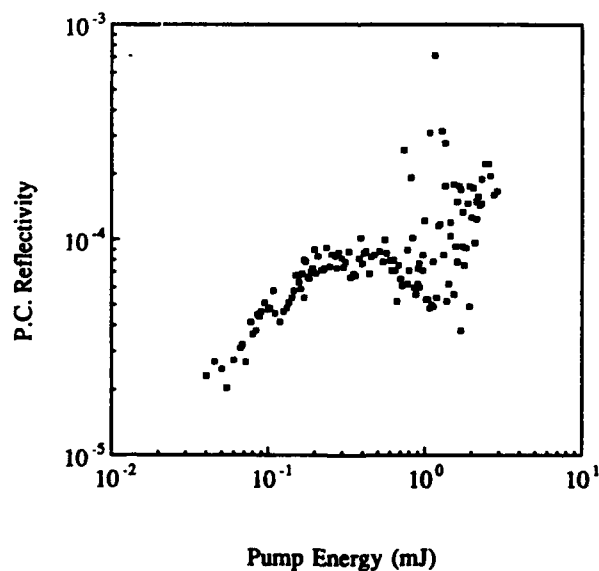
During exposure to the high power pulsed laser, the Schott RG-6 glass gold colloidal suspension developed permanent gratings which caused the "phase conjugate" reflectivity to remain approximately constant over a wide pump beam energy range. One possible (partial) explanation for this result is the possibility of total particle decomposition in the regions of the antinodes of the optical standing waves. Thus, the total diffraction grating would be the sum of the linear gratings formed by sample damage and the nonlinear gratings which still exist at the nodes of the optical standing waves. If the linear contribution is assumed to dominate in the experiment, constant reflectivity would be expected. Interestingly, the total phase conjugate signal is significantly greater than the sum of the two "separate" permanent gratings, i.e. the signals detected when one or the other of the pump beams was blocked. This implies the



(a) Phase conjugate signal for water-based gold colloid (+) and plain water (■) in a 2-mm flow-through cell.



(b) Phase conjugate reflectivity if the signal from the water and cell is assumed in phase (+) and antiphase (■) with that of the gold particles.



(c) Phase conjugate reflectivity when water and cell nonlinearities are assumed to be real and that of the gold particles are assumed to be imaginary. All beams are linearly copolarized.

Figure 24. Phase conjugation signal for water-based gold colloid and plain water in a 2-mm flow-through cell.

dominance of the nonlinear contribution, in direct contradiction to the initial premise. A hand-waving solution is to say that the nonlinear solution dominates with saturation of the nonlinearity being the crucial factor in the case of all beams incident on the sample.

There was also a permanent change in the absorption of the colloids, both liquid and solid (Figures 25, 26), upon exposure to the high-power pump pulses. This appeared as a "bleaching" of the colloid or occasionally the appearance of a pale bluish spot. These changes appeared to be permanent. Data from the spectrophotometer confirmed this; absorption dropped in the blue and increased in the red wavelength region.

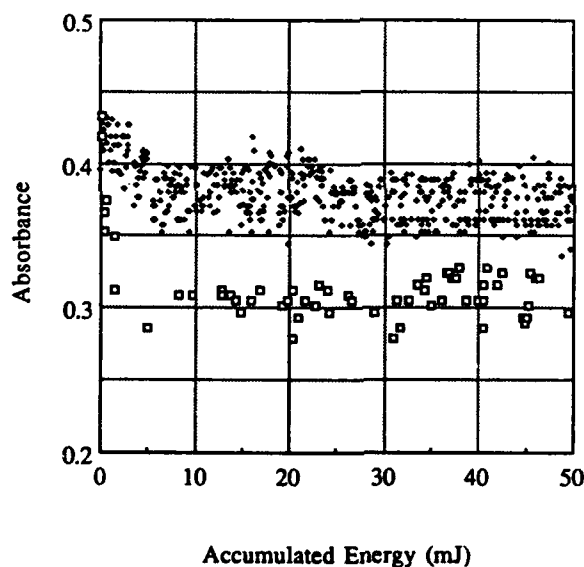


Figure 25. Change in optical absorption at $\lambda = 543$ nm of Schott RG-6 as a function of total energy flux from pulsed Nd:YAG laser ($\lambda = 532$ nm) for average pulse energies of 0.1 mJ/pulse (+) and 1.0 mJ/pulse (□).

The change in absorption in a Schott #RG-6 filter, as a function of accumulated laser energy incident upon the sample spot was measured for two different average laser pulse energies, 0.1 mJ and 1.0 mJ (Fig. 25). Note that, upon interrogation by 1 mJ pump pulses, the absorption at 543 nm has permanently dropped from 0.41 to 0.3 after only a few millijoules of accumulated energy. For the same total accumulated energy flux, the lower energy pulses have done far less damage. The most extreme

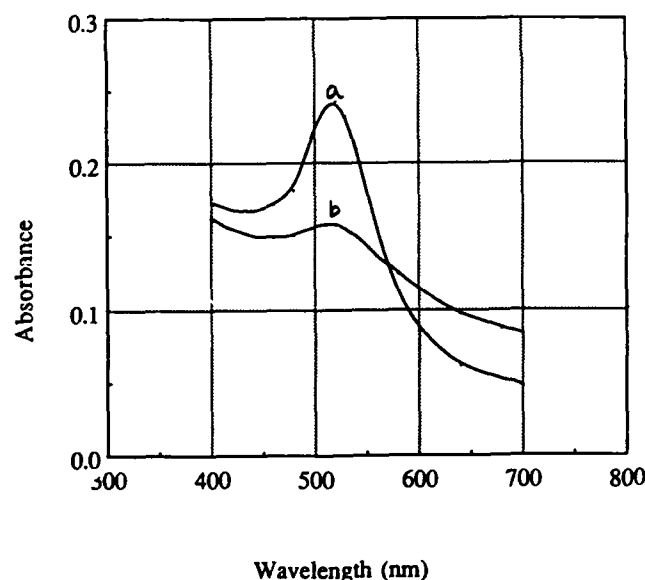


Figure 26. Continuous absorption of water-based gold colloid in a 2-mm cell before (a) and after (b) sample damage.

case, namely irradiation with a few hundred millijoules per second from the CW mode-locked Nd:YAG laser, did not result in any change in absorbance although the accumulated energy was many orders of magnitude larger than the pulsed laser provided.

At the highest pulse energies, there was also an increase in the far field spot size of the phase conjugate; the transmitted probe pulse showed a similar phenomenon. Since the transmitted probe pulse shares this "bloomed" appearance (generally appearing as a somewhat distorted series of concentric rings) in the far field, the most probable cause of the phase-conjugate "bloom" structure is that it is an accurate replication of the self-focusing or self-defocusing of the probe signal. That this phenomenon occurs at high intensities is expected; the self-focusing or self-defocusing phenomenon is also due to the third order nonlinear susceptibility.

Figure 27 shows phase conjugate signal interference and pump signal interference from Schott RG-6 gold colloid glass and Schott OG-530 semiconductor colloid glass as a function of the delay of one arm of the interferometer. Since the maxima and minima of the two signals coincide and the phase of $\chi^{(3)}$ of OG-530 is known to be negative and real, it was determined that for the high repetition rate, low peak intensity (2 kW/cm^2) laser pulses, the phase of the total third order nonlinear susceptibility for the

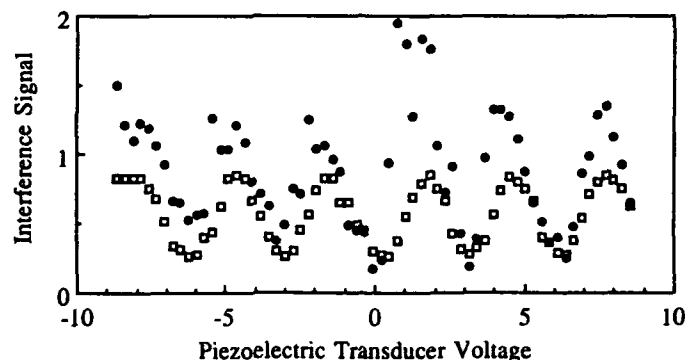


Figure 27. A comparison of the interference of conjugate signals (●) and reference signals (□) from Schott RG-6 gold colloid glass and Schott OG-530 semiconductor colloid glass as a function of delay in the arm of the nonlinear interferometer. Since the phase of the P.C. signal from OG-530 is known to be negative and real in this region, the phase of RG-6 must be the same.

gold colloid sample is negative and real. In other words, for $\chi^{(3)} = \chi_{\text{real}} + i\chi_{\text{imaginary}}$, it was determined that the effective $\chi_{\text{imaginary}}$ is negligible compared to χ_{real} and that χ_{real} is negative. Since the colloid sample is actually a composite system, this $\chi^{(3)}$ cannot be attributed to the particles without further assuming that the nonlinear susceptibility of the glass matrix is insignificant compared with that of the gold particles at this power level. Evidence supporting this claim is that a plain glass sample of 1-mm thickness did not provide a detectable phase-conjugate signal when pumped by the CW mode-locked laser of the Twyman-Green interferometer. Therefore, the negative and real nonlinear susceptibility is attributed to the gold particles.

4.1.2.3 Conclusions. The intensity dependence of the picosecond phase-conjugate reflectivity in gold colloids for pump intensities on the order of 1 GW/cm^2 has been determined experimentally; the intensity dependence of sample damage and the phase of the nonlinear susceptibility of gold colloids has been investigated via interferometric methods using a CW-mode-locked Nd:YAG laser; and also the significance of the phase relationship of the nonlinear susceptibilities in a multi-component system has been recognized. This is significant in an applications environment since the functional intensity dependence could have its shape "tailor-made" by adjusting the stoichiometry of the constituents.

4.2 COHERENT TWO-WAVE MIXING EXPERIMENTS

4.2.1 Experimental Setup

A pulsed Nd:YAG laser operating at 4 Hz was used for the two-wave mixing experiments. The laser system consisted of a passively mode-locked oscillator which provided a pulse train of ~ 10 35-ps pulses at $\lambda = 1.064 \mu\text{m}$. A pulse selector directed one of the most intense pulses of the train to a double-pass Nd:YAG amplifier. The selected pulse was chosen from the leading half of the pulse train to minimize the influence of pulse chirp on the two-wave mixing. This pulse was subsequently frequency doubled in a KDP (KH_2PO_4) crystal and residual 1.064 μm radiation was then eliminated by a harmonic beam splitter. Pulse energies at 532 nm were on the order of 1 to 5 mJ, depending on the experiment, with a standard deviation of 25 percent within any one experiment. In all cases, the beam diameter was ~ 2 mm and was approximately Gaussian.

The 532 nm pulse is split into two components, corresponding to the pump and probe pulses. Another beam splitter deflected roughly 8 percent of the pump pulse into a detector for normalization purposes. The final input intensity (and energy) ratio was variable with $1 < I_{\text{pump}}/I_{\text{probe}} < 10$ depending on the beam splitter selected. A delay stage in the pump beam path controlled the relative arrival times of the pump and probe pulses in the sample. The angle between the pump and probe wavevectors, outside the sample, varied depending on the experiment, from $< 0.3^\circ$ (~ 4 mrad) to $\sim 4.5^\circ$ (~ 78 mrad). Since these pulses provided intensities on the order of 10^9 W/cm^2 , focusing the beams was unnecessary. The initial pump reference and final probe energies were measured as a function of their relative arrival times in the sample by pyroelectric detectors. The analog output of these meters were sent to an A/D converter which was interfaced with a computer. The apparatus is shown schematically in Figure 28.

In some experiments both the pump and probe were linearly polarized, in others the pump was circularly polarized and the probe was linearly polarized. For the experiments in which the pump pulse had circular polarization, the probe pulse had polarizing beam splitters before and after the sample. One of the motivations for an interaction of a circularly polarized pump and a linearly polarized probe was to minimize the influence of the "Kerr Shutter" effect. It is well known that a strong, linearly

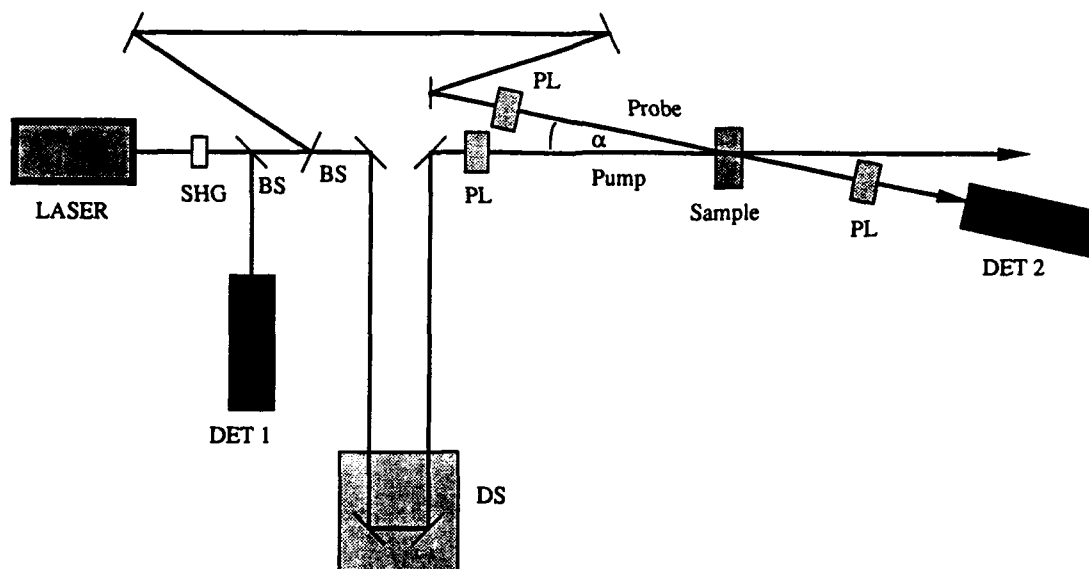


Figure 28. Experimental apparatus and beam geometry for degenerate two-wave mixing. PL = polarizer; DET = detector; DS = delay stage.

polarized pump causes a transient linear birefringence in Kerr media; this effect is often used to rotate the polarization of a probe pulse and thus "time" two picosecond pulses via the "Kerr shutter." A circularly polarized pump causes a transient circular birefringence in a material, but this effect is expected to be insignificant in comparison to the linear effect. For this reason, it is expected that any net change in the measured probe energy is a result of energy transferred from the pump rather than polarization rotation of the probe energy.

In a third group of experiments, both pump and probe pulses had circular polarizations; a comparison was made between an interaction of pulses with identical polarization helicity and an interaction of pulses with opposite polarization helicity.

The samples included carbon disulfide, nitrobenzene, semiconductor colloid glass and a water-based gold particle colloid. The liquid samples were contained in quartz cells of various thicknesses. All of these materials should have nonresonant electronic polarizabilities with response times on the order of 10^{-15} s; they should have additional response times corresponding to molecular reorientation, and various decays from other excited states. Carbon disulfide has a characteristic response time of ~ 1 ps (Ref. 28) and nitrobenzene has two characteristic response times, ~ 8 ps and a few

nanoseconds (Refs. 24,25). Likewise the semiconductor glasses have two: ~ 30 ps and a few nanoseconds (Ref. 26). Finally, the water-based gold colloid should have a very fast response corresponding to a surface plasmon decay (Refs. 27,28,29) as well as a much slower response due to thermal effects.

4.2.2 Experimental Results

The initial experiments were designed to produce visible self diffraction; this phenomena is fairly well understood (Ref. 30) and the experiment is facilitated by the fact that the propagation directions of the diffracted orders allows detection of the process by eye. At small angles, several orders of self diffraction are visible when using CS_2 as the active medium. A sample thickness of ~ 5 mm showed the best compromise between the intensity of each diffraction order and the number of diffraction orders. Sample thicknesses of 1,2, and 10 mm also provided visible self diffraction, but the 1- and 2-mm cells did not provide as much diffracted beam intensity as the 5-mm sample while the 10-mm sample gave more intense diffracted beams but fewer visible orders of diffraction. All visible self diffraction disappeared for angles larger than $\sim 2^\circ$ (35 mrad). Self diffraction was present both in the case of a circularly polarized pump and a linearly polarized pump but the intensity was visibly higher in the case of parallel linearly polarized pump and probe pulses. Semiconductor colloid glasses and nitrobenzene also displayed self diffraction effects, though not to extent of the CS_2 sample.

Once the influence of self diffraction had been verified, the energy of the transmitted probe pulse relative to the pump reference signal (before the sample) was monitored. In these first experiments, an increase in the probe energy of as much as ~ 10 percent was measured, depending on the relative positions of the pump and probe pulses. At some positions, there was an apparent slight loss in the probe energy, but this loss was of the same magnitude as the noise of instrumentation so its presence was neglected at that time. The angle between the pump and probe pulses was then increased to $\sim 4.5^\circ$ where the higher diffraction orders were weak enough to be considered insignificant. It was found that the probe gains and losses were present even without the influence of self diffraction.

By further experimentation, the losses and gains of the probe were successfully quantified as functions of several parameters. In all of the experiments, the laser

intensities were typically on the order of 1 GW/cm^2 . The time axes shown on Figure 29 are not absolute. Although the scales are accurate, the origin has been arbitrarily assigned. The actual origin (location of zero delay between the pump and probe) is located in the region of pump probe overlap. For an experiment in which the pump and probe are initially identical, it may be easily deduced that the origin occurs where the net energy transfer is zero (at the crossing point). For other configurations, the origin is shifted slightly with respect to the crossing point.

When the semiconductor colloid sample was tested (Figure 29), the results were those of a typical pump-probe transient absorption experiment: when the output probe polarization parallel to the input probe polarization was monitored, there was increased transmittance (or decreased absorption) when the pump pulse passed through the sample first. The decay of the transmittance corresponds to the excited state free carrier decay in the semiconductor. There was also a coherence spike (Ref. 34) superimposed on the transient absorption background. When the output probe polarization perpendicular to the input probe polarization was monitored, there was only a "coherence spike" present. The width of this spike was $\sim 15 \text{ ps}$.

The gold colloid also displayed (Figure 30) a coherence spike in the perpendicular polarization, but the excessive noise in the parallel polarization experiment precluded the detection of any coherent phenomena here. Interestingly, the gold colloid showed an increased probe transmittance for all times when the pump passed through the sample first. It is believed that particle damage is an important process at these high intensities and can explain the apparently permanent change in transmittance. The nonlinear coupling in the gold colloid proved to be the weakest coupling in the materials studied.

The most interesting results (Figures 31, 32) appeared for the Kerr media, CS_2 and nitrobenzene. Both of these materials showed a "coherence spike" representing energy transfer from the circular pump pulse to the probe pulse in the polarization perpendicular to the original probe polarization. The width of the spike in the CS_2 sample was approximately 40 ps and the peak energy transfer corresponded to ~ 30 percent of the probe input energy. The corresponding peak energy transfer in the nitrobenzene was ~ 15 percent. The width of the spike in nitrobenzene could not be easily defined as it apparently had a narrow spike (of width $\sim 15 \text{ ps}$) superimposed on a broader ($30\text{--}40 \text{ ps}$) coherent background. Similar phenomena (i.e., probe diffraction experiments) have been

a) the polarization perpendicular to that of the initial probe polarization.

b) the polarization parallel to the initial polarization.

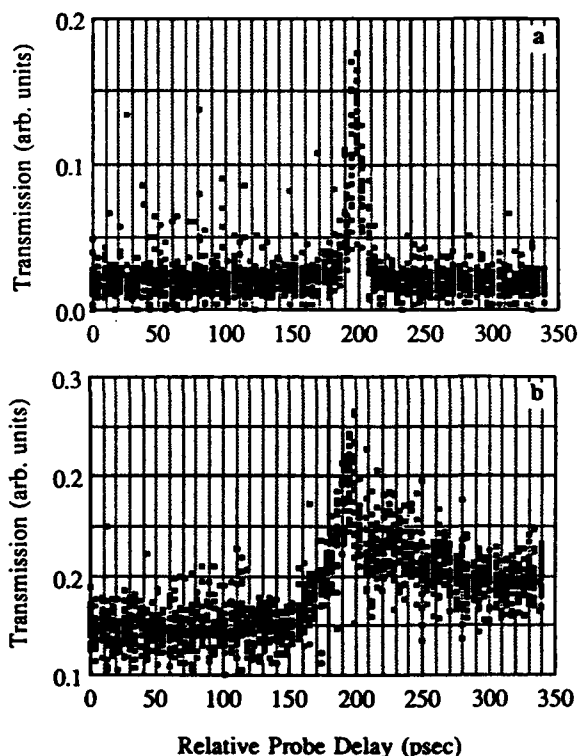
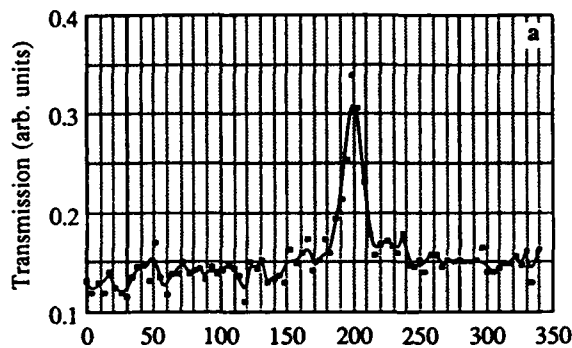


Figure 29. Change in probe transmission in a semiconductor doped glass sample as a function of relative probe delay. Synchronization of the pump and probe occurs at ~ 200 ps on the graphs (i.e., axis origin is arbitrary). Each point represents one laser shot.

discussed by several researchers (Refs. 30,31,32). The shape (intensity) of the diffracted signal as a function of probe delay is explained by considering the pulse durations (causing the broad background) and the coherence time of each of the pulses (causing the narrower spike centered on the broad background) in materials with transient grating decay times which are large compared to the coherence time and pulse length, so that an "integrated-intensity" grating may be assumed.

The 15 to 20 ps coherence spikes in both the nitrobenzene and semiconductor-doped glass samples suggest, therefore, that the laser pulses are not transform-limited. This is expected since passively mode-locked lasers typically have incomplete mode-locking.

a) the polarization perpendicular to that of the initial probe polarization.



b) the polarization parallel to the initial polarization.

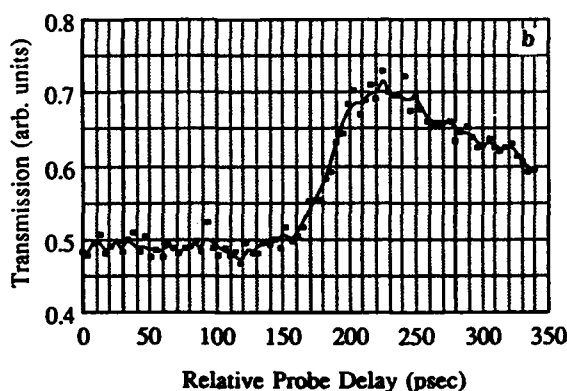
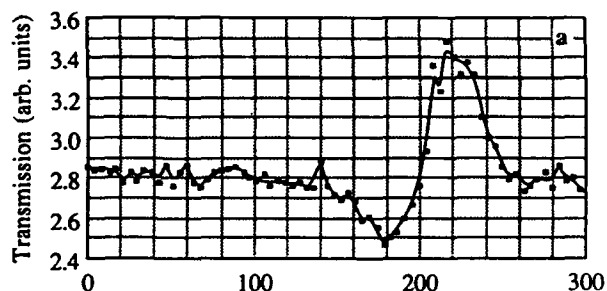


Figure 30. Change in probe transmission in a liquid gold colloid sample as a function of relative probe delay for monitoring: Synchronization of the pump and probe occurs at ~ 200 ps on the graphs (i.e., axis origin is arbitrary). Each point represents 20 laser shots.

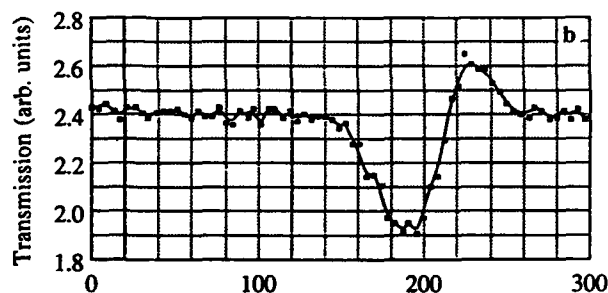
The intensity of the coherence spike was measured as a function of pump intensity in CS_2 . For normalization purposes, the energy of the probe coherence spike was divided by the incident laser energy. Figure 33 shows the expected square law dependence on the incident beam intensity.

In the case of the output probe polarization being parallel to the input polarization, the coherent signal from CS_2 was antisymmetric with respect to pump and probe relative delay times. When the pump pulse arrived in the sample slightly before the probe pulse, there was a net energy transfer from the pump into the probe. This energy transfer was on the order of 20 percent of the initial probe energy. When the probe arrived in the sample slightly before the pump pulse, it lost ~ 20 percent of its initial energy. This result is in agreement with the set of integro-differential equations presented earlier. Examination of the factors $(A^2 - B^2)$ in the coupled field amplitude

a) no polarization discrimination.



b) polarization parallel to the initial probe polarization.



c) polarization perpendicular to the initial probe polarization.

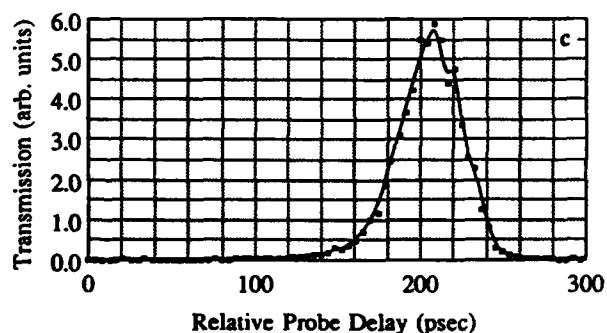


Figure 31. Change in probe transmission in a CS_2 sample as a function of relative probe delay. Synchronization of the pump and probe occurs at ~ 200 ps on the graphs (i.e., axis origin is arbitrary). Each point represents 20 laser shots.

equations indicates that a reversal of leading and trailing pulses is expected to result in a reversal of the direction of energy transfer. Experimental results were inconclusive for nitrobenzene; although the nonlinear optical susceptibility of nitrobenzene has a component with a relaxation time comparable to the pulse width, the excitation of the nonlinearity is not instantaneous and therefore the effective nonlinear excitation by these laser pulses is diminished. The magnitude of the transfer was apparently < 10 percent of the probe energy. However, the noise levels of the instrumentation prevented quantification.

a) the polarization parallel to that of the initial probe polarization.

b) the polarization perpendicular to the initial polarization.

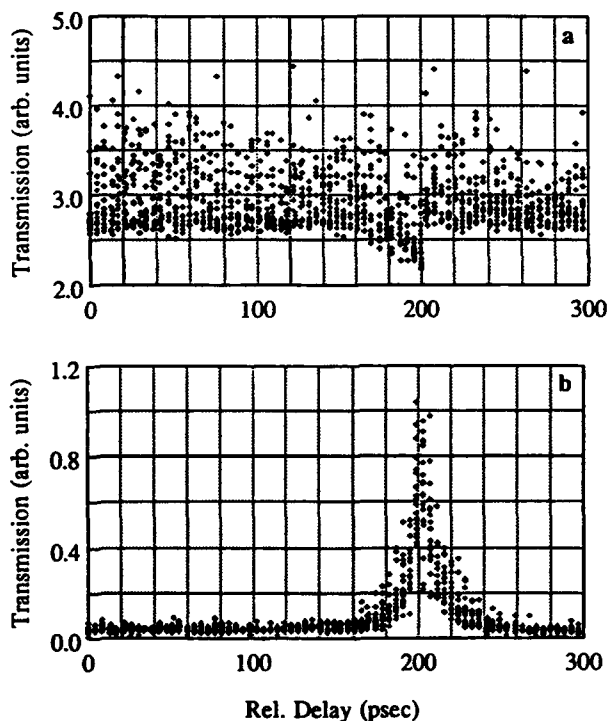


Figure 32. Change in probe transmission in a nitrobenzene sample as a function of relative probe delay. Synchronization of the pump and probe occurs at ~ 200 ps on the graphs (i.e., axis origin is arbitrary). Each point represents a laser shot.

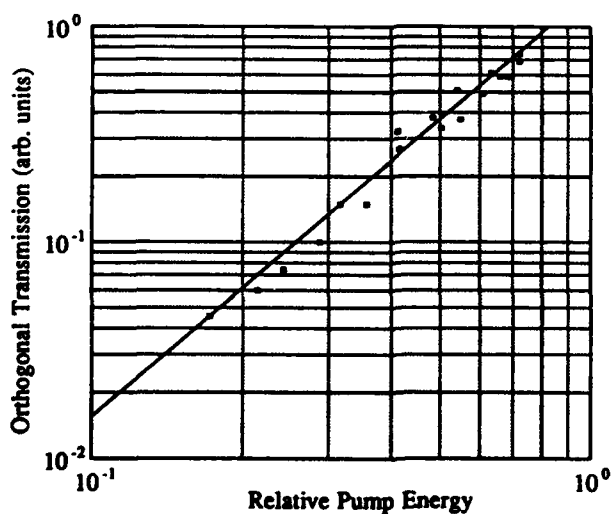


Figure 33. Change in probe transmission in the polarization orthogonal to that of the initial probe polarization as a function of pump energy in the region of ~ 1 mJ per pulse.

Experiments were also carried out in CS_2 as a function of different initial energy ratios between the pump and probe pulses for two polarization combinations: linear-pump/linear-probe and circular-pump/linear-probe.

In the experiments with pump and probe beams having parallel linear polarizations (Figure 34), the results were generally not strictly antisymmetric as a function of pump-probe relative delay. As the initial pump/probe intensity ratio increased, the probe's maximum gains further exceeded its maximum losses. For example, imagine a case in which the pump intensity is initially three or four times that of the probe. If the probe preceeded the pump, it might lose 2 percent of its energy to the pump as they passed through the sample. If instead the pump preceeded the probe, the probe might experience gains of 6 to 7 percent. Even in the case of initially equivalent pump and probe intensities, the antisymmetric coherent signal is present. In this case, the probe's (or pump's) maximum gains should be the same as its maximum losses. However, the situation is complicated experimentally by the simultaneous occurrence of self diffraction. The energy exchange increases with increasing interaction length, while the finite beam diameter requires small intersection angles for a long overlap length. Unfortunately, self-diffraction increases with decreasing intersection angles. The result is that energy is drained from both the pump and the probe samples as they pass through the sample. This means that the maximum net gain for the probe (and pump) is decreased, while the maximum net loss is increased due to the presence of the self-diffraction.

In order to verify this, measurements were made (Figure 35) as a function of the intersection angle for an initial pump/probe intensity ratio of unity. At small angles, the probe's losses were indeed greater than its gains; as the intersection angle increased, the probe's gain indeed became antisymmetric as a function of pump/probe delay.

Analogous experiments were performed using a circularly polarized pump pulse with a linearly polarized probe. In this case, higher initial pump/probe intensity ratios resulted in lower maximum probe gains and higher maximum probe losses. Again, as the initial pump/probe intensity ratios approached unity, the probe's maximum losses became comparable to its gains. The influence of the self diffraction was similar to that in the linear polarization experiments.

a) Initial pump probe intensity ratio of 5/1.

b) Initial pump probe intensity ratio of 3/1.

c) Initial pump probe intensity ratio of 2.5/1.

d) Initial pump probe intensity ratio of 2/1.

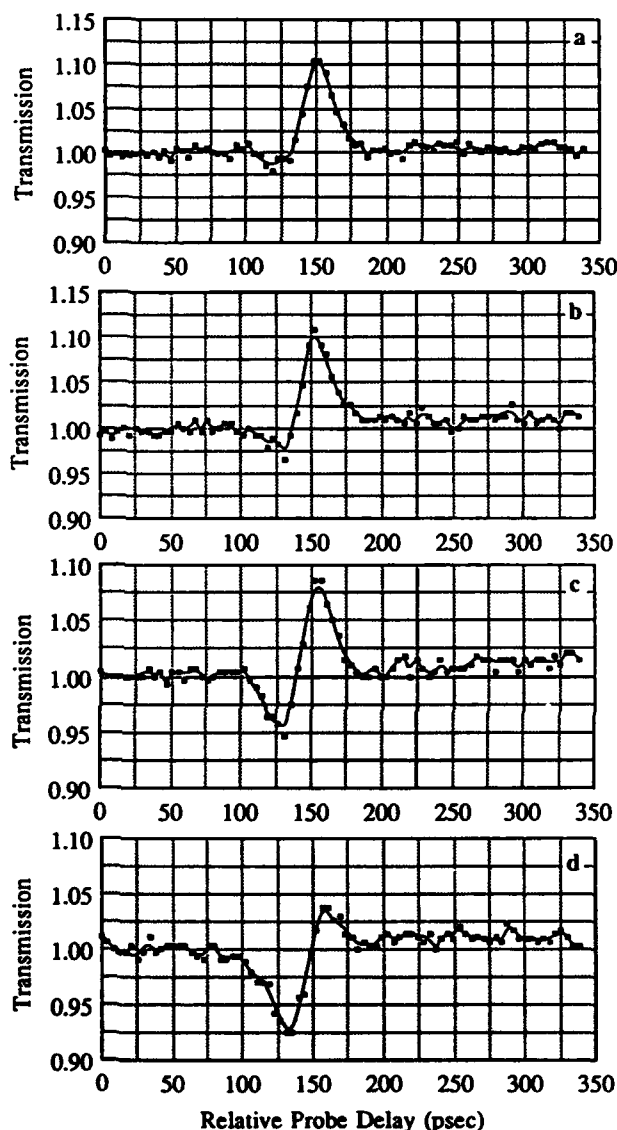


Figure 34. Change in probe transmission in a CS_2 sample as a function of relative probe delay for monitoring the polarization parallel to the initial polarization for four initial pump probe intensity ratios for an intersection angle of $\sim 0.5^\circ$. Synchronization of the pump and probe occurs at ~ 150 ps on the graphs (i.e., axis origin is arbitrary). Each point represents 20 laser shots.

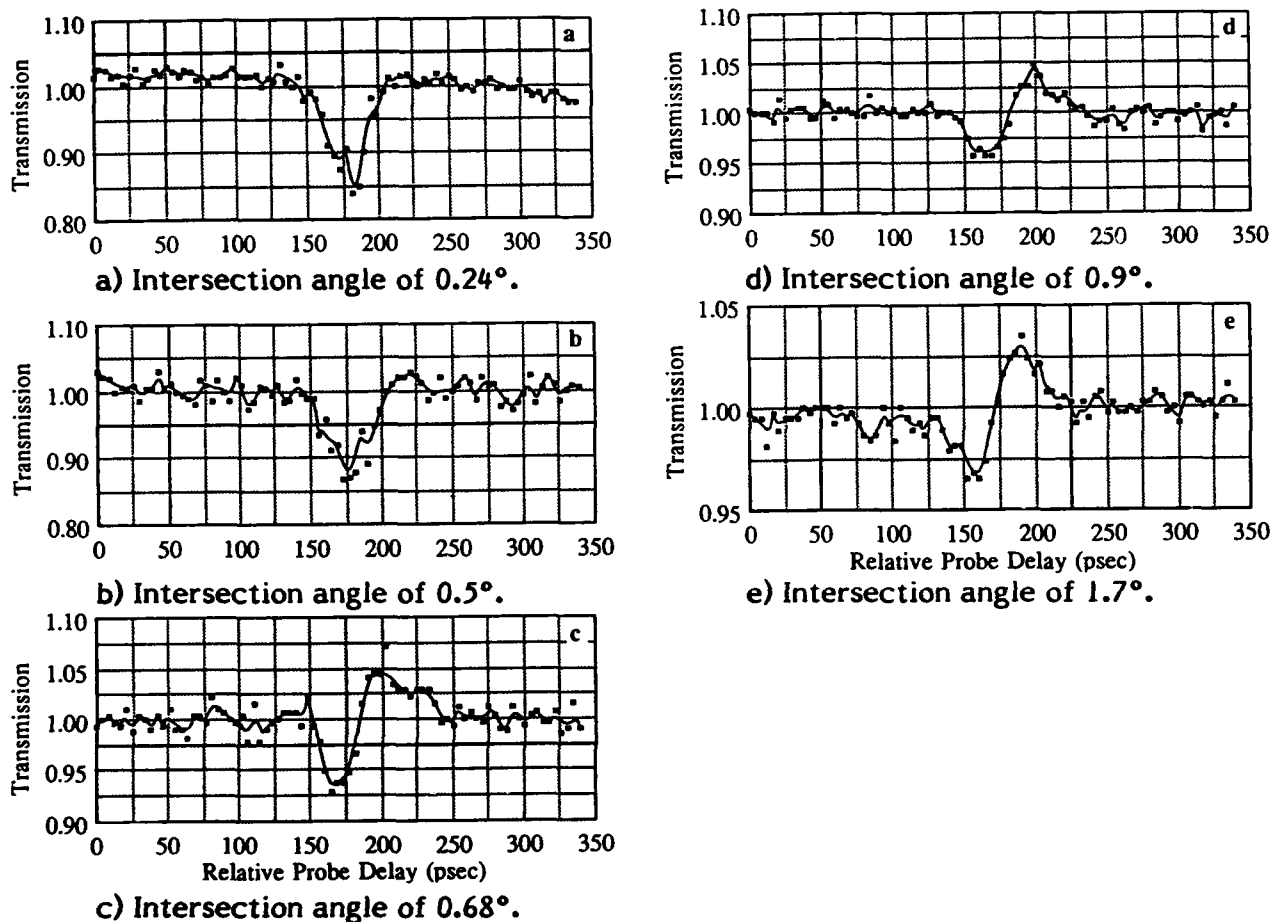
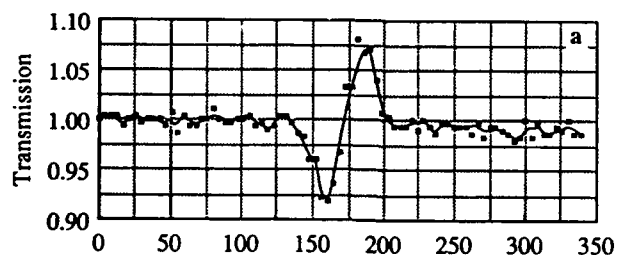


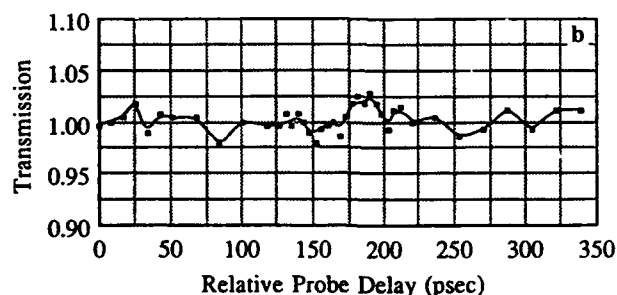
Figure 35. Change in probe transmission intensity in a CS₂ sample as a function of relative probe delay for monitoring the polarization parallel to the initial polarization for five intersection angles. Synchronization of the pump and probe occurs at ~ 150 ps on the graphs (i.e., axis origin is arbitrary). Each point represents 20 laser shots.

A final experiment in CS₂ demonstrated that the nonlinear coupling of two pulses with identical circular polarization was significantly weaker than the coupling of pulses with opposite circular polarization (Fig. 36). This is explained by noting that the sum of two corotating circular polarizations is itself circular; a circular polarization allows only weak molecular alignment (Ref. 33). However, the sum of two counter-rotating circular polarizations has a linear component which can induce significant molecular reorientation.

The results of most of these experimental configurations discussed are summarized in Table 1.



a) two identical (Pump intensity = Probe Intensity) pulses with counterrotating circular polarizations.



b) two identical pulses with corotating circular polarizations.

Figure 36. Change in probe transmission in a CS₂ sample as a function of relative probe delay. One can deduce that zero delay (temporal synchronization of the pump and probe) occurs at ~ 170 ps on the time axis.

Table I
Adjustable parameters of degenerate two-wave mixing

| Polarizations Parameter | Linear and Parallel Pump and Probe | Circular Pump / Linear Probe | | Circular Pump / Circular Probe | |
|---|--|---|--|--|-------------------------------------|
| | | Monitor <i>Parallel</i> to incident Probe | Monitor <i>Perpendicular</i> to incident Probe | Co-Rotating polarizations | Counter-Rotating polarizations |
| Initial ratio of Pump/Probe Intensity <i>Increases</i> : | Probe gains exceed probe losses | Probe losses greater than probe gains | — | — | — |
| Intersection angle, α , of pump and probe <i>decreases</i> : | Probe losses typically exceed probe gains due to the influence of self diffraction losses. | — | — | Negligible Influence | losses to diffracted beams increase |
| <i>Increasing</i> laser intensities | Increase in coupling and energy transfer between pump and probe pulses | Probe intensity increases as the square of pump | — | Increase in coupling and energy transfer. Note that corotating coupling is \ll counterrotating coupling. | — |
| <i>Increasing</i> optical path length in nonlinear medium | Energy transfer in Carbon Disulfide showed a small increase with path length as optical path was increased from 1mm to 2mm to 5mm to 10mm | — | — | — | — |
| Variation of Pump-Probe Relative Delay: | As the pulses pass through the sample, probe <i>loses</i> energy if it leads pump; <i>gains</i> energy if it lags pump | Probe gain is approx. symmetric with delay. Loss not possible | — | Probe <i>gains</i> energy when it lags pump; <i>loses</i> energy when it leads pump. | — |
| Correlation btwn. pulse duration and material relaxation time | The nonlinear coupling which allows energy transfer is strongest when the relaxation time of the optical nonlinearity is comparable to the pulses length. For cases in which the nonlinear relaxation time is significantly smaller or larger than the pulse width, energy transfer is negligible. Response time for <i>excitation</i> of the optical nonlinearity must also be considered | | | | |

5.0 COMPARISON

5.1 LINEAR ABSORPTION SPECTRUM

The absorption of water-based gold colloids in a 2 mm cell was given by Figure 26. Two fitting parameters, $\epsilon_b = 11.6$ and $\nu = 0.09 \omega_p$, were used to interpret the linear absorption spectrum for gold particles. The two parameters appear in the resonant denominator, which is given in Appendix A (Equation A.2a), and calculated from the measured absorption coefficient at the surface plasma frequency both for water-based gold colloids and Schott PG-6 glass in Section 4.1.2. The theoretical absorption spectra for these two parameters are given in Figure 37. There is indeed a reasonable fit for the low energy wing of the absorption spectra, where the interband transition is not the dominant contribution.

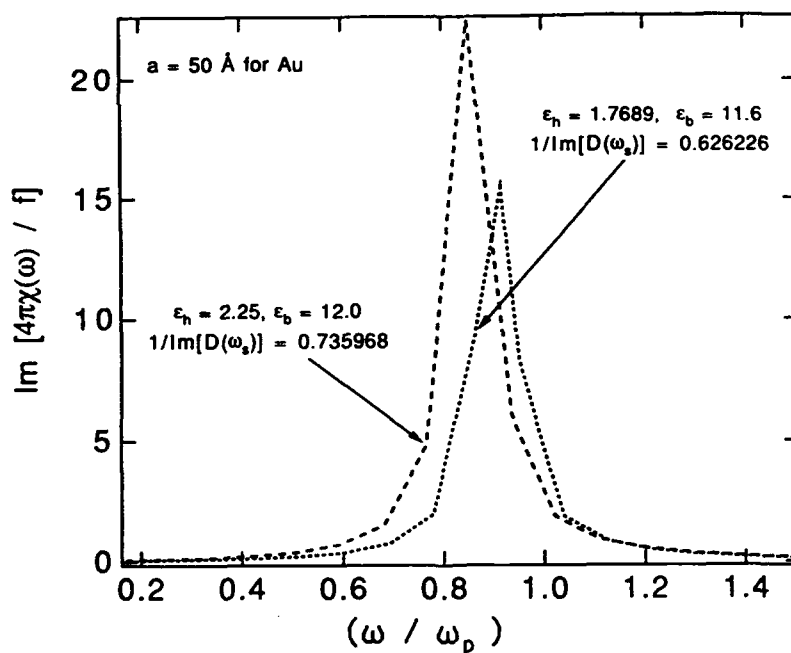


Figure 37. The linear absorption spectra of gold colloids within the quasi-hydrodynamic theory. The fitting parameters are $\epsilon_b = 11.6$ and $\nu = 0.09 \omega_p$.

5.2 PHASE CONJUGATION

Starting from one of the simplest equations for phase-conjugate reflectivity (R):

$$R \sim \tan^2(KL) \quad (77)$$

where K is defined as the nonlinear coupling coefficient (K is proportional to $\chi^{(3)}$ times the field intensity) and L is the interaction length, consider the low-conversion (low reflectivity) limit. In this region, the phase conjugation reflectivity is proportional to the square of K and the approximations for CS₂ and gold colloid samples can be equated, correcting for the reflectivity difference between the two and the actual volume fraction ($\sim 4 \times 10^{-6}$) for the gold colloid:

$$R_{\text{Au Colloid}} = R_{\text{CS}_2} \times 10^{-3} \quad (78a)$$

or

$$(K_{\text{Au}} L_{\text{eff}})^2 = (K_{\text{CS}_2} L)^2 \times 10^{-3} \text{ where } L_{\text{eff}} = (4 \times 10^{-6})L \quad (78b)$$

After the substitutions:

$$K_{\text{Au}} = (1.6 \times 10^{-8})^{-1/2} K_{\text{CS}_2} \quad (79)$$

or equivalent, that the $\chi^{(3)}$ of the gold particle is $\sim 10^4$ times that of CS₂, which is about 10^{-8} esu. The phase conjugation reflectivity of the matrix is insignificant at low intensities, but becomes comparable to that of the particles at higher intensities because of a saturation of the nonlinear susceptibilities of the particles. Thus the suspension may be "tailored" to vary the total optical nonlinearity in the sample.

Using the parameters of CW absorption and picosecond optical phase conjugation measurements the linear and nonlinear properties of gold colloidal suspensions were studied. The theoretical values of $\chi^{(3)}$ for the gold spheres can be obtained from Equation 49 (page 46) using the fitting parameters for CW absorption in Section 5.1, and is on the order of 10^{-10} esu. This is much too low compared to the experimental value.

This indicates that the free electron contribution which is accounted for in the model is not the main nonlinear mechanism in the gold microparticle composites.

5.3 COHERENT TWO-WAVE MIXING

5.3.1 Transient Coherent Two-Wave Mixing in Kerr Medium

Recently there has been considerable interest in coherent beam combination via two-wave mixing in nonlinear media due to its potential applications to optical signal processing and high energy laser physics (Ref. 34). This process proceeds as follows: two laser beams, a pump and a probe wave, enter a nonlinear medium and induce an optical index grating. If the phase of this grating lags that of the interference field pattern formed by the two incident laser beams I and II, energy will be coherently diffracted from beam I to beam II. The diffracted beam I acquires the phase, frequency and propagation vector of beam II.

To date, most research on coherent beam combination via two-wave mixing has focused on photorefractive crystals (Ref. 35) using degenerate CW beams, where a phase lag arises due to spatial nonlocality. Many of the details of this process can be influenced by varying the orientation of the crystal relative to the laser beams. Another scheme for creating a phase lag between the laser interference pattern and the light induced index grating is to utilize nondegenerate beams in optical Kerr media or other $\chi^{(3)}$ materials with finite response time (Ref. 36). For this case, energy is coherently transferred from the high-frequency beam to the low frequency one and the gain is a maximum for $\Omega\tau = 1$. Here Ω is the difference in laser frequencies and τ is the medium response time. Finally, nonlinear instantaneous Kerr film coated on a metallic substrate such as gold or silver can transfer energy between surface polaritons and laser beams (Ref. 37).

The role of beam polarization on transient, degenerate beam combination via two-wave mixing in CS_2 utilizing Gaussian laser pulses whose pulsewidth, τ_p , is not too much greater than τ was examined. For this situation, the finite response time of the medium and the width of the laser pulses are responsible for the appearance of the required phase lag. Since this is a transient phenomenon dependent upon temporal non-locality, the energy transferred from one beam to the other will intimately reflect the time-dependent characteristics of the system. Prior research has focused on beams that are linearly polarized in the same direction (Ref. 38).

In the two-wave mixing, beam combination experiments a pulsed Nd:Yag laser operating at 4 Hz was used. The laser system consisted of a passively mode-locked oscillator that provided ~ 20-ps pulses at 532 nm with ~ 1 mJ. In all cases, the beam diameter was 2 mm and the transverse profile was essentially Gaussian. The pulse is split into two components, corresponding to the pump and probe waves with the final intensity ratio equal to 10. A delay stage in the pump beam path controlled the relative arrival times between the pump and probe pulses in the sample. The angle between the pump and probe wavevectors was 4.5°, and the optical path length was 5 mm. The polarization dependence of the coupling between the two beams was examined using a configuration consisting of a right-circularly polarized pump pulse and a linearly polarized probe pulse. The pump reference and polarization discriminated transmitted probe energies were measured by pyroelectric energy meters as a function of their relative arrival times. The Kerr medium was CS₂ which has a characteristic response time of 1 to 2 ps.

Experimentally, it was observed that the coherent signal due to energy transfer was asymmetric with respect to probe delay time for the case where the output polarization was parallel to the input probe polarization. When the pump pulse arrived in the sample slightly after the probe pulse, i.e., delay time $\tau_D < 0$, there was a net energy transfer from the probe into the pump. This energy transfer was on the order of 20 percent of the initial probe energy. When the probe arrived in the sample slightly after the pump pulse, i.e., $\tau_D > 0$, it gained a small fraction of its initial energy. Energy transfer to the probe beam in the orthogonal polarization direction was also measured. In this case, the energy transfer curve was symmetrical with respect to the pulse delay time and achieved a maximum value of about 25 percent.

Next, a theory is presented for coherent beam combination via transient two-wave mixing in optical Kerr media with degenerate laser pulses. The transient dynamics of most Kerr media are reasonably well described by the Debye relaxation model. The laser beams are governed by the wave equation

$$\left[\nabla^2 - \frac{n^2}{c^2} \frac{\partial^2}{\partial t^2} \right] E(r,t) = \frac{1}{c^2} \frac{\partial^2}{\partial t^2} P_{NL}(r,t) \quad (80)$$

where $P_{NL}(r,t)$ is the nonlinear polarization and n is the linear refractive index. Since the dynamics of the nonlinear polarization are governed by Debye relaxation, the ℓ th component of the nonlinear polarization is given by

$$P_{NL}^{\ell}(r,t) = E_j(r,t) \int_{-\infty}^t dt' \frac{d_{\ell jki}}{\tau} \exp\left[-\frac{(t-t')}{\tau}\right] E_k(r,t') E_i(r,t') \quad (81)$$

where $d_{\ell jki}$ is the ℓjki th component of the third-order optical susceptibility tensor.

First the parallel polarization case, in which the pump is circularly polarized and the probe wave is linearly polarized in the x-direction is considered. They are nearly colinear and propagate in the z-direction. The energy of the transmitted probe polarized in the x-direction is measured. If the pump is not significantly depleted, polarization changes in both beams may be neglected so that the electrodynamics of beam combination involves independent quantities: the pump (probe) intensity I_1 (I_2) and the phase difference $\phi = \phi_1 - \phi_2$. The phase difference between the two pulses is driven by their nonlinear interaction with one another through their coupling to the Kerr medium. Within the slowly-varying envelope approximation

$$L I_1(z,t) = -2^{3/2}(\pi\omega/nc)d [I_1 I_2]^{1/2} F^{\ell}(z,t) \quad (82a)$$

$$L I_2(z,t) = +2^{3/2}(\pi\omega/nc)d [I_1 I_2]^{1/2} F^{\ell}(z,t) \quad (82b)$$

$$L \phi(z,t) = 2^{3/2}(\pi\omega/nc)d [1/I_1 - 1/I_2] (I_1 I_2)^{1/2} F^{\pi}(z,t) \quad (82c)$$

where $L = (\partial/\partial z + (n/c)\partial/\partial t)$ and $d \equiv d_{xxxx}$ is real. Equations 82a through 82c describe energy transfer processes involving the x-component of the probe wave. The coherent-coupling grating term $F(z,t) = F^{\ell}(z,t) + iF^{\pi}(z,t)$ is defined by

$$F(z,t) = \frac{1}{\tau} \int_{-\infty}^t dt' [I_1(z,t') I_2(z,t')]^{1/2} \exp\{i(\phi(z,t') - \phi(z,t)) - \frac{t-t'}{\tau}\} \quad (83)$$

which gives rise to coherent energy transfer between the beams. The quantity, $\phi(z, t') - \phi(z, t) + i(t - t')/\tau$ is driving the phase difference between the laser interference pattern and the index grating created within the nonlinear medium by the laser beams themselves. For steady-state situations, ϕ is independent of time, and energy transfer will proceed only if the laser beams are nondegenerate. However, for transient situations ϕ is time-dependent, and a transient phase lag will develop between the index grating and the laser interference pattern due to the finite response time τ of the medium. Note that the $L\phi$ depends upon $(I_1 - I_2)$, so that locally the direction of energy transfer will depend upon the relative beam intensities.

The laser beams are modeled as Gaussian pulses, with a delay time τ_D between them and identical pulse widths $\tau_p = 10\tau$. Numerically solving Equations 82 and 83 yields the transmitted pulse energy of the pump and probe waves. Figure 38 compares theory to experiment for the fractional change in energy of the probe versus pulse delay time. The solid line is theory, the diamonds are experimental data points with error bars included, where laser fluctuations were the dominant contribution to experimental error. An examination of this figure reveals that theory and experiment are in excellent agreement, with theory predicting the positions of the main features correctly: e.g., the zero crossing and the maximum fractional energy transfer and are in good overall quantitative agreement. The greatest discrepancy occurs when the energy transfer is small between the probe and the pump.

The physical content of these results can be stated as follows. If the pump wave enters the medium before the probe and the time delay between them is long compared to the medium response time, their overlap is insignificant and the induced index grating is negligible. As the pulse delay decreases, the beam overlap grows and the index grating they generate becomes substantial. If the pulse width is not too long compared to the medium response time, the phase difference does not approach steady-state and the phase lag between the index grating and the laser interference pattern is significant. This manifests itself in the form of increased energy transfer. This trend continues, until the two beam phases are the same over most of the overlap region. Although the index grating becomes deeper, the phase difference is only weakly driven by the nonlinear coupling and the phase lag begins to decrease. This behavior is in accordance with Equations 82a, b, and c and manifests itself as a reduction in energy transferred from one beam to the other. Eventually, the pulse delay reaches a point in

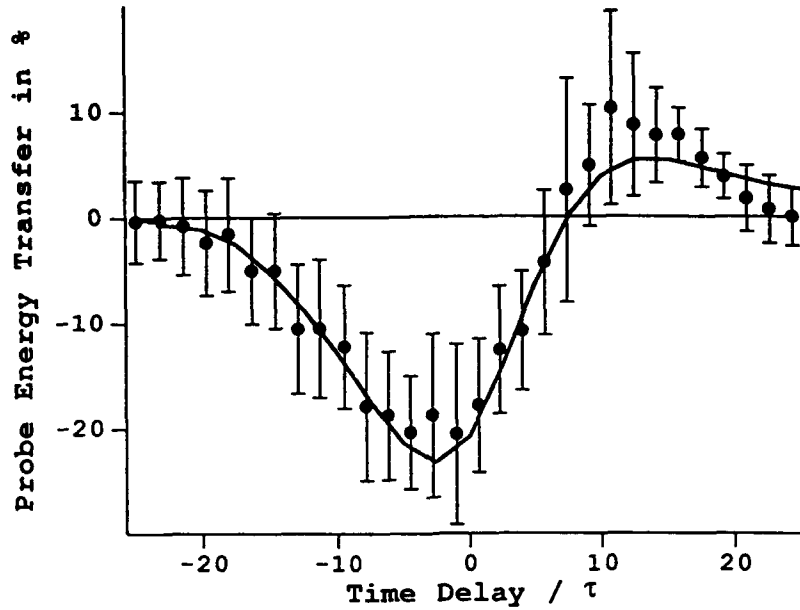


Figure 38. Percentage of energy transfer versus pulse delay in CS_2 for a pump/probe intensity ratio of 10, an optical path length of 5 mm and parallel polarization. The initial pump intensity was 1 GW/cm^2 , $d = 8 \times 10^{-16} \text{ cm}^2/\text{GW}$ and $\tau_p = 20 \text{ ps}$. The diamonds are experimental data points with error bars and the curve is theory.

which no energy is transferred. Once the probe beam leads the pump, the situation reverses itself, the phase lag changes sign and energy flows from the probe to the pump wave. This trend continues for increasing time delays until a point is reached in which the beam overlap is once again too weak to induce a meaningful index grating and energy is no longer diffracted from the probe wave to the pump.

Next, the cross-polarization case with a right-circularly polarized pump wave, a linearly polarized probe beam initially in the x-direction and energy transfer in the y-direction of the probe is measured. Again changes in pump polarization are neglected. The dominant grating arises from the coupling between the pump beam and the x-component of the probe wave which, through medium nonlinear anisotropy, twists the polarization of the diffracted beam into the y-direction. Denoting the y(x) component of the probe intensity by I_{2y} (I_{2x})

$$L I_1(z,t) = -2^{3/2}(\pi\omega/nc) d/6[I_1 I_{2x}]^{1/2} F(z,t) \quad (84a)$$

$$L I_{2y}(z,t) = +2^{3/2}(\pi\omega/nc) (d/6[I_1 I_{2x}]^{1/2} F^y(z,t)) \quad (84b)$$

$$L \phi(z,t) = 2^{3/2}(\pi\omega/nc)[I_1 I_{2x}]^{1/2} d[F^x(z,t))/6I_1 + F^y(z,t)/2i_{2x}] \quad (84c)$$

where off-diagonal components of d_{ijk} are related to the diagonal ones and F is given by Equation 83. Note that the phase difference does not depend on the relative intensities of the pump and probe waves so that energy is always transferred to the y-component of the probe beam. The numerical results are shown in Figure 39. For this case, the phase lag will not reverse sign and energy transfer is symmetric with respect to $\tau_D = 0$. As the delay time between the probe and pump increases, the index grating decreases with a corresponding reduction in energy transfer.

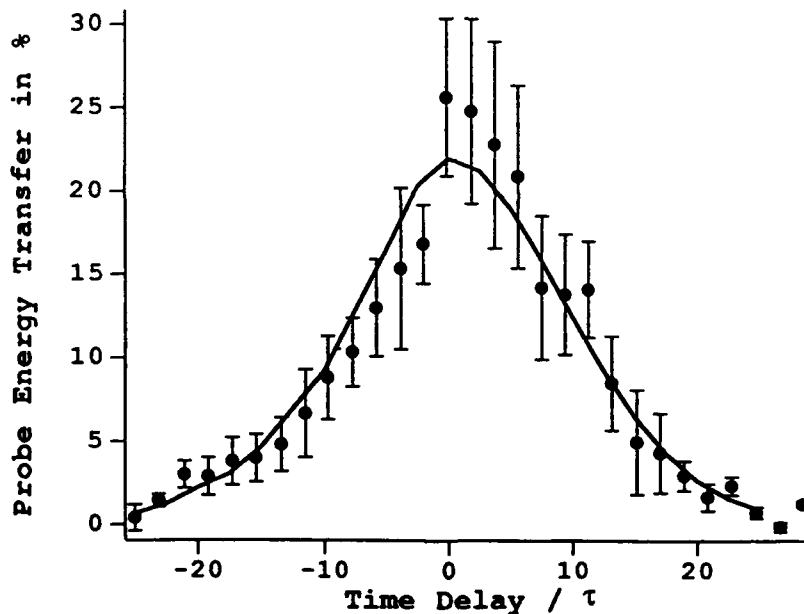


Figure 39. Percentage of energy transfer versus pulse delay in CS_2 for a pump/probe intensity ratio of 10, an optical path length of 5 mm and cross polarization. The initial pump intensity was 1 GW/cm^2 , $d = 8 \times 10^{-16} \text{ cm}^2/\text{GW}$ and $\tau_D = 20 \text{ ps}$. The diamonds are experimental data points with error bars and the curve is theory.

An examination of these figures reveals that theory and experiment are in excellent agreement for all but the shortest pulse delay times. For the smallest pulse delay times, the index grating involving the y-component of the probe beam is significant and since Equations 84a, b, and c ignore this effect, they underestimate the energy

transferred. Note that although the fractional energy transfer approaches 25 percent, pump depletion is still negligible and therefore the pump polarization remains essentially circular.

The temporal pulse shapes at output are Gaussian for Gaussian input pulses with pulse widths being 10τ . Frequency chirp is negligible for the optical path lengths used.

To summarize: polarization resolved coherent two-wave mixing experiments have been performed using degenerate, frequency-doubled Nd:Yag picosecond laser pulses in CS_2 , with a circularly polarized pump and a linearly polarized probe wave. Theoretical predictions are in excellent agreement with the measurements, and the important role of beam polarization in this process can be seen clearly by comparing the parallel-polarized and cross-polarized cases.

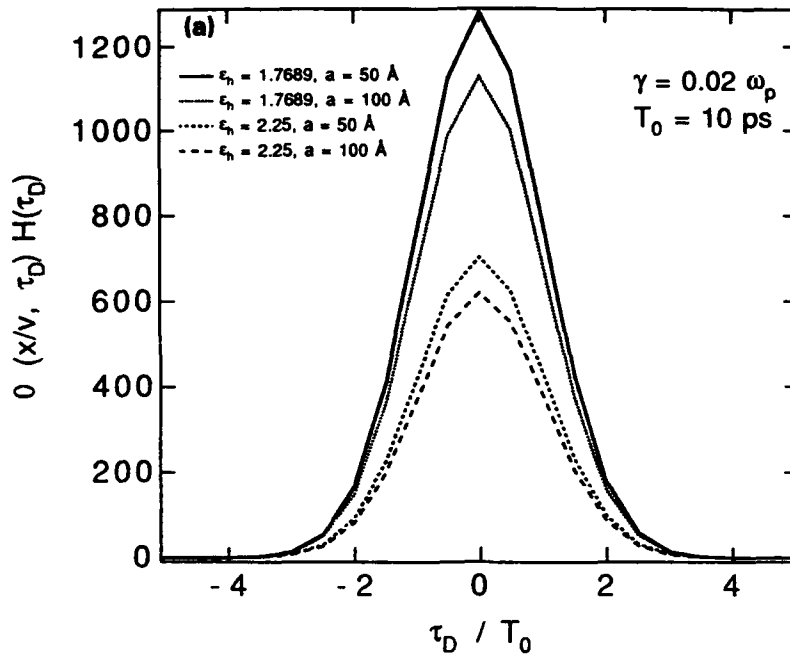
5.3.2 Transient Coherent Two-Wave Mixing in Metallic Colloids (Gold and Silver)

As a comparison to the Kerr medium discussed in Section 5.3.1, the coherent part of the third-order polarization for probe wave at ω_2 in a Kerr medium is worked out with the Debye relaxation time characteristics and is given by

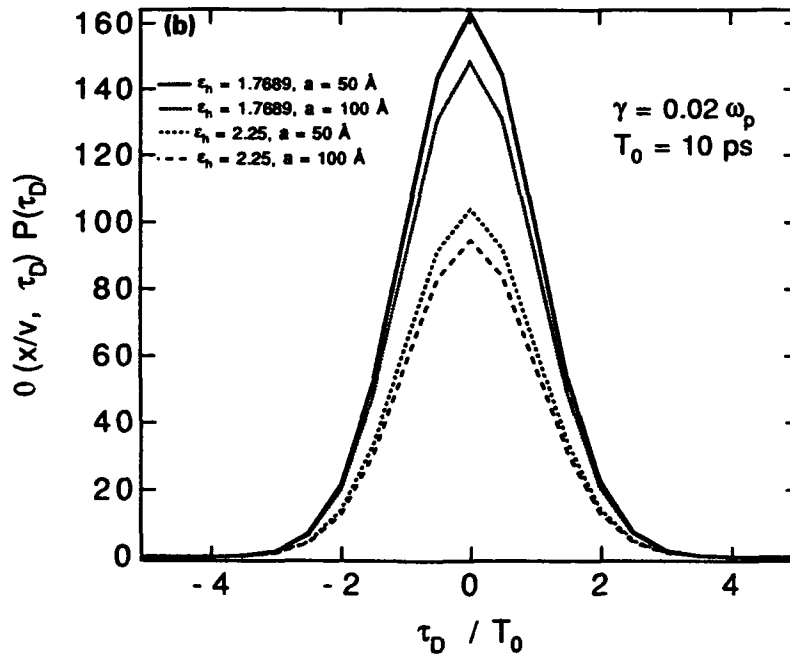
$$P_{\ell}^{(3C)}(t) = \frac{d_{\ell j k i}}{\tau} e^{-i\omega_2 t} \frac{4\sqrt{2\pi} I_1}{C T_2} \left(\frac{\sqrt{2\pi} I_2}{C T_2} \right)^{1/2} O(t, \tau_D) P(T_e/\tau) \quad (85)$$

where the overlap function $O(t, \tau_D)$ and the dimensionless polarization prefactor $P(T_e/\tau)$ are given by Equations 68b and 68d. In Equation 85, both input pulses are taken to be Gaussian and are defined as in Equation 64: τ is the phenomenological relaxation time and τ_D is the probe delay time. Comparing Equations 85 and 67, the inhomogeneous part of the time-dependent third-order polarization for microparticle composites is the same as a Kerr medium with the Debye relaxation characteristics. The homogeneous part has additional time asymmetric factor resulting from the additional fourth field enhancement factor involved.

In Figures 40 through 42, the dimensionless time-dependent polarization prefactors are plotted as functions of the probe delay times. One can see the effective decay times are much shorter in the heavily damped spheres, viz. $\nu = 0.1 \omega_p$. When the decay time is much shorter than the pulse widths, the CW limit for shorter pulses takes

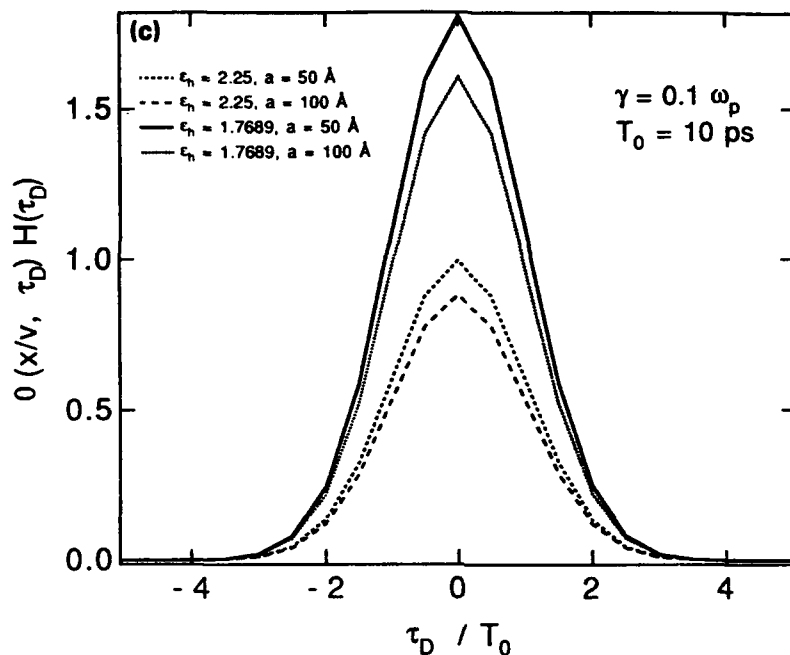


(a) The homogeneous part versus probe delay time, with $v = 0.02 \omega_p$.

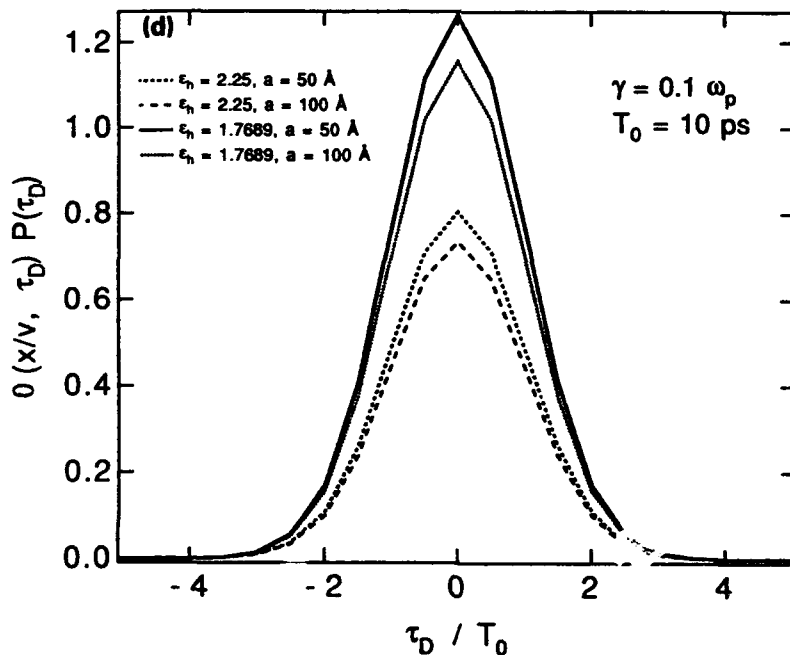


(b) the inhomogeneous part versus probe delay time, with $v = 0.02 \omega_p$.

Figure 40. The time-dependence prefactors versus probe delay time for silver colloids in water ($\epsilon_h = 1.7689$) and glass ($\epsilon_h = 2.25$) with radius of 50 Å or 100 Å, pulse widths 10 ps and $t = x/v$.

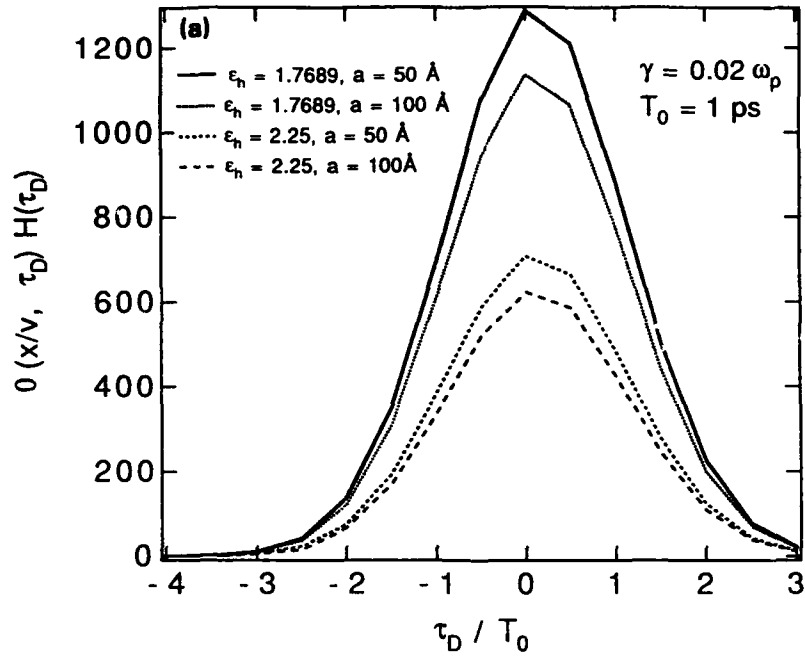


(c) the homogeneous part versus probe delay time, with $v = 0.1 \omega_p$.

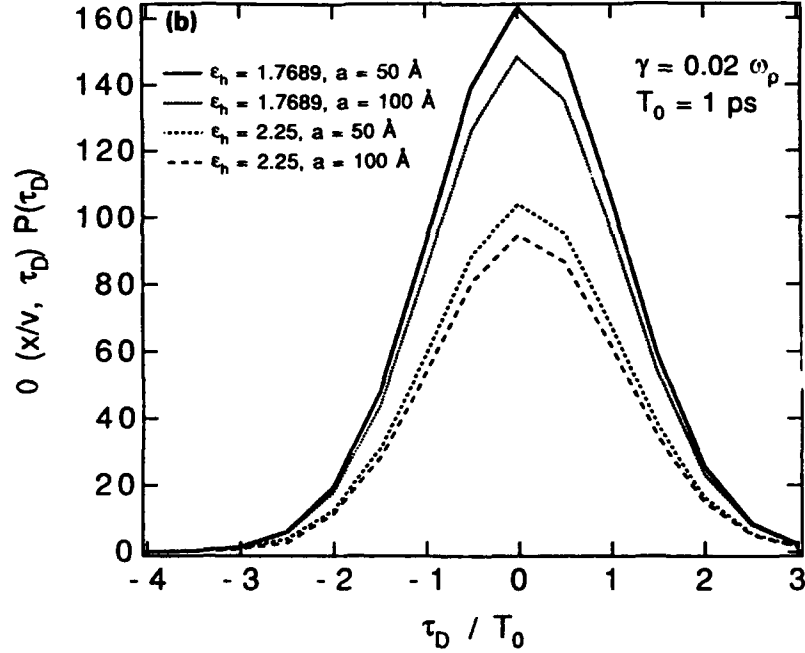


(d) the inhomogeneous part versus probe delay time, with $v = 0.1 \omega_p$.

Figure 40. (Concluded)

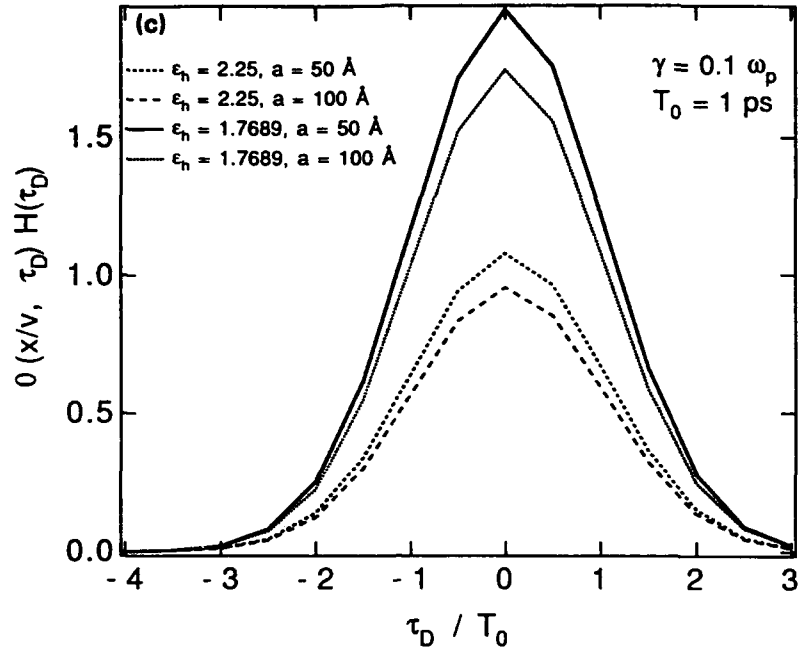


(a) The homogeneous part versus probe delay time, with $v = 0.02 \omega_p$.

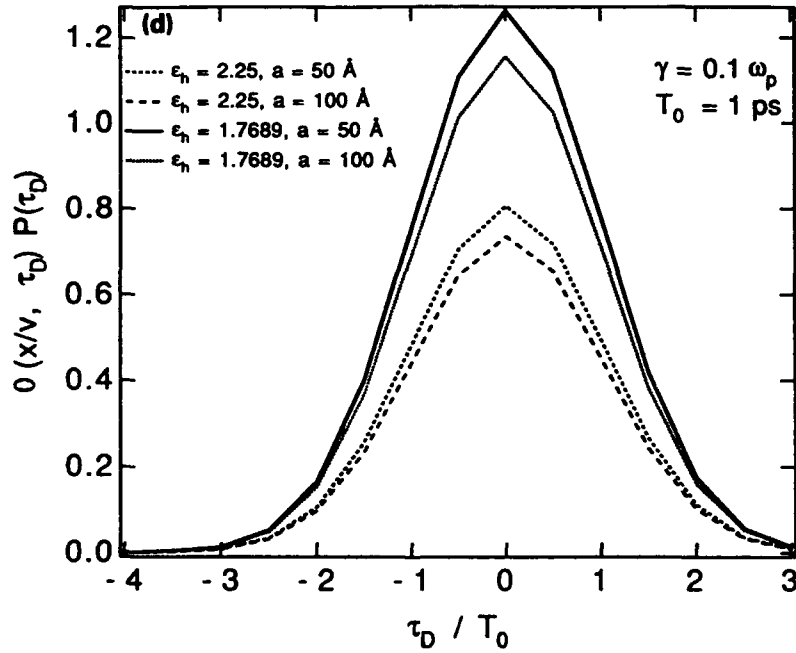


(b) the inhomogeneous part versus probe delay time, with $v = 0.02 \omega_p$.

Figure 41. The time-dependence prefactors versus probe delay time for silver colloids in water ($\epsilon_h = 1.7689$) and glass ($\epsilon_h = 2.25$) with radius of 50 Å or 100 Å, pulse widths 1 ps and $t = x/v$.

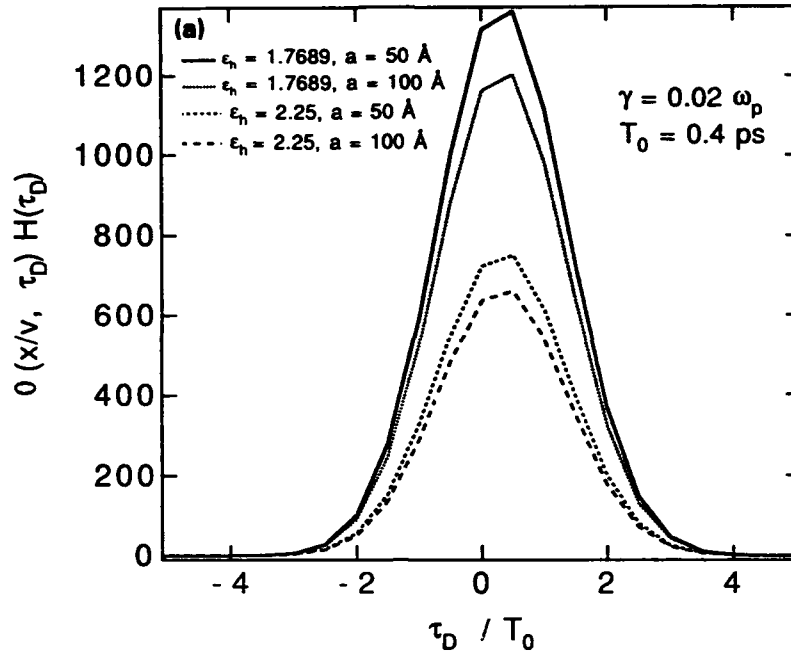


(c) the homogeneous part versus probe delay time, with $v = 0.1 \omega_p$.

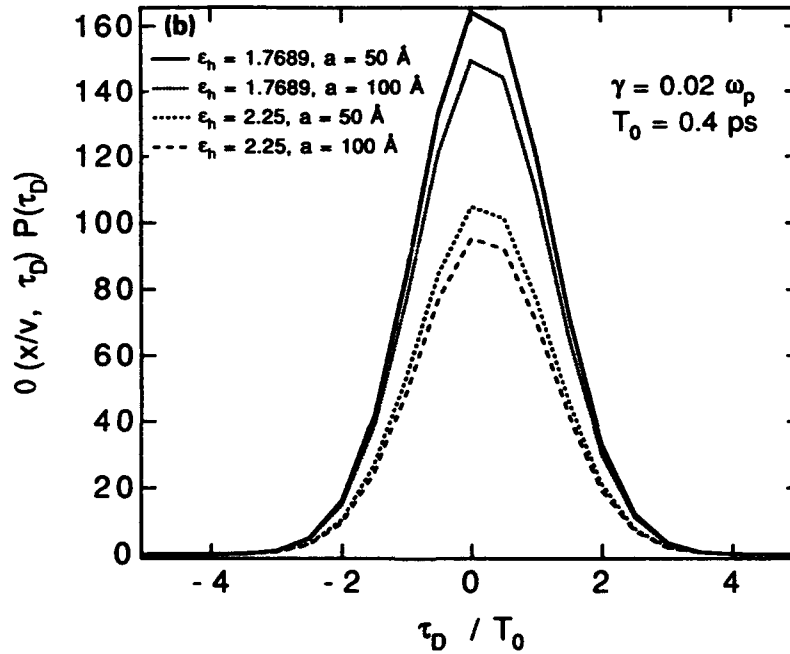


(d) the inhomogeneous part versus probe delay time, with $v = 0.1 \omega_p$.

Figure 41. (Concluded)

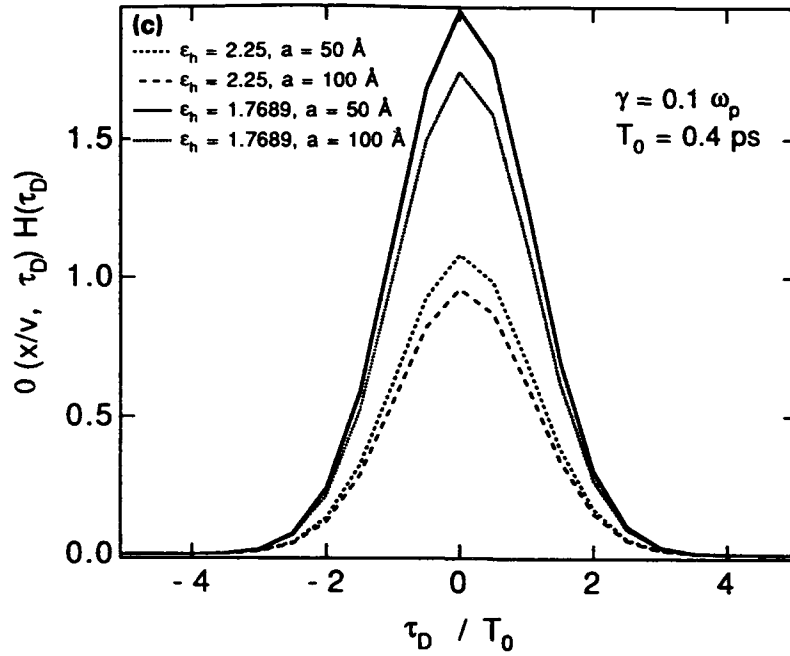


(a) The homogeneous part versus probe delay time, with $v = 0.02 \omega_p$.

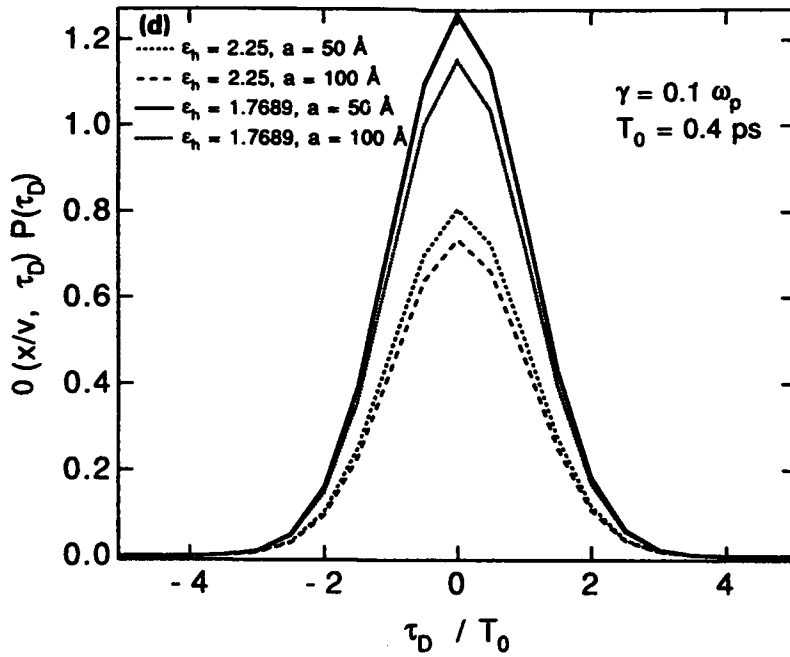


(b) the inhomogeneous part versus probe delay time, with $v = 0.02 \omega_p$.

Figure 42. The time-dependence prefactors versus probe delay time for silver colloids in water ($\epsilon_h = 1.7689$) and glass ($\epsilon_h = 2.25$) with radius of 50 Å or 100 Å, pulse widths 0.4 ps and $t = x/v$.



(c) the homogeneous part versus probe delay time, with $v = 0.1 \omega_p$.



(d) the inhomogeneous part versus probe delay time, with $v = 0.1 \omega_p$.

Figure 42. (Concluded)

effect and the time-dependent behaviors are solely determined by the overlap of the incident pulses. Note that there is more asymmetry in the homogeneous part than the inhomogeneous part.

The transient behavior for the metallic microparticle composites for the inhomogeneous (driven) third-order polarization is the same as the Kerr medium considered in Section 5.3.1, since they are driven by the nonlinear polarization with the same time-dependence, c.f. Equations 85 and 67. For the homogeneous contribution the additional time asymmetry will enhance the gain in the positive probe delay time. This was indeed observed in the transient two-wave mixing experiments in gold colloids (see Figure 30). Also all the homogeneous contributions are larger than the corresponding inhomogeneous counterparts. This is the reminiscence of the additional enhancement field factor in the homogeneous parts.

6.0 A ONE-DIMENSIONAL CONJUGATED POLYMER

6.1 ONE-DIMENSIONAL VIBRON-LATTICE MODEL

The conjugated polymers with π -electrons have been demonstrated to have high electrical conductivity and unusual nonlinear optical properties. The potential high speed (subpicoseconds) and large spectral range are very attractive for nonlinear optical processing. The nonlinearity associated with π -electrons is the nonresonant type, which provides the large spectral range. The π -electron response time is limited by the one-dimensional diffusion time, which is much shorter than the three-dimensional one and is on the order of subpicoseconds. The band gaps will be determined by the shortest wavelength in the applications.

Here we use a simple and tractable one-dimensional vibron model (Ref. 39) is used within the framework of lattice dynamics to describe conjugated polymers and were able to predict the values of off-resonant $\chi^{(3)}$ with reasonable accuracy.

Particular attention will be given to Polyacetylene (PA) which contains a high density of π -electrons and promises an ultrafast response time. It has been measured (Ref. 40) to have $\chi^{(3)} = 10^{-10}$ esu at off-resonance spanning from 1.17 eV to 1.5 eV with a 0.1 ps response time and have $\chi^{(3)} = 10^{-9}$ esu at the narrow two-photon resonance peak centered at 0.91 eV with a response time of a few ps.

The π -electrons of PA are modeled by vibrons with harmonic on-site potential and nearest neighbor interaction between them. The σ -backbone of PA, which is formed by CH groups, is modeled by a one-dimensional (1D) lattice within the harmonic lattice approximation. The interaction between the π -electrons and σ -backbone is also restricted to nearest neighbors. To be more specific, the model Hamiltonian of PA is chosen as follows:

$$H = H_{\pi} + H_{\sigma} + H_{int} + V_{ext} \quad (86)$$

In Equation 86, the Hamiltonian H_{π} for π -electrons (or vibrons) is given by

$$H_{\pi} = \frac{1}{2} m_e \sum_n \dot{q}_n^2 + \sum_n v(q_n) - \sum_{nm} L(n,m) q_m q_n \quad (87a)$$

where m_e and q_n are the mass, velocity and displacement of the n -th π -electrons. The on-site potential $v(q_n)$ for n -th vibron is assumed to be harmonic type and is given by

$$v(q_n) = \frac{1}{2} m_e \omega_0^2 q_n^2 \quad (87b)$$

where the eigen frequency ω_0 is closely related to the bandwidth W of the π -electron band structure. The interaction $L(n,m)$ among the π -electrons is reduced to

$$\sum_{nm} L(n,m) q_m q_n = L_0 \sum_n (q_{n+1} + q_{n-1}) q_n \quad (87c)$$

for the nearest neighbor interaction among them. The nearest neighbor interaction constant L_0 is related to the hopping integral t_0 in SSH Hamiltonian (Ref. 41), viz.

$$L_0 = \frac{m_e \omega_0}{h} t_0 \quad (88)$$

where $t_0 = 2.5$ eV for PA.

The Hamiltonian H_σ for σ -backbone (or 1-D lattice) is given by

$$H_\sigma = \frac{1}{2} M \sum_n U_n^2 + \frac{1}{2} K \sum_n (U_n - U_{n+1})^2 \quad (89)$$

where M , U_n and U_{n+1} are the mass, velocity and displacement of the n -th CH group (or the $n+1$ -th lattice site); and K is the effective spring constant of the 1-D lattice. The K is equal to 21 eV/Å (from Reference 41).

The interaction Hamiltonian H_{int} between the vibrons (π -electrons) and the lattice (σ -backbone) is given by

$$H_{int} = -\lambda \sum_n \{ (U_{n+1} - U_n) q_{n+1} + (U_n - U_{n-1}) q_{n-1} \} q_n \quad (90)$$

where the nearest neighbor interaction is assumed and the vibron-lattice coupling constant λ is related to the electron-phonon coupling constant α in SSH Hamiltonian (Ref. 41), viz.

$$\lambda = \frac{m_e \omega_0}{h} \alpha \quad (91)$$

where $\alpha = 4.1 \text{ eV/\AA}$ for PA.

The response V_{ext} to the external optical field is assumed to be electric-dipole interaction, viz.

$$V_{\text{ext}} = eq_n E \quad (92)$$

where E is the electric field of the external optical pulse.

From the model Hamiltonian, the equation of motion for PA is given by

$$\begin{aligned} m_e \ddot{q}_n + m_e \omega_0^2 q_n - 2L_0(q_{n+1} + q_{n-1}) \\ - 2\lambda [(U_{n+1} - U_n) q_{n+1} + (U_n - U_{n-1}) q_{n-1}] = -eE \end{aligned} \quad (93a)$$

$$M\ddot{U}_n + K(2U_n - U_{n+1} - U_{n-1}) + 2\lambda (q_{n+1} - q_{n-1}) q_n = 0 \quad (93b)$$

which are respectively for the π -electron and CH group at the n -th site. Since $M \gg m_e$ and hence $\dot{U}_n \ll \dot{q}_n$, adiabatic approximation can be used to reduce Equation 93b as follows.

$$K(2U_n - U_{n+1} - U_{n-1}) + 2\lambda (q_{n+1} - q_{n-1}) q_n = 0 \quad (94)$$

Equation 94 can be integrated and have

$$U_n - U_{n+1} = \frac{2\lambda}{K} (q_n + q_{n-1}) q_n + U_0 \quad (95)$$

where U_0 is an integration constant, and is equal to zero or 0.04 \AA for undimerized (unconjugated) or dimerized (conjugated) PA, respectively.

This model Hamiltonian can be employed to design and study other conjugated polymers.

6.2 THIRD-ORDER NONLINEAR SUSCEPTIBILITY

The equation of motion, Equation 93 within the adiabatic approximation for the third-order susceptibility of PA will be solved in this section.

Substituting Equation 95 into Equation 93a, the equation of motion for the n -th π -electron is obtained,

$$m_2 \ddot{q}_n + m_e \omega_0^2 q_n - 2(L_0 + \lambda U_0) (q_{n+1} + q_{n-1}) - \frac{4\lambda^2}{K} [(q_{n+1} + q_n) q_{n+1} + (q_n + q_{n-1}) q_{n-1}] = -eE \quad (96)$$

where $\frac{4\lambda^2}{K}$ is the effective nonlinear coefficient for the π -electrons, and this particular combination is the consequence of the electron-photon interaction.

Equation 96 can be used to solve for the linear and nonlinear response of the π -electrons in the presence of an optical field at ω , viz.

$$E = E_0 e^{-i\omega t} + \text{c.c.} \quad (97)$$

For a 1-D lattice, the linear displacement of the n -th π -electron can be written as

$$q_n = q_1 e^{i(kan - \omega t)} + \text{c.c.} \quad (98)$$

where a is the lattice spacing (or the spacing between CH group). The amplitude q_1 obeys the following linearized equation:

$$[m_e(\omega_0^2 - \omega^2) - 4(L_0 + \lambda U_0 - \cos ka)] q_1 = -eE_0 e^{-ikan} \quad (99a)$$

which yields

$$q_1 = -\frac{eE_0}{\Delta_1(\omega)} e^{-ikan} \quad (99b)$$

with the linear dispersion relation $\Delta_1(\omega)$ at ω is given by

$$\Delta_1(\omega) = m_e(\omega_0^2 - \omega^2) - 4(L_0 + \lambda U_0) \cos ka \quad (100)$$

The linear dipole moment at ω of a PA chain with N-sites is given by

$$p_1(\omega) = -e \sum_{n=1}^N q_1 e^{ikan} = \frac{Ne^2 E_0}{\Delta_1(\omega)} \quad (101a)$$

The corresponding polarization without local field correction is given by

$$P_1(\omega) = \frac{p_1(\omega)}{NaA} = x^{(1)}(\omega) E_0 \quad (101b)$$

where the linear susceptibility $x^{(1)}(\omega)$ along the chain is given by

$$x^{(1)}(\omega) = \frac{e^2}{aA\Delta_1(\omega)} \quad (102)$$

with A as the cross-section of the PA chain, and $A = 3.125 \times 10^{-15} \text{ cm}^2$.

The measured dielectric constants (Ref. 42) at 9.1 GHz for trans-PA are $\epsilon_{\parallel} = 5.7$ and $\epsilon_{\perp} = 4.0$, respectively. From Equation 102 and the measured ϵ_{\parallel}

$$\Delta_1(\omega = 0) = 1.62 \times 10^4 \text{ erg/cm}^2 \quad (103)$$

Equating Equations 100 and 103

$$\hbar\omega_0 = 11.91 \text{ eV} \quad (104)$$

which is comparable to the bandwidth $w = 10 - 12$ eV.

The static dispersion relation $\Delta_1(\omega = 0)$ is also related to the energy gap of the π -electrons, viz.

$$\Delta_1(\omega) = m_e \left(\frac{E_g}{h} \right)^2 \quad (105)$$

which yields $E_g = 2.78$ eV with Equation 103 and is comparable to the observed optical gap 2.0 to 2.2 eV.

The displacement of the 1-D lattice up to the third-order at ω can be written as

$$q_n = (q_1 + q_3) e^{i(kan - \omega t)} + \text{c.c.} \quad (106)$$

where q_1 and q_3 are the amplitudes of linear and nonlinear displacements. The nonlinear amplitude q_3 obeys the following equation,

$$\begin{aligned} [m_e(\omega_0^2 - \omega^2) - 4(L_0 + \lambda U_0) \cos ka] q_3 \\ = \frac{8\lambda^2}{K} (2 + 3 \cos ka + \cos 2ka) |q_1|^2 q_1 \end{aligned} \quad (107a)$$

where q_1 is given by Equation 99b. Then

$$q_3 = - \frac{8\lambda^2}{K} (2 + 3 \cos ka + \cos 2ka) \frac{e^3 |E_0|^2 E_0 e^{-i kan}}{|\Delta_1|^2 \Delta_1} \quad (107b)$$

Then the third-order nonlinear polarization at ω without local field correction is given by

$$P_3(\omega) = \chi^{(3)}(\omega) |E_0|^2 E_0 \quad (108)$$

where the third-order susceptibility along the chain is given by

$$\chi^{(3)}(\omega) = \frac{e^4}{aA} \frac{\lambda^2}{K} \frac{8(2+3 \cos ka + \cos 2ka)}{\Delta_1(\omega)^2 |\Delta_1(\omega)|^2} \quad (109)$$

In Equations 107 and 108, the condition of wavelength being long compared to the lattice spacing, i.e., $ka \ll 1$, can be used. In Equation 109 every parameter is fixed, and yields

$$\chi^{(3)}(\omega = 0) = 3.04 \times 10^{-10} \text{ esu} \quad (110a)$$

$$\chi^{(3)}(\hbar\omega = 1 \text{ eV}) = 5.3 \times 10^{-10} \text{ esu} \quad (110b)$$

$$\chi^{(3)}(\hbar\omega = 1.5 \text{ eV}) = 1.2 \times 10^{-9} \text{ esu} \quad (110c)$$

which is in reasonable agreement with the measured values $\chi^{(3)} = 10^{-10}$ esu spanning 1.17 eV to 1.5 eV.

This model can be extended to include the coulomb interaction and to study other conjugated polymers.

7.0 CONCLUSIONS

This report reviews theoretical and experimental research into the active nonlinear optical processes primarily in the microparticle composites and also in conjugated polymers.

The experimental studies done at the University of California at Irvine focused on the transient effects in the phase conjugation and coherent beam combination (or coherent two-wave mixing) using picosecond pulses. Beside the time-resolved experiments, the polarization resolved experiments were performed to demonstrate the coherent coupling nature in the two-wave mixing processes.

The theoretical studies emphasized the physical mechanisms for the nonlinear properties of the metallic microparticle composites and the conjugated polymers. The modeling of the nonlinear optical processes, viz. the phase conjugation and coherent beam combination, was carried out for the Kerr media and the metallic microparticle composites. The theory for the transient effects of the Kerr medium and the microparticle composites is discussed using either the time-dependent third-order polarization appearing in the Maxwell's equations or by solving the Maxwell's equations and the dynamic equation of the medium simultaneously. The additional asymmetry observed with respect to the probe delay time in the two-wave mixing experiments for microparticle composites is predicted in the calculated time-dependent third-order polarization.

In the past much attention has been paid to the study of linear optical properties of small metallic particles. The mechanisms of the surface plasma resonance and of the broadening of the linear absorption band in small spherical particles have been widely investigated. The calculation for the linear optical properties was first performed assuming independent electrons in the local approximation and improvements were then brought by introducing the nonlocal character of the response of electrons. Recently, the nonlinear optical phenomena present in such particles have been studied using optical phase conjugation in metallic colloids. The surface plasma resonance occurs for this nonlinear process in the same way as for linear properties.

A solid-state nonlocal continuum theory has been developed for the nonlinear electrodynamics of the microparticle composites. The calculation of the Kerr-type polarizability for the free electron part of small metallic spheres using the quasi-hydrodynamic theory has been done in this report. It is understood that some approximations have to be introduced in order to perform tractable analytical calculation. The quasi-hydrodynamic theory which includes the possibility of single particle-collective mode interactions is a simpler alternative to a classical kinetic theory or a quantum self-consistent field approach. However, the interband transition contribution of the microspheres by a frequency-independent background dielectric function ϵ_b to renormalize the free electrons has been taken into account. The free path effect approximation is used for the surface-scattering-contributed additional damping inside the microparticles. Silver spheres can be described accurately by this model. That is, the calculated third-order susceptibility from dressed free electrons and the measured third-order susceptibility are comparable in silver spheres, which are both 10^{-9} esu. Gold spheres can be explained by this model with two fitting parameters, i.e., the background dielectric constant and the damping factor, for their free electron contribution. However, the calculated third-order susceptibility from free electrons in gold spheres is much too small compared to the measured one, which indicates the important interband contribution in the optical nonlinearity for gold.

A semi-classical lattice-dynamic theory was derived to predict the large non-resonant optical nonlinearity below the band gap for 1-D conjugated polymers. The characteristic electron-photon interaction driven electronic nonlinearity is clearly identified in the formalism of the Kerr-type polarizability calculation for conjugated polymers.

The theoretical studies concentrated on the electronic nonlinearity of the microparticle composites which is caused by free (or conduction) electrons. This nonlinearity was also the focus of the short (picosecond) pulse experiments. The findings will have applications in high bit-rate transmission and communications.

The electronic nonlinearity involved in the microparticle composites is a resonant type, which results from the local field enhancement of the excited surface plasma modes and always is accompanied by an enhanced linear absorption for lossy materials. Since it is a resonant nonlinearity, there is limited spectral range for the

nonlinearity, which is 0.05 μm or 0.1 μm for silver or gold particles. Because of the enhancement in the linear absorption, the nonlinear efficiency must be optimized with some compromise in the absorption loss, which can be achieved by the small volume fractions or thin samples. The optimal thicknesses of the samples are a few millimeters. Small volume fraction is also needed to eliminate the unwanted scattering loss, which has to be less than 10^{-4} . Because of the potential excessive Mie scattering from large particles, the particle size below 100 \AA must also be restricted.

In the experimental studies, the microparticle composites were used for picosecond phase conjugation as well as weak probe signal amplification. The time-resolved and/or polarization resolved degenerate phase conjugation and two-wave mixing experiments were performed in the microparticle composites with a volume fraction between 4×10^{-6} and 10^{-5} with particle radii $< 120 \text{\AA}$. The degradation of the conjugated or amplified images from the scattering by particles is negligible with aforementioned limits of the sizes and volume fractions. However, the absorption from the particles is influential under all circumstances, which limits the sample thicknesses to 1 to 2 mm.

The relaxation time of the free (or conduction) electron part of electronic nonlinearity in the metallic microparticle composites is on the order of tens of femtoseconds according to the quasi-hydrodynamic theory. However, in the case of the gold the bound (or valence) electron contributed electronic nonlinearity contributed by the interband transition will have much longer relaxation time. For the two-wave mixing experiments the relaxation time was on the order of tens of picoseconds.

The conjugated polymers, which have nonresonant nonlinearity below the band gap with potential subpicosecond relaxation time because of fast one-dimensional diffusion characteristics were also investigated. Because the nonlinearity is a nonresonant type, the spectral range of the conjugated polymer is large. However, there is the shortest wavelength limit in the nonlinear conjugated polymer applications, which is set by the band gap. The limits on the band gap of the polymers can be easily tailored by the chemical engineering, e.g., by doping or using a different backbone element. The PAs, considered here to have a band gap of 2 eV, are suitable for IR applications. The polysilanes and polygermanes have band gaps in the UV region and can be useful for all visible applications.

REFERENCES

1. Kielich, S., "Linear and nonlinear light scattering in colloidal media," J. Colloid and Interface Sci. 27, 432, 1968.
2. Hache, F., Ricard, D., Flytzanis, C. Kreibig, U., "The optical Kerr effect in small metal particles and metal colloids: the case of gold," Appl. Phys. A47, 347, 1988.
3. Stroud, D., Hui,, P.M., "Nonlinear susceptibilities of granular matter," Phys. Rev. B37, 8719, 1988.
4. Kleinman, L., "Improved Hydrodynamic Theory of Surface Plasmons," Phys. B7, 2288 (1973).
5. Sipe, J.E., So,, V.C.Y., Fukui, M., Stegeman, G.I., "Analysis of second-harmonic generation at metal surfaces," Phys. Rev. B21, 4389, 1980.
6. Fuchs, R., Kliewer, K.L., "Surface Plasmon in a Semi-infinite Free-electron Gas," Phys. Rev. B3, 2270, 1971.
7. Genzel, L., Martin, T.P., Kreibig, U., "Dielectric function and plasma resonances of small metal particles," Z. Physik B21, 339, 1975.
8. Chizmeshya, A., Zaramba, E., "Second-harmonic generation at metal surfaces using an extended Thomas-Fermi-von Weizsacker Theory," Phys. Rev. B37, 2805, 1988.
9. Hua, X.M., Gersten, J.I., "Theory of second-harmonic generation by small metal spheres," Phys. Rev. B33, 3756, 1986.
10. Bhatnagar, P.L., Gross, E.P., Krook, M., "A model for collision processes in gases I. Small amplitude processes in charged and neutral one-component systems," Phys. Rev. 94, 511, 1954.

11. Baynham, A.C., Boardman, A.D., Plasma Effects in Semiconductors: Helicon and Alfen Waves, Taylor and Francis LTD., N.Y., 1971.
12. Baudman, A.D., Rupp, R., "The boundary conditions between spatially dispersive media," Surface Science 112, 153, 1981; and M.H. Cohen, Phys. Rev. 126, 389, 1962.
13. Ishimaru, A., Wave Propagation and Scattering in Random Media, Vol. 2, Academic Press, New York, NY, 1978.
14. Kreibig, U., "Electronic properties of small silver particles: the optical constant and their temperature dependence," J. Phys. F4, 999, 1974.
15. Hache, F., Ricard, D., Flytzanis, C., "Optical nonlinearities of small metal particles: surface-mediated resonance and quantum size effects," JOSA B3, 1647, 1986.
16. Zel'dovich, B. Ya., Pilipetsky, N.F. Shkunov, V.V.: "Principles of Phase Conjugation", Springer Series in Optical Sciences, Vol. 42, Springer, Berlin, 1985.
17. Pepper, D.M., Yariv, A., "Optical phase conjugation using three-wave and four-wave mixing via elastic photon scattering in transparent media," in "Optical Phase Conjugation," ed. R.A. Fisher, pp 23, Pergamon, New York, 1983.
18. Marburger, J.H., Lam, J.F., "Nonlinear theory of degenerate four-wave mixing," Appl. Phys. Lett 34, 389, 1979.
19. Jian-quan, Y., Guosheng, Z., Siegman, A.E., "Large signal results for a degenerate four-wave mixing and phase conjugate resonators," Appl. Phys. B 30, 11, 1983.
20. Trebino, R., Siegman, A.E., "Phase-conjugate reflection at arbitrary angles using TEM₀₀ pump beams," Opt. Comm. 31, 1, 1980.

21. Bochove, E., "Theory of phase conjugation by degenerate four-wave mixing using spatially varying pump beams," J. Opt. Soc. Am. **73**, 1330, 1983.
22. Turkevich, J., Stevenson, P., Hillier, J., "A study of the nucleation and growth processes in the synthesis of colloidal gold," Faraday Disc. **11** 55, 1951.
23. Saltiel, S., VanWanterghem, B., Rentzepis, P.M., "Measurements of $\chi^{(3)}$ and phase shift in nonlinear media by means of phase conjugation interferometer," Optics Letters **14** (3) pp183-185, 1989.
24. Etchepare, J., Kenney-Wallace, G.A., Grillon, G., Migus, A., Chambaret, J.P., "Polarization and temporal selectivity of subpicosecond optical responses in CS₂," IEEE Jour. Quant. Elec. **QE-18**, pp 1826-1829, 1982.
25. Ho, P.P. and Alfano, R.R., "Optical Kerr effect in liquids," Phys. Rev. A **20**, 2170-2187, 1979.
26. Yao, S.S., Karaguleff, C., Gabel, A., Fortenberry, R., Seaton, C.T. and Stegeman, G.I., "Ultrafast carrier and grating lifetimes in semiconductor-doped glasses," Appl. Phys. Lett. **46**, pp 801-802, 1985.
27. Lushnikov, A.A. and Simonov, A.J., "Optical properties of gold particles," Z. Physik **270**, 17-24, 1974.
28. Dutton, T.E., VanWanterghem, B., Saltiel, S., Chestnoy, N., Rentzepis, P.M., Shen, T.P. and Rogovin, D., "Picosecond phase conjugate reflectivity of gold colloids by degenerate four-wave mixing," Jour. Phys. Chem **XX**, 1100-1105, 1990.
29. Hache, F., Ricard, D. and Flytzanis, C., "Optical nonlinearities of small metal particles: surface-mediated resonance and quantum size effects," J. Opt. Soc. Am. B **3**, 1647-1655, 1986.
30. Eichler, H.J., Günter, P. and Pohl, D.W., "Laser-Induced Dynamic Gratings," Springer-Verlag, Berlin, Heidelberg, 1986.

31. Nighan, W.L. Jr, Gong, T., Liou, L. and Fauchet, P.M., "Self-diffraction: a new method for characterization of ultrashort laser pulses," Optics Comm. **69**, pp 339-344, 1989.
32. Trebino, R., Gustafson, E.K. and Siegman, A.E., "Fourth-order partial-coherence effects in the formation of integrated-intensity gratings with pulsed light sources," J. Opt. Soc. Am. B **3**, pp 1295-1304, 1986.
33. Shen, Y.R., The Principles of Nonlinear Optics, John Wiley and Sons, New York, 1984.
34. McMichael, I., Yeh, P., Beckwith, P., "Nondegenerate two-wave mixing in ruby," Opt. Lett. **13**, 500, 1988.
35. Staebler, D., Amodei, J., "Coupled-wave analysis of holographic storage in LiNbO_3 ," J. Appl. Phys. **43**, 1042, 1972.
36. Anan'ev, Y., "Possibility of dynamic correction of wave fronts," Sov. J. Quantum Electron. **4**, 929, 1975.
37. Shen, T.P., Rogovin, D., "Coherent beam combination at interfaces via surface polariton effects," Phys. Rev. Lett. **61**, 951, 1988.
38. Palfrey, S.L., Heinz, T.F., "Coherent interactions in pump probe absorption measurements: the effect of phase gratings," JOSA **B2**, 674, 1985.
39. Takeno, S., "Vibron solitons and coherent polarization in an exactly tractable oscillator-lattice system," Prog. of Theoretical Physics **73**, 853, 1985.
40. Etemad, S., Baker, G.L., Jaye, D., Kajzar, F., Messor, J., "Linear and nonlinear optical properties of polyacetylene," SPIE **682**, 44, 1982.

41. Su, W.P., Schrieffer, J.R., Heeger, A.J., "Soliton excitations in polyacetylene," Phys. Rev. B 22, 2099, 1980.
42. Devreaux, F., Döry, I., Mihaly, L., Pekker, S., Janossy, A., Kertesz, M., "Anisotropy of the dielectric constant of polyacetylene," J. Polym. Sci. Polymer Physics edition, 19, 743, 1981.

APPENDIX A

To solve Equation 7a for a sphere, expand the electron density in the following series

$$n_1(r, \omega_j) = \sum A_{lm}(q_j a) i_l(q_j r) Y_{lm}(\theta, \phi) \quad (\text{A.1})$$

where a is the radius of the sphere and $i_n(z)$ is the n^{th} order modified spherical Bessel function of $q_j = q(\omega_j)$. In spherical coordinates $\mathbf{r} = (r, \theta, \phi)$ and $Y_{lm}(\theta, \phi)$ is the spherical harmonic of order (l, m) . Since the ω_1 laser beam is elliptically polarized, $n_1(r, \omega_1)$ consists of the $l = 1, m = \pm 1$ term. The ω_2 laser beam is linearly polarized in the $\mathbf{e}_2 = (\hat{x} \cos \theta_2 + \hat{z} \sin \theta_2)$ direction and $n_1(r, \omega_2)$ contains the $l = 1, m = \pm 1$ (see Fig. 1). Applying the boundary conditions at the surface yields the following solutions for the first-order electron density at the two laser frequencies

$$n_1(r, \omega_1) = \frac{\epsilon_b}{4\pi e a} N(r, \omega_1) A_1 (\eta \cos \theta + \sin \theta \sin \phi) / D_1(\omega_1) \quad (\text{A.2a})$$

$$n_1(r, \omega_2) = \frac{\epsilon_b}{4\pi e a} N(r, \omega_2) A_2 (\sin \theta_2 \cos \theta + \cos \theta_2 \sin \theta \cos \phi) / D_1(\omega_2) \quad (\text{A.2b})$$

The boundary conditions yield the following expression for $N(r, \omega_j)$

$$N(r, \omega_j) = 3\epsilon_h(\omega_j) q_j a i_1(q_j r) / \Omega_j i_1'(q_j a) \quad (\text{A.2c})$$

where $i_1'(z)$ implying the derivative with respect to z , and the denominator $D_1(\omega_j)$ is given by

$$D_1(\omega_j) = \epsilon_b (1 - 1/\Omega_j) + 2\epsilon_h(\omega_j) [1 - i_1(q_j a) / \Omega_j q_j a i_1'(q_j a)] \quad (\text{A.2d})$$

with $\Omega_j \equiv \omega_j(\omega_j + i\nu)/\omega_p^2$ and ν is assumed to be frequency independent. The real part of this important denominator vanishes at ω_s . This denominator dominates the electrodynamics of microparticle composites whenever the surface (or Frohlich) dipole mode is excited by $\omega_j = \omega_s$.

The first order electric field $E_1(r, \omega_j)$ is given by

$$E_{1r}(r, \omega_1) = \Sigma_r(r, \omega_1) A_1(\eta \cos \theta + \sin \theta \sin \phi) / D_1(\omega_1) \quad (\text{A.3a})$$

$$E_{1r}(r, \omega_2) = \Sigma_r(r, \omega_2) A_2(\sin \theta_2 \cos \theta + \cos \theta_2 \sin \theta \cos \phi) / D_1(\omega_2) \quad (\text{A.3b})$$

$$E_{1\theta}(r, \omega_1) = \Sigma_\theta(r, \omega_1) A_1(-\eta \sin \theta + \cos \theta \sin \phi) / D_1(\omega_1) \quad (\text{A.3c})$$

$$E_{1\theta}(r, \omega_2) = \Sigma_\theta(r, \omega_2) A_2(\cos \theta_2 \cos \theta \cos \phi - \sin \theta_2 \sin \theta) / D_1(\omega_2) \quad (\text{A.3d})$$

$$E_{1\phi}(r, \omega_1) = \Sigma_\phi(r, \omega_1) A_1 \cos \phi / D_1(\omega_1) \quad (\text{A.3e})$$

$$E_{1\phi}(r, \omega_2) = -\Sigma_\phi(r, \omega_2) A_2 \cos \theta_2 \sin \phi / D_1(\omega_2) \quad (\text{A.3f})$$

where

$$\Sigma_r(r, \omega_j) = 3\epsilon_h(\omega_j) [1 - t_1'(q_j r) / \alpha_j t_1'(q_j a)] \quad (\text{A.3g})$$

$$\Sigma_\theta(r, \omega_j) = 3\epsilon_h(\omega_j) [1 - t_1(q_j r) / \alpha_j q_j r t_1'(q_j a)] \quad (\text{A.3h})$$

The first order electron drift velocity $v_1(r, \omega_j)$ is

$$v_{1r}(r, \omega_1) = \tilde{\Sigma}_r(r, \omega_1) V_{10}(\eta \cos \theta + \sin \theta \sin \phi) / D_1(\omega_1) \quad (\text{A.4a})$$

$$v_{1r}(r, \omega_2) = \tilde{\epsilon}_r(r, \omega_2) V_{20} (\sin \theta_2 \cos \theta + \cos \theta_2 \sin \theta \cos \phi) / D_1(\omega_2) \quad (\text{A.4b})$$

$$v_{1\theta}(r, \omega_1) = \tilde{\epsilon}_\theta(r, \omega_1) V_{10} (-\sin \theta + \cos \theta \sin \phi) / D_1(\omega_1) \quad (\text{A.4c})$$

$$v_{1\theta}(r, \omega_2) = \tilde{\epsilon}_\theta(r, \omega_2) V_{20} (\cos \theta_2 \cos \theta \cos \phi - \sin \theta_2 \sin \theta) / D_1(\omega_2) \quad (\text{A.4d})$$

$$v_{1\phi}(r, \omega_1) = \tilde{\epsilon}_\theta(r, \omega_1) V_{10} \cos \phi / D_1(\omega_1) \quad (\text{A.4e})$$

$$v_{1\phi}(r, \omega_2) = -\tilde{\epsilon}_\theta(r, \omega_2) V_{20} \cos \theta_2 \sin \phi / D_1(\omega_2) \quad (\text{A.4f})$$

where $V_{j0} = -ieA_j/m(\omega_j + iv)$ and the various $\tilde{\epsilon}_\mu$ are defined as

$$\tilde{\epsilon}_r(r, \omega_j) = 3\epsilon_h(\omega_j) [1 - i'_1(q_j r) / i'_1(q_j a)] \quad (\text{A.4g})$$

$$\tilde{\epsilon}_\theta(r, \omega_j) = 3\epsilon_h(\omega_j) [1 - i_1(q_j r) / i'_1(q_j a) q_j r] \quad (\text{A.4h})$$

Outside the microparticle, the first-order electric field is dipolar in nature. In the near (static) zone, the electrostatic potential of a sphere is given by

$$\phi_1(r, \omega_1) = \left\{ -r + \frac{u^{(1)}(\omega_1)}{r^2} \right\} A_1 \theta_1 \quad (\text{A.5})$$

where the angular functions θ_i are given by

$$\theta_1 = \eta \cos \theta + \sin \theta \sin \phi \quad (\text{A.6a})$$

$$\theta_2 = \sin \theta_2 \cos \theta + \cos \theta_2 \sin \theta \sin \phi \quad (\text{A.6b})$$

In Equation A.5, the first-order dipole moment at ω_i is given by

$$u^{(1)}(\omega_i) = \frac{4\pi}{3} a^3 p^{(1)}(\omega_i) \quad (\text{A.7})$$

where a is the radius of the sphere and the first-order polarization is given by

$$p^{(1)}(\omega_i) = \frac{3}{4\pi} \left\{ \frac{\epsilon_b - \epsilon_h(\omega_i)}{\epsilon_b + 2\epsilon_h(\omega_i)} - \frac{3\epsilon_b \epsilon_h(\omega_i)}{\epsilon_b + 2\epsilon_h(\omega_i)} \frac{j_2(q_i a)}{a_i j_1'(q_i a) D_1(\omega_i)} \right\} \quad (\text{A.8})$$

APPENDIX B

First, the different components $S_{\nu}^{\pm}(r)$ of the driver term $S^{\pm}(r)$ in Equations 2.11 depend only weakly on frequency ω and do not reflect the surface mode resonances of the microparticles, and are defined below:

$$S_{r00}^{\pm}(r) = S_{r20}^{\pm}(r) - 3[\tilde{\epsilon}_{\theta}(r, \omega_1)\tilde{\epsilon}_r(r, \pm\omega_2) + \tilde{\epsilon}_{\theta}(r, \pm\omega_2)\tilde{\epsilon}_r(r, \omega_1)]L^{\pm}a/r \quad (B.1a)$$

$$\begin{aligned} S_{r20}^{\pm}(r) = & N_1(r, \omega_1)\epsilon_r(r, \pm\omega_2) + N_1(r, \pm\omega_2)\epsilon_r(r, \omega_1) \\ & + N_1(r, \omega_1)\tilde{\epsilon}_r(r, \pm\omega_2)\omega_1/(\pm\omega_2 + i\nu) \pm N_1(r, \pm\omega_2)\tilde{\epsilon}_r(r, \omega_1)\omega_2/(\omega_1 + i\nu) \\ & - L^{\pm}[\tilde{\epsilon}_r(r, \omega_1)\tilde{\epsilon}_r'(r, \pm\omega_2) - \tilde{\epsilon}_{\theta}(r, \omega_1)\tilde{\epsilon}_r(r, \pm\omega_2)a/r] \\ & - L^{\pm}[\tilde{\epsilon}_r(r, \pm\omega_2)\tilde{\epsilon}_r'(r, \omega_1) - \tilde{\epsilon}_{\theta}(r, \pm\omega_2)\tilde{\epsilon}_r(r, \omega_1)a/r] \\ & + 2/3(\beta/\omega_p a)^2[N_1(r, \omega_1)N_1'(r, \pm\omega_2) + N_1(r, \pm\omega_2)N_1'(r, \omega_1)] \end{aligned} \quad (B.1b)$$

$$S_{\theta20}^{\pm}(r) = S_{\phi21}^{\pm}(r) + 2L^{\pm}\frac{a}{r}\tilde{\epsilon}_{\theta}(r, \omega_1)\tilde{\epsilon}_{\theta}(r, \pm\omega_2) \quad (B.1c)$$

$$S_{\theta21-}^{\pm}(r) = \frac{4}{3}S_{\phi}(r, \omega_1, \pm\omega_2) - \frac{1}{3}S_{\phi}(r, \pm\omega_2, \omega_1) + L^{\pm}\frac{a}{r}\tilde{\epsilon}_{\theta}(r, \omega_1)\tilde{\epsilon}_{\theta}(r, \pm\omega_2) \quad (B.1d)$$

$$S_{\theta21+}^{\pm}(r) = -\frac{1}{3}S_{\phi}(r, \omega_1, \pm\omega_2) + \frac{4}{3}S_{\phi}(r, \pm\omega_2, \omega_1) + L^{\pm}\frac{a}{r}\tilde{\epsilon}_{\theta}(r, \omega_1)\tilde{\epsilon}_{\theta}(r, \pm\omega_2) \quad (B.1e)$$

$$S_{\theta 22}^{\pm}(r) = S_{\theta 20}^{\pm}(r) + 3L^{\pm} \frac{a}{r} \tilde{\epsilon}_{\theta}(r, \omega_1) \tilde{\epsilon}_{\theta}(r, \pm \omega_2) \quad (\text{B.1f})$$

$$S_{\phi 21}^{\pm}(r) = S_{\phi}(r, \omega_1, \pm \omega_2) + S_{\phi}(r, \pm \omega_2, \omega_1) \quad (\text{B.1g})$$

$$S_{\phi 22}^{\pm}(r) = \frac{7}{2} S_{\phi}(r, \omega_1 \pm \omega_2) - \frac{3}{2} S_{\phi}(r, \pm \omega_2, \omega_1) + 3L^{\pm} \frac{a}{r} \tilde{\epsilon}_{\theta}(r, \pm \omega_2) \quad (\text{B.1h})$$

and

$$\begin{aligned} S_{\phi}(r, \omega_1, \pm \omega_2) = & N_1(r, \omega_1) \Sigma_{\theta}(r, \pm \omega_2) + N_1(r, \omega_1) \tilde{\epsilon}_{\theta}(r, \pm \omega_2) \omega_1 / (\pm \omega_2 + i\nu) \\ & - \tilde{\epsilon}_r(r, \omega_1) \tilde{\epsilon}'_{\theta}(r, \pm \omega_2) L^{\pm} \\ & + 2/3 (\beta / \omega_p a)^2 N_1(r, \omega_1) N_2(r, \pm \omega_2) a / r \end{aligned} \quad (\text{B.1i})$$

where the dimensionless linear electron density $N_1(r, \omega_j)$ is given in Equation A.2c and the L^{\pm} function is defined by

$$L^{\pm} = \omega_p^2 [(\omega_1 + i\nu)(\pm \omega_2 + i\nu)]^{-1} \quad (\text{B.2a})$$

and the primed functions are defined as

$$F'(r, \omega_j) = a \partial F(r, \omega_j) / \partial r \quad (\text{B.2b})$$

Then, to solve Equations 2.8 for a sphere, expand $n_2(r, \omega_{\pm})$ in terms of spherical harmonics as $n_1(r, \omega_j)$.

$$n_2(r, \omega_{\pm}) = \sum B_{lm}(q_{\pm}a) i_l(q_{\pm}r) Y_{lm}(\theta, \phi) + \int dr' [G_S(q_{\pm}|r, r') \nabla \cdot S_{\pm}(r')] / \beta^2 \quad (\text{B.3a})$$

where the integral is an inhomogeneous term, the coefficients B_{lm} are determined by the boundary conditions. The Green's function $G_S(q_{\pm}|r, r')$ is given by

$$G_S(q_{\pm}|r, r') = q_{\pm} \sum i_l(q_{\pm}r_{<}) K_l(q_{\pm}r_{>}) Y_{lm}^*(\theta', \phi') Y_{lm}(\theta, \phi) \quad (\text{B.3b})$$

where * implies a complex conjugate. The sum and difference-frequency fields obey the Laplace equation

$$\nabla^2 \phi_2(r, \omega_{\pm}) = 0 \quad (\text{B.4a})$$

outside the microparticle, and the Poisson equation

$$\nabla^2 \phi_2(r, \omega_{\pm}) = 4\pi e n_2(r, \omega_{\pm}) / \epsilon_b \quad (\text{B.4b})$$

within it. Equations B.2 will be solved by expanding in spherical harmonics. Thus, outside the sphere,

$$\phi_2(r, \omega_{\pm}) = \sum C_{lm}(q_{\pm} a) r^{-(l+1)} Y_{lm}(\theta, \phi) \quad (B.5a)$$

The electrostatic potential inside the microparticle is driven by the second-order charge density, $n_2(r, \omega_{\pm})$. Thus, within this region, the second-order electrostatic potential is written as

$$\phi_2(r, \omega_{\pm}) = \sum D_{lm}(q_{\pm} a) r^l Y_{lm}(\theta, \phi) - (4\pi e / \epsilon_b) \int dr' G_0(r, r') n_2(r', \omega_{\pm}) \quad (B.5b)$$

where $G_0(r, r')$ is the Green's function for the Laplace equation. The coefficients for the various multipole fields C_{lm} and D_{lm} are determined by the electrostatic boundary conditions at the surface of the microsphere. The first-order fields exhibit a dipolar character outside the microparticle, therefore, the electrostatic fields consist of $l = 1$, $m = \pm 1$ at ω_1 , and $l = 1$, $m = \pm 1$ at ω_2 . Thus, the second-order fields should have monopole and quadrupole characters. The second-order electrostatic field should consist of $l = 0$ and the $l = 2$, $m = (0, \pm 1, \pm 2)$ terms. However, a monopole field vanishes by charge conservation. Hence, only the coefficients for the quadrupole contribute, i.e., D_{20} (C_{20}), $D_{2\pm 1}$ ($C_{2\pm 1}$) and $D_{2\pm 2}$ ($C_{2\pm 2}$) are non-zero. Finally, the second-order drift velocity, $v_2(r, \omega_{\pm})$ can be expressed in terms of $n_2(r, \omega_{\pm})$ and $\phi_2(r, \omega_{\pm})$ via Euler's Equation and given by

$$v_2(r, \omega_{\pm}) = v_2''(r, \omega_{\pm}) + v_2'(r, \omega_{\pm}) \quad (B.6)$$

where

$$v_2''(r, \omega_{\pm}) = -1 [S_{\pm}(r) - (n_0 e / m) \nabla \phi(r, \omega_{\pm}) + \beta^2 \nabla n_2(r, \omega_{\pm})] / n_0 (\omega_{\pm} + i\nu) \quad (B.6a)$$

and

$$v_2'(r, \omega_{\pm}) = -\frac{1}{n_0} n_1(r, \omega_1) v_1(r, \pm \omega_2) - \frac{1}{n_0} n_1(r, \pm \omega_2) v_1(r, \omega_1) \quad (\text{B.6b})$$

Equations B.1 through B.3, along with the boundary conditions on the drift velocity and the electrostatic potential, completely determine the unknown coefficients B_{lm} , C_{lm} and D_{lm} . It is a tedious but a straightforward task to obtain the following expression for the density $n_2(r, \omega_{\pm})$:

$$\begin{aligned} n_2(r, \omega_{\pm}) = & r_{\pm} \{ (4\pi/9)^{1/2} n_{2,00}(r, \omega_{\pm}) \eta \sin \theta_2 Y_{00}(\theta) \\ & + (16\pi/45)^{1/2} n_{2,20}(r, \omega_{\pm}) \eta \sin \theta_2 Y_{20}(\theta) \\ & - (2\pi/15)^{1/2} n_{2,21-}(r, \omega_{\pm}) \eta \cos \theta_2 [Y_{21}(\theta, \phi) - Y_{2-1}(\theta, \phi)] \\ & + i (2\pi/15)^{1/2} n_{2,21+}(r, \omega_{\pm}) \sin \theta_2 [Y_{21}(\theta, \phi) + Y_{2-1}(\theta, \phi)] \\ & - i (2\pi/15)^{1/2} n_{2,22}(r, \omega_{\pm}) \cos \theta_2 [Y_{22}(\theta, \phi) - Y_{2-2}(\theta, \phi)] \} \end{aligned} \quad (\text{B.7a})$$

where

$$r_{\pm} \equiv \epsilon_b A_1 A_2 q_{\pm} a / 4\pi m \beta^2 D(\omega_1) D(\omega_2) \quad (\text{B.7b})$$

where $q_{\pm} = [\omega_p^2 - \omega_{\pm}(\omega_{\pm} + i\nu)]^{1/2}/\beta$. The quantity r_{\pm} , which has units of density, exhibits resonant behavior if ω_1 and/or ω_2 lie near the surface dipole mode frequency ω_s . This feature of the second-order density response follows directly from the drive term, $S_{\pm}(r)$. An examination of Equation B.7a reveals the important role of the initial geometry as manifested in the angle θ_2 and the initial polarization as manifested in η .

The dimensionless functions in monopole and quadrupole radial density $n_{2,00}(r, \omega_{\pm})$ and $n_{2,2m}(r, \omega_{\pm})$ are given by

$$n_{2,00}(r, \omega_{\pm}) = i_0(q_{\pm}r)J_{00S}(a, \omega_{\pm})/i_1(q_{\pm}a) - J_{00}(r, \omega_{\pm}) \quad (B.7c)$$

$$n_{2,2m}(r, \omega_{\pm}) = \bar{J}_{2m}(a, \omega_{\pm})i_2(q_{\pm}r)/i_2'(q_{\pm}a)D_2(\omega_{\pm}) - J_{2m}(r, \omega_{\pm}) \quad (B.7d)$$

where the denominator $D_2(\omega_{\pm})$, which appears only in the quadrupole radial density terms in Equation B.7d, is given by

$$D_2(\omega_{\pm}) = 2\epsilon_b(\alpha_{\pm} - 1) + 3\epsilon_h(\omega_{\pm}) [\alpha_{\pm} - 2i_2(q_{\pm}a)/q_{\pm}ai_2'(q_{\pm}a)] \quad (B.8)$$

where $\alpha_{\pm} = \omega_{\pm}(\omega_{\pm} + i\nu)/\omega_p^2$. Note that $D_2(\omega_{\pm})$ is a function only of ω_{\pm} , not ω_1 or ω_2 individually. This feature follows because $D_2(\omega_{\pm})$ reflects the possibility of exciting a surface mode if ω_{\pm} coincides with a quadrupole Frohlich surface resonant frequency ω_q .

In Equations B.7, the functions $J_{\ell m}(r, \omega_{\pm})$ are defined as

$$J_{\ell m}(r, \omega_{\pm}) = k_{\ell}(q_{\pm}r)j_{\ell m}^{<}(r, \omega_{\pm}) + i_{\ell}(q_{\pm}r)j_{\ell m}^{>}(r, \omega_{\pm}) \quad (B.9a)$$

where $(\ell, m) = (0, 0), (2, 0)$ and $(2, 1)$, two functions J_{00S} and \bar{J}_{2m} are defined by

$$J_{00S}(r, \omega_{\pm}) = \frac{q_{\pm}}{a^2} \int_0^r dr' r'^2 J_{00}(r', \omega_{\pm}) \quad (B.9b)$$

$$\begin{aligned} \bar{J}_{2m}(r, \omega_{\pm}) &= (3\epsilon_h(\omega_{\pm}) + 2\epsilon_b) (\alpha_{\pm} - 1) J_{2m}'(a, \omega_{\pm}) \\ &+ 3\epsilon_h(\omega_{\pm}) J_{2mS}(a, \omega_{\pm}) \end{aligned} \quad (B.9c)$$

with

$$J_{\ell m}'(r, \omega_{\pm}) = K_{\ell}'(q_{\pm} r) j_{\ell m}^{<}(r, \omega_{\pm}) + i_{\ell}'(q_{\pm} r) j_{\ell m}^{>}(r, \omega_{\pm}) \quad (B.9d)$$

$$J_{2mS}(r, \omega_{\pm}) = \frac{q_{\pm}}{a^4} \int_0^r dr' r'^4 J_{2m}(r', \omega_{\pm}) \quad (B.9e)$$

The functions $j_{\ell m}^{<}(r, \omega_{\pm})$ and $j_{\ell m}^{>}(r, \omega_{\pm})$ are given by

$$j_{00}^{<}(r, \omega_{\pm}) = (q_{\pm}/a^2) \int_0^r dr' r'^2 i_0'(q_{\pm} r') S_{r00}(r') \quad (B.10a)$$

$$j_{00}^{>}(r, \omega_{\pm}) = (q_{\pm}/a^2) \int_r^a dr' r'^2 k_0'(q_{\pm} r') S_{r00}^{\pm}(r') \quad (B.10b)$$

$$\begin{aligned}
j_{2m}^{<}(r, \omega_{\pm}) &= (q_{\pm}/a^2) \int_0^r dr' r'^2 i_2(q_{\pm} r') S_{r,20}^{\pm}(r') \\
&+ (1/a^2) \int_0^r dr' r'^2 i_2(q_{\pm} r') S_{\theta,2m}^{\pm}(r')
\end{aligned} \tag{B.10c}$$

and

$$\begin{aligned}
j_{2m}^{>}(r, \omega_{\pm}) &= (q_{\pm}/a^2) \int_r^a dr' r'^2 k_2(q_{\pm} r') S_{r,20}^{\pm}(r') \\
&+ (1/a^2) \int_r^a dr' r'^2 k_2(q_{\pm} r') S_{\theta,2m}^{\pm}(r')
\end{aligned} \tag{B.10d}$$

where the $S_{lm}^{\pm}(r)$ are given in Equations B.1.

The next focus is on the electric component of the second-order electric fields oscillating at the sum and difference-frequencies in the vicinity of the microparticle. Inside the particle, the various components of the electric field are given by

$$\begin{aligned}
E_{2r}(r, \omega_{\pm}) &= E_{20} \{ (4\pi/9)^{1/2} \sin\theta_2 Y_{00}(\theta) \varepsilon_{r,00}^{\pm}(r) \\
&+ (16\pi/45)^{1/2} \sin\theta_2 Y_{20}(\theta) \varepsilon_{r,20}^{\pm}(r) \\
&- (2\pi/15)^{1/2} \cos\theta_2 [\gamma_{21}(\theta, \phi) - \gamma_{2-1}(\theta, \phi)] \varepsilon_{r,21-}^{\pm}(r)
\end{aligned}$$

$$\begin{aligned}
& + i(2\pi/15)^{1/2} \sin\theta_2 [Y_{21}(\theta, \phi) + Y_{2-1}(\theta, \phi)] \Sigma_{r,21-}^{\pm}(r) \\
& - i(2\pi/15)^{1/2} \cos\theta_2 [Y_{22}(\theta, \phi) - Y_{2-2}(\theta, \phi)] \Sigma_{r,22}^{\pm}(r) \}
\end{aligned}
\tag{B.11a}$$

$$\begin{aligned}
E_{2\theta}(r, \omega_{\pm}) = E_{20} \{ & (16\pi/45)^{1/2} \sin\theta_2 \eta \frac{\partial}{\partial\theta} Y_{20}(\theta) \Sigma_{\theta,20}^{\pm}(r) \\
& - (2\pi/15)^{1/2} \cos\theta_2 \eta \frac{\partial}{\partial\theta} [Y_{21}(\theta, \phi) - Y_{2-1}(\theta, \phi)] \Sigma_{\theta,21-}^{\pm}(r) \\
& + i(2\pi/15)^{1/2} \sin\theta_2 \frac{\partial}{\partial\theta} [Y_{21}(\theta, \phi) + Y_{2-1}(\theta, \phi)] \Sigma_{\theta,21+}^{\pm}(r) \\
& - i(2\pi/15)^{1/2} \cos\theta_2 \frac{\partial}{\partial\theta} [Y_{22}(\theta, \phi) - Y_{2-2}(\theta, \phi)] \Sigma_{\theta,22}^{\pm}(r) \}
\end{aligned}
\tag{B.11b}$$

$$\begin{aligned}
E_{2\phi}(r, \omega_{\pm}) = E_{20} \{ & -(2\pi/15)^{1/2} \cos\theta_2 \eta \frac{1}{\sin\theta} \frac{\partial}{\partial\phi} [Y_{21}(\theta, \phi) - Y_{2-1}(\theta, \phi)] \Sigma_{\theta,21-}^{\pm}(r) \\
& + i(2\pi/15)^{1/2} \sin\theta_2 \frac{1}{\sin\theta} \frac{\partial}{\partial\phi} [Y_{21}(\theta, \phi) + Y_{2-1}(\theta, \phi)] \Sigma_{\theta,21+}^{\pm}(r) \\
& - i(2\pi/15)^{1/2} \cos\theta_2 \frac{1}{\sin\theta} \frac{\partial}{\partial\phi} [Y_{22}(\theta, \phi) - Y_{2-2}(\theta, \phi)] \Sigma_{\theta,22}^{\pm}(r) \}
\end{aligned}
\tag{B.11c}$$

where

$$E_{20} = 4\pi e r_{\pm} / \epsilon_b q_{\pm} \quad (\text{B.12})$$

Thus, the second-order electric fields have r, θ and ϕ -components. This complex polarization structure arises from the fact that the incident fields for the noncollinear configuration break the cylindrical symmetry of the system, a point which is underscored by the fact that the ϕ -component of the electric field vanishes, viz, the cylindrical symmetry is restored, if the two laser beams are collinear (i.e., $\theta_2 = \pi/2$) and copolarized. The functions $\varepsilon_{a,lm}^{\pm}(r)$ are dimensionless field strengths which are defined by:

$$\varepsilon_{r,00}^{\pm}(r) = (a/r)^2 J_{00S}(r, \omega_{\pm}) - J_{00S}(a, \omega_{\pm}) i_1(q_{\pm} r) / i_1(q_{\pm} a) \quad (\text{B.13a})$$

$$\varepsilon_{r,2m}^{\pm}(r) = 2Q_{\pm} \varepsilon_{2m}(a, \omega_{\pm}) r/a + \varepsilon_{2m}(r, \omega_{\pm}) - (2/3) \varepsilon_{2mG}(r, \omega_{\pm}) \quad (\text{B.13b})$$

$$\varepsilon_{\theta,2m}^{\pm}(r) = Q_{\pm} \varepsilon_{2m}(a, \omega_{\pm}) r/a - [\varepsilon_{2m}(r, \omega_{\pm}) + \varepsilon_{2mG}(r, \omega_{\pm})] / 3 \quad (\text{B.13c})$$

where

$$Q_{\pm} = (\epsilon_h(\omega_{\pm}) - \epsilon_b) / (3\epsilon_h(\omega_{\pm}) + 2\epsilon_b)$$

The functions $\varepsilon_{2m}(r, \omega_{\pm})$ and $\varepsilon_{2mG}(r, \omega_{\pm})$ are defined as

$$\varepsilon_{2m}(r, \omega_{\pm}) = 3/5 [(a/r)^4 J_{2mS}(r, \omega_{\pm}) - J_{2m}(a, \omega_{\pm}) i_3(q_{\pm} r) / i_2^1(q_{\pm} a) D_2(\omega_{\pm})] \quad (\text{B.14a})$$

$$\begin{aligned} \varepsilon_{2mG}(r, \omega_{\pm}) = & 3/5 [q_{\pm} r J_{2mG}(r, \omega_{\pm}) \\ & - \bar{J}_{2m}(a, \omega_{\pm}) \{i_1(q_{\pm} r) - i_1(q_{\pm} a) r/a\} / i_2'(q_{\pm} a) D_2(\omega_{\pm})] \end{aligned} \quad (B.14b)$$

with J_{00S} , \bar{J}_{2mS} and J_{2mS} are given in Equations B.7b, B.7c and B.7e and

$$J_{2mG}(r, \omega_{\pm}) = \int_r^a dr' J_{2m}(r', \omega_{\pm}) / r' \quad (B.15)$$

The electric field inside the microparticle has two possible frequencies where a surface mode resonance can be excited. Specifically, the presence of the r_{\pm} factor implies possible resonant enhancement of the field if ω_1 and/or ω_2 coincide with the surface dipolar mode. Further, the $D_2(\omega_{\pm})$ resonant denominator in Equations B.14 implies that the quadrupole surface mode at ω_{\pm} can also amplify the field. In actual practice, all three frequencies (ω_1 , ω_2 and ω_{\pm}) cannot coincide with a Frohlich resonance for the second-order processes discussed here.

Outside the microparticle, the electric fields are quadrupolar in nature. In the near (static) zone, the electrostatic potential of a sphere is given by

$$\begin{aligned} \phi_2(r, \omega_{\pm}) = & 1/3 \{ (16\pi/45)^{1/2} \gamma_{20}(\theta) Q_{zz} \\ & - (2\pi/15)^{1/2} [\gamma_{21}(\theta, \phi) - \gamma_{2-1}(\theta, \phi)] Q_{xz} \} / r^3 \end{aligned} \quad (B.16)$$

The components of the quadrupole moment, $Q_{\mu\nu}$, in terms of the dimensionless quantities U_{2j} are given by

$$Q_{zz} = -16\pi\epsilon r_{\pm} \sin\theta_2 U_{20}^{\pm} a^5 / 3(3\epsilon_h(\omega_{\pm}) + 2\epsilon_b) \quad (\text{B.17a})$$

$$Q_{xz} = -4\pi\epsilon r_{\pm} \cos\theta_2 U_{21}^{\pm} a^5 / (3\epsilon_h(\omega_{\pm}) + 2\epsilon_b) \quad (\text{B.17b})$$

where U_{2m}^{\pm} is the dimensionless function in the quadrupole moments and given by

$$U_{2m}^{\pm} = \frac{1}{a^5} \int_0^a r^4 dr n_{2,2m}(r, \omega_{\pm}) \quad (\text{B.18a})$$

$$= [\bar{J}_{2m}(a, \omega_{\pm}) i_3(q_{\pm} a) / D_2(\omega_{\pm}) - J_{2mS}(a, \omega_{\pm})] / q_{\pm} a \quad (\text{B.18b})$$

As expected, the quadrupole moments and the electrostatic field outside the microparticle are also surface enhanced if either of the frequencies ω_1 or ω_2 coincides with the surface dipole resonance (from r_{\pm}) or ω_{\pm} with the surface quadrupole resonance from $D_2(\omega_{\pm})$.

The second-order electron drift velocity $v_2^{\pm}(r, \omega_{\pm})$ in Equation B.6a is given by

$$\begin{aligned} v_{2r}^{\pm}(r, \omega_{\pm}) = & v_{20} [(4\pi/9)^{1/2} \sin\theta_2 n Y_{00}(\theta) \tilde{z}_{r,00}^{\pm}(r) \\ & + (16\pi/45)^{1/2} \sin\theta_2 n Y_{20}(\theta) \tilde{z}_{r,20}^{\pm}(r) \\ & - (2\pi/15)^{1/2} \cos\theta_2 n (Y_{21}(\theta, \phi) - Y_{2-1}(\theta, \phi)) \tilde{z}_{\theta,21-}^{\pm}(r) \\ & + i (2\pi/15)^{1/2} \sin\theta_2 (Y_{21}(\theta, \phi) + Y_{2-1}(\theta, \phi)) \tilde{z}_{\theta,21+}^{\pm}(r) \\ & - i (2\pi/15)^{1/2} \cos\theta_2 (Y_{22}(\theta, \phi) - Y_{2-2}(\theta, \phi)) \tilde{z}_{\theta,22}^{\pm}(r)] \end{aligned} \quad (\text{B.19a})$$

$$\begin{aligned}
v_{20}''(r, \omega_{\pm}) = & v_{20} [(16\pi/45)^{1/2} \sin\theta_2 \frac{\partial}{\partial\theta} Y_{20}(\theta) \tilde{x}_{\theta,20}^{\pm}(r) \\
& - (2\pi/15)^{1/2} \cos\theta_2 \frac{\partial}{\partial\theta} (Y_{21}(\theta, \phi) - Y_{2-1}(\theta, \phi)) \tilde{x}_{\theta,21-}^{\pm}(r) \\
& + i (2\pi/15)^{1/2} \sin\theta_2 \frac{\partial}{\partial\theta} (Y_{21}(\theta, \phi) + Y_{2-1}(\theta, \phi)) \\
& - i (2\pi/15)^{1/2} \cos\theta_2 \frac{\partial}{\partial\theta} (Y_{22}(\theta, \phi) - Y_{2-2}(\theta, \phi)) \tilde{x}_{\theta,22}^{\pm}(r)]
\end{aligned}
\tag{B.19b}$$

$$\begin{aligned}
v_{2\phi}''(r, \omega_{\pm}) = & v_{20} [- (2\pi/15)^{1/2} \cos\theta_2 \frac{1}{\sin\theta} \frac{\partial}{\partial\phi} (Y_{21}(\theta, \phi) - Y_{2-1}(\theta, \phi)) \tilde{x}_{\phi,21-}^{\pm}(r) \\
& + i (2\pi/15)^{1/2} \sin\theta_2 \frac{1}{\sin\theta} \frac{\partial}{\partial\phi} (Y_{21}(\theta, \phi) + Y_{2-1}(\theta, \phi)) \tilde{x}_{\phi,21+}^{\pm}(r) \\
& - (2\pi/15)^{1/2} \cos\theta_2 \frac{1}{\sin\theta} \frac{\partial}{\partial\phi} (Y_{22}(\theta, \phi) - Y_{2-2}(\theta, \phi)) \tilde{x}_{\phi,22}^{\pm}(r)]
\end{aligned}
\tag{B.19c}$$

where

$$v_{20} = - i \beta^2 q_{\pm} r_{\pm} / n_0 (\omega_{\pm} + i\nu) \tag{B.20}$$

And the dimensionless function $\tilde{x}_{a,lm}^{\pm}(r)$ is given by

$$\tilde{x}_{r,00}^{\pm}(r) = J_{00S}(a, \omega_{\pm}) i_1(q_{\pm} r) / i_1(q_{\pm} a) - J_{00}'(r, \omega_{\pm}) + \varepsilon_{r,00}(r) q_{TF}^2 / q_{\pm}^2 \tag{B.21a}$$

$$\begin{aligned}
\tilde{x}_{r,2m}^{\pm}(r) = & J_{2m}(a, \omega_{\pm}) i_2'(q_{\pm} r) / i_2'(q_{\pm} a) D_2(\omega_{\pm}) - J_{2m}'(r, \omega_{\pm}) \\
& + \varepsilon_{r,2m}^{\pm}(r) q_{TF}^2 / q_{\pm}^2
\end{aligned}
\tag{B.21b}$$

$$\tilde{\varepsilon}_{\theta,2m}^{\pm}(r) = \sigma_{2m}^{\pm}(r) + \frac{1}{q_{\pm}^2 a^2} S_{\theta,2m}^{\pm}(r) \quad (\text{B.21c})$$

$$\tilde{\varepsilon}_{\phi,21}^{\pm}(r) = \sigma_{21}^{\pm}(r) + \frac{1}{q_{\pm}^2 a^2} S_{\phi,21}^{\pm}(r) \quad (\text{B.21d})$$

where J_{00S} , J_{00}^{\dagger} , \bar{J}_{2m} , D_2 , $S_{\theta,2m}^{\pm}$ and $S_{\phi,21}^{\pm}$ are defined previously in Equations B.7, B.8 and B.9, $\varepsilon_{a,2m}^{\pm}$ is the dimensionless field strengths given in Equations B.13, $q_{TF} = \omega_p/\beta$, and

$$\sigma_{2m}^{\pm}(r) = n_{2,2m}(r, \omega_{\pm})/q_{\pm} r + \varepsilon_{\theta,2m}^{\pm}(r) q_{TF}^2/q_{\pm}^2 \quad (\text{B.22})$$

APPENDIX C

To solve Equations 2.12 for a sphere, expand $n_3(r, \omega_j)$ in terms of spherical harmonics as $n_1(r, \omega_j)$ and $n_2(r, \omega_{\pm})$.

$$n_3(r, \omega_j) = \sum G_{lm}(q_j a) i_l(q_j r) Y_{lm}(\theta, \phi) + \int dr' [G_S(q_j r, r') \nabla \cdot T(r'; \omega_j)] / \beta^2 \quad (C.1a)$$

where the integral is an inhomogeneous term and the coefficients G_{lm} are determined by the boundary conditions. The Green's function $G_S(q_j | r, r')$ is given by

$$G_S(q_j | r, r') = q_j \sum i_l(q_j r_<) K_l(q_j r_>) Y_{lm}^*(\theta', \phi') Y_{lm}(\theta, \phi) \quad (C.1b)$$

where * implies a complex conjugate. The third-order fields at ω_j obey the Laplace equation

$$\nabla^2 \phi_3(r, \omega_j) = 0 \quad (C.2a)$$

outside the microparticle, and Poisson equation

$$\nabla^2 \phi_3(r, \omega_j) = 4\pi e n_3(r, \omega_j) / \epsilon_b \quad (C.2b)$$

within it. Equations C.2 will be solved by expanding in spherical harmonics. Thus, outside the sphere, we have

$$\phi_3(r, \omega_j) = \sum E_{lm}(q_j a) r^{-(l+1)} Y_{lm}(\theta, \phi) \quad (C.3a)$$

The electrostatic potential inside the microparticle is driven by the third-order charge density, $n_3(r, \omega_j)$. Thus, within this region, the third-order electrostatic potential is written as

$$\phi_3(r, \omega_j) = \sum F_{lm}(q_j a) r^l Y_{lm}(\theta, \phi) - (4\pi e / \epsilon_b) \int dr' G_0(r, r') n_3(r', \omega_j) \quad (C.3b)$$

where $G_0(r, r')$ is the Green's function for the Laplace equation. The coefficients for the various multipole fields E_{lm} and F_{lm} are determined by the electrostatic boundary conditions at the surface of the microsphere. The first-order fields exhibit a dipolar character outside the microparticle, viz, the electrostatic fields consist of $l = 1, m = \pm 1$ at ω_1 , and $l = 1, m = \pm 1$ at ω_2 . The second-order fields have monopole and quadrupole characters. The second-order electrostatic fields consist of $l = 0$ and the $l = 2, m = (0, \pm 1, \pm 2)$ terms. However, a monopole field vanishes by charge conservation. Hence, only the quadrupole contributions are nonzero. Then, the third-order field should have dipole and octupole characters, since the third-order electrostatic fields consist of $l = 1, m = 0, \pm 1$ and $l = 3, m = 0, m = \pm 1, m = \pm 2, m = \pm 3$ terms. Finally, the third-order drift velocity, $v_3(r, \omega_j)$ can be expressed in terms of $n_3(r, \omega_j)$ and $\phi_3(r, \omega_j)$ via Euler's Equation and given by

$$v_3(r, \omega_j) = v_3''(r, \omega_j) + v_3'(r, \omega_j) \quad (C.4)$$

where

$$v_3''(r, \omega_j) = -i[T(r; \omega_j) - (n_0 e/m) v \phi(r, \omega_j) + \beta^2 v n_3(r, \omega_j)]/n_0(\omega_j + i\nu) \quad (C.5a)$$

and

$$\begin{aligned} v_3'(r, \omega_1) = & -\frac{1}{n_0} n_1(r, \omega_2) v_2(r, \omega_-) - \frac{1}{n_0} n_2(r, \omega_-) v_1(r, \omega_2) \\ & - \frac{1}{n_0} n_1(r, -\omega_2) v_2(r, \omega_+) - \frac{1}{n_0} n_2(r, \omega_+) v_1(r, -\omega_2) \end{aligned} \quad (C.5b)$$

Equations C.1 through C.3, along with the boundary conditions on the drift velocity and the electrostatic potential, completely determine the unknown coefficients E_{lm} , F_{lm} , and G_{lm} . It is a tedious, but a straightforward task to obtain the following expression for the density $n_3(r, \omega_j)$:

$$\begin{aligned} n_3(r, \omega_j) = & \sum_{i=1}^2 r_{3j} \{ (4\pi/3)^{1/2} n_{3i,10}(r, \omega_j) Y_{10}(\theta) \\ & + i (2\pi/3)^{1/2} n_{3i,11}(r, \omega_j) [Y_{11}(\theta, \phi) + Y_{1-1}(\theta, \phi)] \} \left| \frac{A_1}{D_1(\omega_1)} \right|^2 \\ & + \sum_m n_{3,3m}(r, \omega_j) Y_{3m}(\theta, \phi) \end{aligned} \quad (C.6a)$$

where

$$r_{3j} \equiv \epsilon_b A_j q_j a^2 / 4\pi m^2 \beta^4 D_1(\omega_j) \quad (C.6b)$$

where $q_j = [\omega_p^2 - \omega_j(\omega_j + i\nu)]^{1/2}/\beta$. The third-order density exhibits resonant behavior if ω_1 and/or ω_2 lie near the surface dipole mode frequency ω_s . This feature of the third-order density response follows directly from the drive term, $T(r; \omega_j)$. In Equation C.6a, only the dipole terms which contribute to the third-order susceptibility are written out more explicitly.

The dimensionless functions in dipole radial density $n_{3i,10}(r, \omega_j)$ and $n_{3i,11}(r, \omega_j)$ are given by

$$n_{3i,1m}(r, \omega_j) = \bar{L}_{1m}(a, \omega_j) i_1(q_j r) / \Omega_j i_1'(q_j a) D_1(\omega_j) - L_{1m}(r, \omega_j) \quad (C.6c)$$

where the denominator $D_1(\omega_j)$, which appears in the dipole radial density terms in Equation C.6c, is given by Equation A.2d.

In Equations C.6, the functions $L_{lm}(r, \omega_j)$ are defined as

$$L_{lm}(r, \omega_j) = k_l(q_j r) L_{lm}^<(r, \omega_j) + i_l(q_j r) L_{lm}^>(r, \omega_j) \quad (C.7a)$$

where $(l, m) = (1, 0)$ and $(1, 1)$, function \bar{L}_{1m} is defined by

$$\begin{aligned} \bar{L}_{1m}(r, \omega_j) = & (2\epsilon_h(\omega_j) + \epsilon_b) (\Omega_j - 1) L_{1m}^i(a, \omega_j) \\ & + 2\epsilon_h(\omega_j) L_{1m}^s(a, \omega_j) \end{aligned} \quad (C.7b)$$

with

$$L'_{2m}(r, \omega_j) = K'_{2m}(q_j r) \mathfrak{L}_{2m}^{<}(r, \omega_j) + i_{2m}'(q_j r) \mathfrak{L}_{2m}^{>}(r, \omega_j) \quad (C.7c)$$

$$L_{1mS}(r, \omega_j) = \frac{q_j}{a^3} \int_0^r r' dr' r'^3 L_{1m}(r', \omega_j) \quad (C.7d)$$

The functions $\mathfrak{L}_{2m}^{<}(r, \omega_j)$ and $\mathfrak{L}_{2m}^{>}(r, \omega_j)$ are given by

$$\begin{aligned} \mathfrak{L}_{1m}^{<}(r, \omega_j) = & (q_j/a^2) \int_0^r r' dr' r'^2 i_1'(q_j r') T_{r_{1m}}(r'; \omega_j) \\ & + (1/a^2) \int_0^r r' dr' r' i_1(q_j r') [T_{\theta_{1m}}(r'; \omega_j) + T_{\phi_{1m}}(r'; \omega_j)] \end{aligned} \quad (C.8a)$$

and

$$\begin{aligned} \mathfrak{L}_{1m}^{>}(r, \omega_j) = & (q_j/a^2) \int_r^a dr' r'^2 k_1'(q_j r') T_{r_{1m}}(r'; \omega_j) \\ & + (1/a^2) \int_r^a dr' r' k_1(q_j r') [T_{\theta_{1m}}(r'; \omega_j) + T_{\phi_{1m}}(r'; \omega_j)] \end{aligned} \quad (C.8b)$$

Outside the microparticle, the electric fields are dipole and octupole in nature. In the near (static) zone, the dipole part of electrostatic potential of a sphere is given by

$$\begin{aligned}
\phi_3(r, \omega_j) = & \{(4\pi/3)^{1/2} Y_{10}(\theta) u_0^{(3)}(\omega_j) \\
& + i (2\pi/3)^{1/2} [Y_{11}(\theta, \phi) - Y_{1-1}(\theta, \phi)] u_1^{(3)}(\omega_j) \\
\end{aligned} \tag{C.9}$$

The components of the third-order dipole moment, $u_m^{(3)}$, in terms of the dimensionless quantities $P_{i,1m}^{(3)}$ are given by

$$u_m^{(3)}(\omega_j) = -4\pi\epsilon r \sum_{i=1}^2 a^3 P_{i,1m}^{(3)}(\omega_j) \left| \frac{A_i}{D_1(\omega_i)} \right|^2 \frac{1}{q_j (2\epsilon_h(\omega_j) + \epsilon_b)} \tag{C.10a}$$

where $P_{i,1m}^{(3)}(\omega_j)$ is the dimensionless function in the third-order dipole moments and given by

$$P_{i,1m}^{(3)}(\omega_j) = \frac{q_j}{a^3} \int_0^a r^3 dr n_{31,1m}(r, \omega_j) \tag{C.10b}$$

$$= [L_{1m}(a, \omega_j) i_2(q_j a) / \Omega_j i_1'(q_j a) D_1(\omega_j) - L_{1m} S(a, \omega_j)] \tag{C.10c}$$

As expected, the third-order dipole moments and the third-order electrostatic field outside the microparticle are also surface enhanced if either of the frequencies ω_1 or ω_2 coincides with the surface dipole resonance.

In Equation C.10c, the first and second terms are contributed by the homogeneous and inhomogeneous solution of the third-order density given in Equation C.6a. The homogeneous part has an additional local field enhancement factor as compared to the inhomogeneous part for the third-order polarization in the frequency domain. This difference between the homogeneous and inhomogeneous parts will appear in the time-dependent third-order polarization to be discussed in Section 3.3.2.

The three factors of the local field enhancement are due to the third-order nonlinear processes in the small spheres and the additional fourth factor appearing in the homogeneous part occurring through the boundary condition of the sphere for the homogeneous part of the third-order density.

Finally, the nonlinear third-order polarization of a single sphere is given by

$$P_m^{(3)}(\omega_j) = \sum_{i=1}^2 x_0^{(3)} P_{i,1m}^{(3)}(\omega_j) \frac{A_j}{D_1(\omega_j)} \left| \frac{A_i}{D_1(\omega_i)} \right|^2 \quad (C.11a)$$

where

$$x_0^{(3)} = - \frac{3\epsilon_b}{4\pi(2\epsilon_h(\omega_j) + \epsilon_b)} \frac{e^2 a^2}{m^2 \beta^4} \quad (C.11b)$$